

AFIT/GSO/ENP/93D-02

**AD-A273 882**



**DTIC**  
**ELECTE**  
**DEC 17 1993**  
**S E D**

**HYPERSPECTRAL ANALYSIS OF SPACE OBJECTS:  
SIGNAL TO NOISE EVALUATION**

**THESIS**  
**Daniel Hrovat**  
**Captain, USAF**

AFIT/GSO/ENP/93D-02

**93-30498**



Approved for public release; distribution unlimited

**'93 12 15118**

**Best  
Available  
Copy**

AFIT/GSO/ENP/93D-02

HYPERSPECTRAL ANALYSIS OF SPACE OBJECTS:  
SIGNAL TO NOISE EVALUATION

THESIS

Presented to the Faculty of the Graduate School of Engineering  
of the Air Force Institute of Technology  
Air University  
In Partial Fulfillment of the  
Requirements for the Degree of  
Master of Science (Space Operations)

Daniel Hrovat, B.S.  
Captain, USAF

December, 1993

Accession For	
NTIS CRA&I	<input checked="" type="checkbox"/>
DTIC TAB	<input checked="" type="checkbox"/>
Unannounced	<input type="checkbox"/>
Justification .....	
By .....	
Distribution /	
Availability Codes	
Dist	Avail and/or Special
A-1	

Approved for public release; distribution unlimited

DTIC QUALITY INSPECTED 1

## *Preface*

My quest for a thesis topic began with an interest in detecting space objects using a space-based sensor. My advisor, Dr. Michael C. Roggemann, worked with me on defining the scope of my research. During a visit to Phillips Lab, Dr. Roggemann discovered the Lasers and Imaging branch (PL/LIMI) was interested in hyperspectral imaging of space objects for Space Object Identification applications. Hyperspectral imaging involves viewing an object in very narrow wavelength bandwidths. The information stored in each wavelength bandwidth forms a spectral signature, which can possibly be used to identify an object. My thesis evolved into hyperspectral analysis of space objects, and addressed the question if enough target signal was present in the narrow wavelength bandwidths to conduct hyperspectral measurements. I owe a great deal of thanks to Dr. Roggemann for his guidance, insight, patience, and sense of humor. I can honestly say I enjoyed my research. I also thank Dr. Theodore E. Luke, my co-advisor, for asking difficult questions that probed my understanding. To my wife Danielle and son Peter, I love you very much, and thanks for *everything*. Finally, I thank God, who makes all things possible.

I dedicate this thesis to General James H. Doolittle, pioneer aviator, 1923 graduate of the Air Service Engineering School (AFIT's predecessor), and leader of the Tokyo raid. General Doolittle advocated effective use of air power for the defense of the United States. I pray I have the same vision for space power as General Doolittle had for air power.

*General James H. Doolittle, 1896-1993*

Daniel Hrovat

## *Table of Contents*

	<b>Page</b>
<b>Preface</b> . . . . .	ii
<b>List of Figures</b> . . . . .	vii
<b>List of Tables</b> . . . . .	x
<b>Abstract</b> . . . . .	xii
<b>I. Introduction</b> . . . . .	1-1
1.1 Background . . . . .	1-1
1.2 Problem Statement . . . . .	1-2
1.3 Approach . . . . .	1-2
1.4 Scope . . . . .	1-3
1.5 Summary of Key Results . . . . .	1-3
1.6 Organization . . . . .	1-4
<b>II. Theory</b> . . . . .	2-1
2.1 Introduction . . . . .	2-1
2.2 Target Signal . . . . .	2-1
2.2.1 Introduction . . . . .	2-1
2.2.2 Radiometry . . . . .	2-1
2.2.3 Target Count Rate Equation . . . . .	2-7
2.3 Background Noise . . . . .	2-8
2.4 Detector Noise . . . . .	2-9
2.5 Integration Time . . . . .	2-9
2.6 Signal to Noise Ratio . . . . .	2-10

	Page
2.6.1 SNR Equation for Imaging . . . . .	2-10
2.6.2 SNR Equation for Spectrometry . . . . .	2-14
<b>III. Results . . . . .</b>	<b>3-1</b>
3.1 Introduction . . . . .	3-1
3.2 Procedure . . . . .	3-1
3.2.1 Configuration . . . . .	3-1
3.2.2 Spectral Reflectance Interpolation . . . . .	3-2
3.2.3 Radiometry Model . . . . .	3-3
3.2.4 Example Input and Output . . . . .	3-4
3.2.5 Integration Time . . . . .	3-5
3.3 Hyperspectral Imaging . . . . .	3-9
3.3.1 Case One . . . . .	3-10
3.3.2 Case Two . . . . .	3-14
3.3.3 Comparison, Case One versus Case Two . . . . .	3-16
3.4 Hyperspectrometry . . . . .	3-18
3.4.1 Case Three . . . . .	3-18
3.4.2 Case Four . . . . .	3-22
3.4.3 Comparison, Case Three versus Case Four . . . . .	3-27
<b>IV. Conclusions and Recommendations . . . . .</b>	<b>4-1</b>
4.1 Conclusions . . . . .	4-1
4.2 Recommendations for Further Research . . . . .	4-2
<b>Appendix A. Mathcad Models . . . . .</b>	<b>A-1</b>
A.1 Model Configuration . . . . .	A-1
A.2 Spectral Reflectivity Interpolation . . . . .	A-1
A.3 Radiometry Model . . . . .	A-1

	<b>Page</b>
<b>Appendix B. Case (1): 20 nm, 10 nm and 5 nm Graphs . . . . .</b>	<b>B-1</b>
<b>B.1 Legend . . . . .</b>	<b>B-1</b>
<b>B.2 20 nm graphs . . . . .</b>	<b>B-1</b>
<b>B.3 10 nm graphs . . . . .</b>	<b>B-1</b>
<b>B.4 5 nm graphs . . . . .</b>	<b>B-2</b>
<b>Appendix C. Case (2): 20 nm, 10 nm and 5 nm Graphs . . . . .</b>	<b>C-1</b>
<b>C.1 Legend . . . . .</b>	<b>C-1</b>
<b>C.2 20 nm graphs . . . . .</b>	<b>C-1</b>
<b>C.3 10 nm graphs . . . . .</b>	<b>C-1</b>
<b>C.4 5 nm graphs . . . . .</b>	<b>C-2</b>
<b>Appendix D. Case (3): 20 nm, 10 nm and 5 nm Graphs . . . . .</b>	<b>D-1</b>
<b>D.1 Legend . . . . .</b>	<b>D-1</b>
<b>D.2 20 nm graphs . . . . .</b>	<b>D-2</b>
<b>D.2.1 Ultraviolet (UV), 300 nm - 400 nm . . . . .</b>	<b>D-2</b>
<b>D.2.2 Blue (B), 380 nm - 540 nm . . . . .</b>	<b>D-2</b>
<b>D.2.3 Visible (V), 480 nm - 650 nm . . . . .</b>	<b>D-2</b>
<b>D.3 10 nm graphs . . . . .</b>	<b>D-2</b>
<b>D.3.1 Ultraviolet (UV), 300 nm - 400 nm . . . . .</b>	<b>D-2</b>
<b>D.3.2 Blue (B), 380 nm - 540 nm . . . . .</b>	<b>D-3</b>
<b>D.3.3 Visible (V), 480 nm - 650 nm . . . . .</b>	<b>D-3</b>
<b>D.4 5 nm graphs . . . . .</b>	<b>D-3</b>
<b>D.4.1 Ultraviolet (UV), 300 nm - 400 nm . . . . .</b>	<b>D-3</b>
<b>D.4.2 Blue (B), 380 nm - 540 nm . . . . .</b>	<b>D-3</b>
<b>D.4.3 Visible (V), 480 nm - 650 nm . . . . .</b>	<b>D-4</b>

	Page
Appendix E. Case (4): 20 nm, 10 nm and 5 nm Graphs . . . . .	E-1
E.1 Legend . . . . .	E-1
E.2 20 nm graphs . . . . .	E-2
E.2.1 Ultraviolet (UV), 300 nm - 400 nm . . . . .	E-2
E.2.2 Blue (B), 380 nm - 540 nm . . . . .	E-2
E.2.3 Visible (V), 480 nm - 650 nm . . . . .	E-2
E.3 10 nm graphs . . . . .	E-2
E.3.1 Ultraviolet (UV), 300 nm - 400 nm . . . . .	E-2
E.3.2 Blue (B), 380 nm - 540 nm . . . . .	E-3
E.3.3 Visible (V), 480 nm - 650 nm . . . . .	E-3
E.4 5 nm graphs . . . . .	E-3
E.4.1 Ultraviolet (UV), 300 nm - 400 nm . . . . .	E-3
E.4.2 Blue (B), 380 nm - 540 nm . . . . .	E-3
E.4.3 Visible (V), 480 nm - 650 nm . . . . .	E-4
Appendix F. Spectral Reflectance of Various Materials . . . . .	F-1
Bibliography . . . . .	BIB-1
Vita . . . . .	VITA-1



## List of Figures

Figure	Page
2.1. Target-sensor and source-target angles . . . . .	2-3
3.1. Spectral Reflectance (%), SMC-23: Solar Cell, Silicon . . . . .	3-2
3.2. Case (1), Count Rate $\frac{iT}{q}$ (1/s) vs $\Omega$ ( $rad m^2$ ), 10 nm . . . . .	3-6
3.3. Case (1), SNR vs $\Omega$ ( $rad m^2$ ), 10 nm . . . . .	3-7
3.4. Case (1), $SNR_{pix}$ vs $z$ , 10 nm . . . . .	3-8
3.5. Case (2), SNR vs $\Omega$ ( $rad m^2$ ), 10 nm . . . . .	3-17
3.6. Case (3), SNR vs $\Omega$ ( $rad m^2$ ) (UV), 10 nm . . . . .	3-29
3.7. Case (4), SNR vs $\Omega$ ( $rad m^2$ ) (UV), 10 nm . . . . .	3-30
3.8. Case (3), SNR vs $\Omega$ ( $rad m^2$ ) (B), 10 nm . . . . .	3-32
3.9. Case (4), SNR vs $\Omega$ ( $rad m^2$ ) (B), 10 nm . . . . .	3-33
3.10. Case (3), SNR vs $\Omega$ ( $rad m^2$ ) (V), 10 nm . . . . .	3-35
3.11. Case (4), SNR vs $\Omega$ ( $rad m^2$ ) (V), 10 nm . . . . .	3-36
B.1. Case (1), Count Rate $\frac{iT}{q}$ (1/s) vs $\Omega$ ( $rad m^2$ ), 20 nm . . . . .	B-3
B.2. Case (1), SNR vs $\Omega$ ( $rad m^2$ ), 20 nm . . . . .	B-4
B.3. Case (1), $SNR_{pix}$ vs $z$ , 20 nm . . . . .	B-5
B.4. Case (1), Count Rate $\frac{iT}{q}$ (1/s) vs $\Omega$ ( $rad m^2$ ), 10 nm . . . . .	B-6
B.5. Case (1), SNR vs $\Omega$ ( $rad m^2$ ), 10 nm . . . . .	B-7
B.6. Case (1), $SNR_{pix}$ vs $z$ , 10 nm . . . . .	B-8
B.7. Case (1), Count Rate $\frac{iT}{q}$ (1/s) vs $\Omega$ ( $rad m^2$ ), 5 nm . . . . .	B-9
B.8. Case (1), SNR vs $\Omega$ ( $rad m^2$ ), 5 nm . . . . .	B-10
B.9. Case (1), $SNR_{pix}$ vs $z$ , 5 nm . . . . .	B-11
C.1. Case (2), Count Rate $\frac{iT}{q}$ (1/s) vs $\Omega$ ( $rad m^2$ ), 20 nm . . . . .	C-3

Figure	Page
C.2. Case (2), SNR vs $\Omega$ ( $rad\ m^2$ ), 20 nm . . . . .	C-4
C.3. Case (2), $SNR_{pix}$ vs $z$ , 20 nm . . . . .	C-5
C.4. Case (2), Count Rate $\frac{iT}{q}$ (1/s) vs $\Omega$ ( $rad\ m^2$ ), 10 nm . . . . .	C-6
C.5. Case (2), SNR vs $\Omega$ ( $rad\ m^2$ ), 10 nm . . . . .	C-7
C.6. Case (2), $SNR_{pix}$ vs $z$ , 10 nm . . . . .	C-8
C.7. Case (2), Count Rate $\frac{iT}{q}$ (1/s) vs $\Omega$ ( $rad\ m^2$ ), 5 nm . . . . .	C-9
C.8. Case (2), SNR vs $\Omega$ ( $rad\ m^2$ ), 5 nm . . . . .	C-10
C.9. Case (2), $SNR_{pix}$ vs $z$ , 5 nm . . . . .	C-11
D.1. Case (3), Count Rate $\frac{iT}{q}$ (1/s) vs $\Omega$ ( $rad\ m^2$ ) (UV), 20 nm . . . . .	D-5
D.2. Case (3), SNR vs $\Omega$ ( $rad\ m^2$ ) (UV), 20 nm . . . . .	D-6
D.3. Case (3), Count Rate $\frac{iT}{q}$ (1/s) vs $\Omega$ ( $rad\ m^2$ ) (B), 20 nm . . . . .	D-7
D.4. Case (3), SNR vs $\Omega$ ( $rad\ m^2$ ) (B), 20 nm . . . . .	D-8
D.5. Case (3), Count Rate $\frac{iT}{q}$ (1/s) vs $\Omega$ ( $rad\ m^2$ ) (V), 20 nm . . . . .	D-9
D.6. Case (3), SNR vs $\Omega$ ( $rad\ m^2$ ) (V), 20 nm . . . . .	D-10
D.7. Case (3), Count Rate $\frac{iT}{q}$ (1/s) vs $\Omega$ ( $rad\ m^2$ ) (UV), 10 nm . . . . .	D-11
D.8. Case (3), SNR vs $\Omega$ ( $rad\ m^2$ ) (UV), 10 nm . . . . .	D-12
D.9. Case (3), Count Rate $\frac{iT}{q}$ (1/s) vs $\Omega$ ( $rad\ m^2$ ) (B), 10 nm . . . . .	D-13
D.10. Case (3), SNR vs $\Omega$ ( $rad\ m^2$ ) (B), 10 nm . . . . .	D-14
D.11. Case (3), Count Rate $\frac{iT}{q}$ (1/s) vs $\Omega$ ( $rad\ m^2$ ) (V), 10 nm . . . . .	D-15
D.12. Case (3), SNR vs $\Omega$ ( $rad\ m^2$ ) (V), 10 nm . . . . .	D-16
D.13. Case (3), Count Rate $\frac{iT}{q}$ (1/s) vs $\Omega$ ( $rad\ m^2$ ) (UV), 5 nm . . . . .	D-17
D.14. Case (3), SNR vs $\Omega$ ( $rad\ m^2$ ) (UV), 5 nm . . . . .	D-18
D.15. Case (3), Count Rate $\frac{iT}{q}$ (1/s) vs $\Omega$ ( $rad\ m^2$ ) (B), 5 nm . . . . .	D-19
D.16. Case (3), SNR vs $\Omega$ ( $rad\ m^2$ ) (B), 5 nm . . . . .	D-20
D.17. Case (3), Count Rate $\frac{iT}{q}$ (1/s) vs $\Omega$ ( $rad\ m^2$ ) (V), 5 nm . . . . .	D-21
D.18. Case (3), SNR vs $\Omega$ ( $rad\ m^2$ ) (V), 5 nm . . . . .	D-22

Figure	Page
E.1. Case (4), Count Rate $\frac{i\tau}{q}$ (1/s) vs $\Omega$ ( $rad\ m^2$ ) (UV), 20 nm . . .	E-5
E.2. Case (4), SNR vs $\Omega$ ( $rad\ m^2$ ) (UV), 20 nm . . . . .	E-6
E.3. Case (4), Count Rate $\frac{i\tau}{q}$ (1/s) vs $\Omega$ ( $rad\ m^2$ ) (B), 20 nm . . . . .	E-7
E.4. Case (4), SNR vs $\Omega$ ( $rad\ m^2$ ) (B), 20 nm . . . . .	E-8
E.5. Case (4), Count Rate $\frac{i\tau}{q}$ (1/s) vs $\Omega$ ( $rad\ m^2$ ) (V), 20 nm . . . . .	E-9
E.6. Case (4), SNR vs $\Omega$ ( $rad\ m^2$ ) (V), 20 nm . . . . .	E-10
E.7. Case (4), Count Rate $\frac{i\tau}{q}$ (1/s) vs $\Omega$ ( $rad\ m^2$ ) (UV), 10 nm . . . . .	E-11
E.8. Case (4), SNR vs $\Omega$ ( $rad\ m^2$ ) (UV), 10 nm . . . . .	E-12
E.9. Case (4), Count Rate $\frac{i\tau}{q}$ (1/s) vs $\Omega$ ( $rad\ m^2$ ) (B), 10 nm . . . . .	E-13
E.10. Case (4), SNR vs $\Omega$ ( $rad\ m^2$ ) (B), 10 nm . . . . .	E-14
E.11. Case (4), Count Rate $\frac{i\tau}{q}$ (1/s) vs $\Omega$ ( $rad\ m^2$ ) (V), 10 nm . . . . .	E-15
E.12. Case (4), SNR vs $\Omega$ ( $rad\ m^2$ ) (V), 10 nm . . . . .	E-16
E.13. Case (4), Count Rate $\frac{i\tau}{q}$ (1/s) vs $\Omega$ ( $rad\ m^2$ ) (UV), 5 nm . . . . .	E-17
E.14. Case (4), SNR vs $\Omega$ ( $rad\ m^2$ ) (UV), 5 nm . . . . .	E-18
E.15. Case (4), Count Rate $\frac{i\tau}{q}$ (1/s) vs $\Omega$ ( $rad\ m^2$ ) (B), 5 nm . . . . .	E-19
E.16. Case (4), SNR vs $\Omega$ ( $rad\ m^2$ ) (B), 5 nm . . . . .	E-20
E.17. Case (4), Count Rate $\frac{i\tau}{q}$ (1/s) vs $\Omega$ ( $rad\ m^2$ ) (V), 5 nm . . . . .	E-21
E.18. Case (4), SNR vs $\Omega$ ( $rad\ m^2$ ) (V), 5 nm . . . . .	E-22
F.1. Spectral Reflectance (%), SMC-02: Aluminum Alloy Type 2024-T3 (Mill Finish) . . . . .	F-2
F.2. Spectral Reflectance (%), SMC-18: Silver . . . . .	F-2
F.3. Spectral Reflectance (%), SMC-20: Paint, Chemglaze A276 (White) . . . . .	F-3
F.4. Spectral Reflectance (%), SMC-23: Solar Cell, Silicon . . . . .	F-3
F.5. Spectral Reflectance (%), SMC-30: Mylar, Aluminized (Aluminum Side Out) . . . . .	F-4

## *List of Tables*

Table	Page
2.1. Target, Sensor, and Source Parameters . . . . .	2-4
3.1. Legend, Case (1), 10 nm . . . . .	3-5
3.2. Summary of Results, Case (1) . . . . .	3-11
3.3. Line Order, Case (1) . . . . .	3-12
3.4. Minimum integration time, Case (1) . . . . .	3-12
3.5. Summary of Results, Case (2) . . . . .	3-15
3.6. Line Order, Case (2) . . . . .	3-16
3.7. Minimum integration time, Case (2) . . . . .	3-16
3.8. Line Order, Case (1) and Case (2) Combined . . . . .	3-16
3.9. Summary of Results, Case (3) . . . . .	3-20
3.10. Line Order, Case (3), UV . . . . .	3-21
3.11. Line Order, Case (3), B . . . . .	3-21
3.12. Line Order, Case (3), V . . . . .	3-22
3.13. Minimum integration time, Case (3) . . . . .	3-23
3.14. Summary of Results, Case (4) . . . . .	3-24
3.15. Line Order, Case (4), UV . . . . .	3-25
3.16. Line Order, Case (4), B . . . . .	3-26
3.17. Line Order, Case (4), V . . . . .	3-26
3.18. Minimum integration time, Case (4) . . . . .	3-27
3.19. Legend, Case (3) and Case (4), 10 nm SNR graphs . . . . .	3-27
3.20. Line Order, Case (3) and Case (4) Combined, UV . . . . .	3-28
3.21. Line Order, Case (3) and Case (4) Combined, B . . . . .	3-31
3.22. Line Order, Case (3) and Case (4) Combined, V . . . . .	3-34

Table	Page
B.1. Legend, Case (1) . . . . .	B-1
C.1. Legend, Case (2) . . . . .	C-1
D.1. Legend, Case (3) . . . . .	D-1
E.1. Legend, Case (4) . . . . .	E-1

*Abstract*

Hyperspectral analysis of space objects is being considered as a means of enhancing Space Object Identification (SOI) capabilities. This study develops a mathematical simulation based on fundamental radiometry principles to evaluate the feasibility of hyperspectral analysis of space objects. The study uses Signal to Noise Ratio (SNR) as the basis for the feasibility evaluation, and addresses the question: Is there enough target signal in narrow wavelength bandwidths to conduct hyperspectral measurements of space objects? The analysis characterizes the target signal and noise sources using fundamental radiometry, and develops a flexible radiometry model which calculates the target signal count rate, and SNR for a specified target-sensor configuration. The model was applied to four case studies, and revealed: 1) Enough target signal is present in narrow wavelength bandwidths for hyperspectral measurements; 2) Differences exist in signal strength as a function of wavelength and bandwidth which may serve as a basis for Space Object Identification applications. Hyperspectral analysis of space objects warrants further investigation.

# HYPERSPECTRAL ANALYSIS OF SPACE OBJECTS: SIGNAL TO NOISE EVALUATION

## *I. Introduction*

Hyperspectral analysis of space objects is being considered as a means of enhancing Space Object Identification (SOI) capability. This study examines the feasibility of hyperspectral analysis from a Signal to Noise perspective. This introductory chapter provides:

- Background
- Problem Statement
- Approach
- Scope
- Summary of key results
- Organization of the thesis

### *1.1 Background*

Hyperspectral analysis involves viewing an object in narrow bandwidths of the electromagnetic spectrum. The wavelength bandwidth is typically on the order of ten nanometers (4:79). In contrast, multispectral analysis typically uses wavelength bandwidths of forty nanometers (5:456). The use of hyperspectral analysis to identify a space object requires a detailed knowledge of the spectral signatures of the materials used to make the object (4:76). A report, *Matter.dat Surface Properties Data Compilation*, contains the spectral reflectances of materials commonly used in

spacecraft construction (14). *Introduction to the Physics and Techniques of Remote Sensing* describes the ideal case for identifying a material using spectral analysis:

...if a certain material, or family of materials, is the only one which has a certain spectral feature, such as an absorption line at a certain wavelength, the identification becomes simple. The identification feature could be a single absorption line, or an association of lines. (4:77)

In a similar way, hyperspectral analysis of space objects may provide a specific signature through "an association of lines" unique to that space object. This hyperspectral signature would enhance Space Object Identification. In addition, hyperspectral analysis may provide insight into a space object's material composition. The two general categories of hyperspectral analysis are hyperspectral imaging and hyperspectrometry. Differentiating imaging from spectrometry is discussed in *Chapter II*. Hyperspectral analysis is being considered for ground-based and space-based sensors (12) (11). The ground-based sensor is a 1.6 m diameter telescope located in Maui, Hawaii. A proposed space-based sensor, part of the Space Surveillance Initiative (SSI) research program (11), may have a hyperspectral sensor as part of its mission suite.

### *1.2 Problem Statement*

Develop a mathematical simulation based on fundamental radiometry principles to evaluate the feasibility of hyperspectral analysis of space objects.

### *1.3 Approach*

The key metric in determining a sensor's feasibility and performance is the Signal to Noise Ratio (SNR). The SNR is a function of the target signal, noise, and integration time. This SNR evaluation addresses the question: Is there enough target signal in narrow wavelength bandwidths to conduct hyperspectral measurements? The approach of this thesis is to characterize the target signal and noise sources using fundamental radiometry. The integration time is case dependent, and



is approached from a best case, worst case standpoint to bound the integration time. The equations derived from the radiometry are evaluated in a mathematical simulation using Mathcad 3.1 (6). This radiometry model is applied to four case studies: two involve hyperspectral imaging, and two involve hyperspectrometry.

#### *1.4 Scope*

1. This study considers the radiometry from point to point, no atmosphere. The radiometry model developed for the SNR evaluation can be applied to ground-based (first order approximation with no atmosphere) or space-based sensors.
2. The sensor is tracking the target.
3. Background noise is small compared to the target signal, so background noise is negligible.
4. Spectral reflectance of materials is not linked to spatial coordinates.
5. Direct solar irradiance is the sole source of energy used in the radiometry development.
6. The detector for this study is a Charge Coupled Device (CCD).

#### *1.5 Summary of Key Results*

For Case (1) and Case (2), the target was modeled as rocket body 6 m long and 2 m in diameter. The range to the target was assumed to be 800 km. For Case(1), the rocket body had an aluminum surface. For Case (2), the rocket body was painted white. For Case (3) and Case (4), the targets were modeled as cylindrical communications satellites in geosynchronous orbit. Range to the targets was 36,000 km. For Case (3), the satellite was 7.6 m long and 3.64 m in diameter, and has an antenna 2.4 m in diameter on top of the cylinder. For Case (4), the satellite is 4.77 m long and 2.2 m in diameter, and has an antenna 1.83 m in diameter on top

of the cylinder. The sensor viewing the targets for all cases was a 1.6 m diameter telescope. For the cases studied:

1. Enough signal is present for hyperspectral imaging and hyperspectrometry for narrow wavelength bandwidths of  $\Delta \lambda = 20 \text{ nm}, 10 \text{ nm},$  and  $5 \text{ nm}.$
2. Analysis of the radiometry model for different materials and objects shows differences in signal strength as a function of wavelength which may serve as a basis for Space Object Identification.

### 1.6 Organization

- *Chapter I, Introduction.*
- *Chapter II, Theory.* Establishes the theoretical basis for the radiometry model.
- *Chapter III, Results.* Outlines the procedures for running the radiometry model, and presents the results from the four case studies.
- *Chapter IV, Conclusions & Recommendations.* Provides a summary of the study, the key results, corollary issues, and recommendations for further research.
- *Appendix A.* Contains the Mathcad code used to develop the radiometry model.
- *Appendices B-E.* Contains the graphical output for the four case studies.
- *Appendix F.* Contains plots of spectral reflectance versus wavelength for the materials used in the case studies.

## II. Theory

### 2.1 Introduction

The main metric for determining the feasibility of an imaging system is Signal to Noise Ratio (SNR). SNR is a measure of a system's ability to discriminate between the target signal and noise. Noise originates from photon shot noise, the background, and the detector. The following sections address the theory and methodology for determining:

- target signal
- background noise
- detector noise
- integration time
- SNR

### 2.2 Target Signal

**2.2.1 Introduction.** Radiometry determines the target signal incident on the detector. For this evaluation, the radiometry is derived from first principles. The result of the radiometry derivation is an expression for the average count rate from the detector. The count rate is proportional to the strength of the target signal, and can be expressed in terms of target, sensor, and source parameters. The final count rate equation includes simplifications used in the Mathcad radiometry model.

**2.2.2 Radiometry.** Radiometry determines the number of photons incident on the detector. The detector generates a count rate based on the strength of the target signal. The count rate from the detector(10) is

$$\frac{i_T}{q} = \int \frac{\Phi_e(\lambda)}{\varepsilon(\lambda)} \eta(\lambda) d\lambda \quad (2.1)$$

where,

$\frac{i_T}{q}$  = count rate from detector (1/s)

$\Phi_e(\lambda)$  = power incident on the detector (W)

$\epsilon(\lambda)$  = photon energy (J)

$\eta(\lambda)$  = detector quantum efficiency

$\lambda$  = wavelength (m).

The photon energy is

$$\epsilon(\lambda) = \frac{hc}{\lambda} \quad (2.2)$$

where,

$h$  = Planck's constant =  $6.626 \times 10^{-34}$  J s

$c$  = speed of light, vacuum =  $3 \times 10^8$  m/s.

The power incident on the detector in terms of detecting optic area and target irradiance (10) is

$$\Phi_e(\lambda) = S_R E_T(\lambda) \tau_o(\lambda) \quad (2.3)$$

where,

$S_R$  = area of detecting optic ( $m^2$ )

$E_T(\lambda)$  = irradiance at the sensor due to the target ( $W/m^2$ )

$\tau_o(\lambda)$  = optical transmission.

The target irradiance at the sensor (10) is

$$E_T(\lambda) = \frac{L_T(\lambda) S_T}{r^2} \cos(\theta_1) \quad (2.4)$$

where,

$L_T(\lambda)$  = target radiance ( $W/m^2 sr$ )

$S_T$  = target area ( $m^2$ )

$r$  = range to target ( $m$ )

$\theta_1$  = target-sensor angle.

The target-sensor angle (and source-target angle described below) are measured with respect to the surface normal of the target (Figure 2.1).

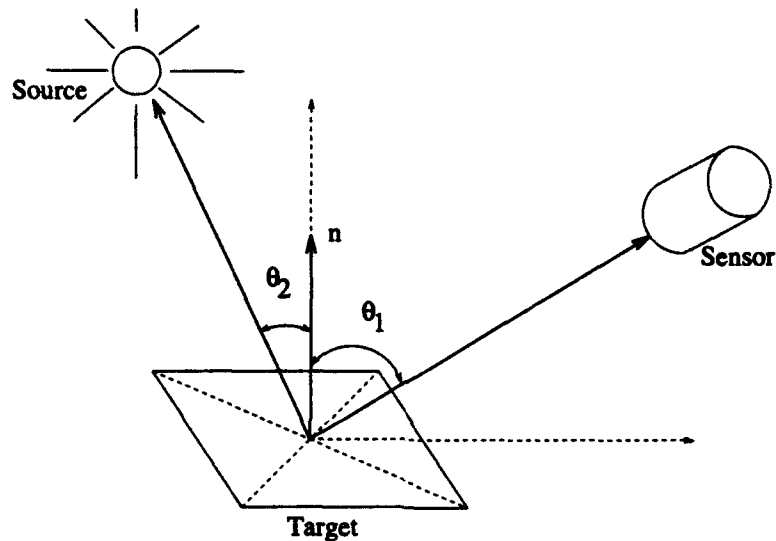


Figure 2.1 Target-sensor and source-target angles

To express the radiance of the target in terms of irradiance from a source, the target is assumed to be Lambertian (2:22), and

$$L_T(\lambda) = \frac{M_T(\lambda)}{\pi} \quad (2.5)$$

where,

$M_T(\lambda)$  = target exitance ( $W/m^2$ ).

The target exitance (10) equals

$$M_T(\lambda) = E_{source}(\lambda) \rho(\lambda) \quad (2.6)$$

where,

$E_{source}(\lambda)$  = irradiance of the source at the target ( $W/m^2$ )

$\rho(\lambda)$  = spectral reflectivity.

For this analysis, the sun is the only source of irradiance on the target

$$E_{source}(\lambda) = E_{sun}(\lambda) \cos(\theta_2) \quad (2.7)$$

where,

$E_{sun}(\lambda)$  = irradiance of the sun at the target ( $W/m^2$ )

$\theta_2$  = source-target angle

The resulting expression for the count rate is

$$\frac{i_T}{q} = \frac{S_R}{r^2} \cos(\theta_1) \cos(\theta_2) S_T \int \frac{E_{sun}(\lambda)}{h c \pi} \rho(\lambda) \tau_o(\lambda) \eta(\lambda) \lambda d\lambda \quad (2.8)$$

Although  $h$ ,  $c$ , and  $\pi$  are not dependent on wavelength, retaining these constants in the integral will allow Equation 2.8 to be calculated in terms of a photon flux, described in Section 2.2.3. The elements of Equation 2.8 can be categorized according to target, sensor and source parameters. (Table 2.1) The following subsections describe each of the parameters listed in Table 2.1.

Target	Sensor	Source
$S_T$	$\lambda^1$	$E_{sun}(\lambda)$
$\rho(\lambda)$	$\Delta \lambda$	$\theta_2$
$r$	$S_R$	
$\theta_1$	$\tau_o(\lambda)$	
	$\eta(\lambda)$	

Table 2.1 Target, Sensor, and Source Parameters

### 2.2.2.1 Target Parameters.

Target Area ( $S_T$ ): As target area increases, the count rate increases. Target size can vary from a few centimeters to greater than 10 m in length.

Spectral Reflectivity ( $\rho(\lambda)$ ): Spectral reflectivity varies for each material with  $0 < \rho(\lambda) < 1$ , and is dependent on wavelength.

Range to target ( $r$ ): The count rate decreases by the square of the range to the target.

Target-sensor angle ( $\theta_1$ ): For this analysis, the target-sensor angle has a range of  $0 \text{ deg} < \theta_1 < 90 \text{ deg}$ , therefore  $1 > \cos(\theta_1) > 0$ . The count rate is a maximum for normal incidence, when  $\theta_1 = 0 \text{ deg}$ . This analysis only considers the sensor viewing one side of the target.

### 2.2.2.2 Sensor Parameters.

Wavelength ( $\lambda$ ): The wavelength identifies which portion of the electromagnetic spectrum the sensor uses. Wavelength for the different case studies varies from 300 nanometers (nm) as the lowest wavelength, to 850 nm as the highest (9). The choice of detector will limit the wavelengths of the sensor. A thinned CCD with an antireflective coating will have a quantum efficiency greater than 50 percent for the wavelength region of  $300 \text{ nm} < \lambda < 900 \text{ nm}$  (7).

Wavelength bandwidth ( $\Delta \lambda$ ): The wavelength bandwidth gives the width of the divisions within the wavelength interval. For this analysis, wavelength bandwidths support Phillips Lab's goal of hyperspectral imaging at wavelength bandwidths of twenty, ten and five nanometers (13).

Area of detecting optic ( $S_T$ ): As the area of detecting optic increases, the count rate increases.

Optical transmission ( $\tau_o(\lambda)$ ): Although dependent on wavelength, the optical transmission will not vary significantly. The optical transmission was set as a constant,  $\tau_o = .98$ .

---

<sup>1</sup>Since the wavelength detected by the sensor is a subset of the wavelength emitted by the source, wavelength is categorized as a sensor parameter.

Detector quantum efficiency ( $\eta(\lambda)$ ): The quantum efficiency ranges from  $0 < \eta(\lambda) < 1$ . For a thinned CCD detector with an antireflective coating, the peak quantum efficiency is approximately 70 percent at 750 nm (7). For the wavelengths used in this analysis, the quantum efficiency will not drop below 50 percent. Since quantum efficiency between the maximum and minimum only differs by 20 percent, the quantum efficiency was set as a constant,  $\eta = .6$ .

**2.2.2.3 Source Parameters.** Irradiance of the sun ( $E_{sun}(\lambda)$ ): To determine the irradiance of the sun at the target, the sun is modeled as a 5770 K blackbody (15). The spectral exitance from the sun is given by Planck's formula (4:35)

$$M_{bb}(\lambda) = \frac{2 \pi h c^2}{\lambda^5 \left[ \exp\left(\frac{h c}{\lambda k_B T}\right) - 1 \right]} \quad (2.9)$$

where,

$$\begin{aligned} h &= \text{Planck's constant} &= 6.626 \times 10^{-34} \text{ J s} \\ c &= \text{speed of light, vacuum} &= 3 \times 10^8 \text{ m/s} \\ \lambda &= \text{wavelength (m)} \\ k_B &= \text{Boltzmann's constant} &= 1.38 \times 10^{-23} \text{ J/K} \\ T &= \text{temperature (K)} \end{aligned}$$

The irradiance of the sun at the target is given by the inverse square law (2:25)

$$E_{sun}(\lambda) = M_{bb}(\lambda) \left( \frac{R_{sun}}{r_{sun}} \right)^2 \quad (2.10)$$

where,

$$\begin{aligned} M_{bb}(\lambda) &= \text{exitance from the sun (W/m}^2\text{)} \\ R_{sun} &= \text{radius of the sun} &= 6.96 \times 10^8 \text{ m} \\ r_{sun} &= \text{distance to the sun} &= 1.5 \times 10^{11} \text{ m} \end{aligned}$$



Source-target angle ( $\theta_2$ ): For this analysis, the source-target angle has a range of  $0 \text{ deg} < \theta_2 < 90 \text{ deg}$ , therefore  $1 > \cos(\theta_2) > 0$ . The count rate is a maximum for normal incidence, when  $\theta_2 = 0 \text{ deg}$ . This analysis only considers the irradiance on one side of the target.

*2.2.3 Target Count Rate Equation.* To simplify the count rate equation (Equation 2.8), the optical transmission and quantum efficiency will not depend on wavelength, so the form of the count rate equation is

$$\frac{i_T}{q} = \frac{S_R}{r^2} \cos(\theta_1) \cos(\theta_2) \tau_o S_T \eta \int \frac{E_{sun}(\lambda)}{h c \pi} \rho(\lambda) \lambda d\lambda \quad (2.11)$$

A major difficulty with this equation is the number of parameters that vary. Target area, range, encounter angles, and area of detecting optic vary depending on the scenario. A means of simplifying this equation is through a hypernormalized parameter

$$\Omega = \frac{S_R}{r^2} \cos(\theta_1) \cos(\theta_2) \tau_o S_T \eta \quad (2.12)$$

The hypernormalized parameter models a wide range of cases, and allows the model to focus on the outcome — the target count rate. *Chapter III* contains a section which illustrates the usefulness of the hypernormalized parameter. With the hypernormalized parameter, the count rate equation simplifies to

$$\frac{i_T}{q} = \Omega \int \frac{E_{sun}(\lambda)}{h c \pi} \rho(\lambda) \lambda d\lambda \quad (2.13)$$

To extract the spectral reflectivity from the integral, the spectral reflectivity values from a given material are treated as a vector. Each element of the vector corresponds to the mean wavelength of the integral. For instance, for limits of integration of 445 nm to 455 nm ( $\Delta\lambda = 10 \text{ nm}$ ), the spectral reflectivity corresponds to wavelength 450 nm. With the spectral reflectivity removed from the integral, the count rate

equation is

$$\frac{i_T}{q} = \Omega \rho \int \frac{E_{sun}(\lambda)}{h c \pi} \lambda d\lambda \quad (2.14)$$

The remaining terms in the integral are the irradiance of the sun, the wavelength, and constants  $h$ ,  $c$ , and  $\pi$ . From Equation 2.10, the irradiance of the sun is determined by Planck's formula and the inverse square law. By including the other terms in the integral ( $h, c, \lambda$ ), the resulting output is a photon flux,  $P$ , in units  $1/(m^2 s)$ . The resulting expression for the target count rate is

$$\frac{i_T}{q} = \Omega \rho \frac{P}{\pi} \quad (2.15)$$

where,

- $\Omega$  = hypernormalized parameter ( $rad m^2$ )
- $\rho$  = spectral reflectivity
- $P$  = photon flux ( $1/(m^2 s)$ )

### 2.3 Background Noise

Background noise sources include the celestial background, earthlimb, aurora, airglow, and zodiacal light (3:46). These noise sources will decrease SNR. The background signal is weak compared to the target signal. The background count rate (10) is determined by

$$\frac{i_B}{q} = \frac{L_B S_R \Gamma_R \eta}{h c} \bar{\lambda} \quad (2.16)$$

where,

- $L_B$  = background radiance ( $W/m^2 sr$ )
- $S_R$  = detecting optic area ( $m^2$ )
- $\Gamma_R$  = detector solid angle ( $sr$ )
- $\eta$  = quantum efficiency
- $h$  = Planck's constant ( $J s$ )
- $c$  = speed of light, vacuum ( $m/s$ )
- $\bar{\lambda}$  = average wavelength of sensor ( $m$ )

For a sensor viewing deep space, the radiance of the celestial background is  $L_B = 2 \times 10^{-6} W/m^2 sr$  (3:54). For a sensor with a 1.6 m diameter collecting optic and a CCD detector with pixel size  $20 \mu m$  (7:8),  $S_R = 2.01 m^2$  and  $\Gamma_R \approx 4 \times 10^{-10} sr$ . Using  $\eta = .6$  and an average wavelength of  $\bar{\lambda} = 600 nm$ , the count rate is  $i_B/q = 2,912$  or roughly  $10^3$ . Target count rates are greater than background noise by at least an order of magnitude. (For the case studies developed in the next chapter, target count rates range from  $10^4$  to  $10^8$ .) Since the target signal dominates the background noise, background noise is assumed negligible in this analysis.

#### 2.4 Detector Noise

Detector noise for a CCD is from read noise. The read noise for a CCD detector ranges from  $\sigma_{rn} = 6 e^-$  to  $\sigma_{rn} = 20 e^-$  or higher depending on the choice of CCD and intended application (8). For this analysis, the CCD read noise is assumed to be  $\sigma_{rn} = 12 e^-$  (7), which corresponds to a CCD detector having high quantum efficiency in the wavelength region 300 nm to 900 nm (8). In terms of a detector noise count rate, the detector noise is  $i_D/q = 12 sec^{-1}$ .

#### 2.5 Integration Time

Integration time is limited by target-sensor viewing geometry, time in coverage, target stability, and the relative velocity between target and sensor. The integration time is case dependent. A complicating factor in hyperspectral analysis is the small

wavelength bandwidth. Integration time must be longer to reach the same SNR as a system with a large wavelength bandwidth. What is a reasonable integration time for hyperspectral analysis? The approach in this analysis uses a long integration time of  $t_d = 8\text{ s}$  to determine if hyperspectral analysis is feasible for long, best case integration times. If hyperspectral analysis is feasible for long integration times, the shortest possible integration time is calculated by setting a minimum SNR threshold and solving for the integration time.

## 2.6 Signal to Noise Ratio

The general form of the SNR equation is (10)

$$SNR = \frac{\overline{K_S}}{\sqrt{\overline{K_S} + \overline{K_B} + \sigma_{rn}^2}} \quad (2.17)$$

where,

$\overline{K_S}$  = average number of photon events caused by desired signal (*counts*)

$\overline{K_B}$  = average number of photon events caused by background (*counts*)

$\sigma_{rn}$  = read noise of detector ( $e^-$ ).

In this analysis, background is negligible (Section 2.3), so Equation 2.17 simplifies to

$$SNR = \frac{\overline{K_S}}{\sqrt{\overline{K_S} + \sigma_{rn}^2}} \quad (2.18)$$

Equation 2.18 is used to derive SNR equations for imaging and spectrometry cases.

**2.6.1 SNR Equation for Imaging.** For the imaging case, light is divided among the individual detectors or pixels in the detector array. The SNR per pixel,

or  $SNR_{pix}$ , is a measure of the signal to noise ratio for each individual detector. To determine if the sensor is imaging, the angular subtense of the diffraction limited spot is compared to the target's angular subtense. The angular subtense of the diffraction limited spot is

$$\Delta\phi_{min} = 1.22 \frac{\lambda}{D} \quad (2.19)$$

where,

$\lambda$  = wavelength (m)

$D$  = diameter of primary optic (m).

The target angular subtense is

$$\Delta\phi_{sat} = \frac{L_T}{r} \quad (2.20)$$

where,

$L_T$  = length of target (m)

$r$  = range to target (m).

If  $\Delta\phi_{min} < \Delta\phi_{sat}$ , the system can image the object. This is a rudimentary definition of imaging, and does not consider resolution criteria. The  $SNR_{pix}$  equation, from 2.18 with  $\overline{K_S} = \overline{K_{pix}}$ , is

$$SNR_{pix} = \frac{\overline{K_{pix}}}{\sqrt{\overline{K_{pix}} + \sigma_{rn}^2}} \quad (2.21)$$

where,

$\overline{K_{pix}}$  = average number of photon events per pixel exposed

$\sigma_{rn}$  = read noise of detector ( $e^-$ ).

To express  $\overline{K_{pix}}$  in terms of the number of detectors exposed by a target (10),

$$\overline{K_{pix}} = \frac{\overline{K_T}}{N_{pix}^2} \quad (2.22)$$

where,

$\overline{K_T}$  = average number of photon events caused by target (*counts*)

$N_{pix}$  = number of pixels exposed by target in one dimension.

The average number of photon events caused by the target (10) is

$$\overline{K_T} = \frac{i_T}{q} t_d \quad (2.23)$$

where,

$\frac{i_T}{q}$  = count rate from the detector (1/s)

$t_d$  = integration time (s).

The number of pixels exposed by a target in one dimension depends on the target's angular subtense and the detector angular subtense (10)

$$N_{pix} = \frac{\Delta\phi_{sat}}{das} \quad (2.24)$$

where,

$\Delta\phi_{sat}$  = target angular subtense (*rad*)

$das$  = detector angular subtense (*rad*).

The detector area subtense expressed in terms of a detector size and focal length is (10)

$$das = \frac{d}{f} \quad (2.25)$$

where,

$d$  = detector size (m)

$f$  = focal length (m).

To avoid specifying a focal length for the sensor, the detector area subtense was assumed to be equal to the diffraction limited spot,

$$das = \Delta\phi_{min}. \quad (2.26)$$

When Equations 2.19, 2.20, 2.23, are substituted into Equation 2.21, the  $SNR_{pix}$  expression becomes

$$SNR_{pix} = \frac{\frac{i_T}{q} t_d \left( \frac{1.22 r \lambda}{L_T D} \right)^2}{\sqrt{\frac{i_T}{q} t_d \left( \frac{1.22 r \lambda}{L_T D} \right)^2 + \sigma_{rn}^2}} \quad (2.27)$$

If  $S_T \approx L_T^2$  and  $S_R \approx D^2$ , Equation 2.27 becomes

$$SNR_{pix} \approx \frac{\frac{i_T}{q} t_d \frac{(1.22 r \lambda)^2}{S_T S_R}}{\sqrt{\frac{i_T}{q} t_d \frac{(1.22 r \lambda)^2}{S_T S_R} + \sigma_{rn}^2}} \quad (2.28)$$

When the hypernormalized parameter (Equation 2.12) and the count rate equation (Equation 2.15) are substituted into the  $SNR_{pix}$  equation, the parameters  $S_R$ ,  $S_T$ , and  $r^2$  cancel. When an object exposes more than one detector, imaging is possible, and the area of the detecting optic  $S_R$ , target area  $S_T$ , and range  $r$ , drop out of the imaging SNR calculation. To make this approximation, the range, target area, and area of detecting optic cannot vary, which negates the use of the hypernormalized parameter. By assuming  $das = \Delta\phi_{min}$ , the area of the detecting optic is hidden with the equation as part of the number of pixels exposed by the target  $N_{pix}$ .

Cancelling  $S_R$ ,  $S_T$ , and  $r^2$ , the  $SNR_{pix}$  equation becomes

$$SNR_{pix} \approx \frac{P \rho t_d 1.22^2 \lambda^2 \cos(\theta_1) \cos(\theta_2) \tau_0 \eta}{\sqrt{P \rho t_d 1.22^2 \lambda^2 \cos(\theta_1) \cos(\theta_2) \tau_0 \eta + \sigma_{rn}^2}} \quad (2.29)$$

The constants and angles can be grouped into a single parameter

$$z = 1.22^2 \cos(\theta_1) \cos(\theta_2) \tau_0 \eta \quad (2.30)$$

The parameter  $z$  is a maximum when the encounter angles equal zero, and quantum efficiency is a maximum. ( $\theta_1 = \theta_2 = 0$  deg,  $\eta_{max} = .7$ ). The maximum value for  $z$  is  $1.02 \approx 1$ . When the parameter  $z$  varies between 0 and 1, the model simulates encounter angles going from 90 deg to 0 deg. The final expression for  $SNR_{pix}$  is

$$SNR_{pix} = \frac{P \rho t_d \lambda^2 z}{\sqrt{P \rho t_d \lambda^2 z + \sigma_{rn}^2}} \quad (2.31)$$

**2.6.2 SNR Equation for Spectrometry.** In contrast to the imaging case, for spectrometry light is incident on a single detector. The single pixel SNR is given by Equation 2.18 with  $\overline{K_S} = \overline{K_T}$

$$SNR = \frac{\overline{K_T}}{\sqrt{\overline{K_T} + \sigma_{rn}^2}} \quad (2.32)$$

where,

$\overline{K_T}$  = average number of photon events per integration time caused by target (counts)

$\sigma_{rn}$  = read noise of detector ( $e^-$ ).



Using Equation 2.23 and expressing the read noise in terms of a count rate from the detector, the single pixel SNR (10) is

$$SNR = \frac{\frac{i_T}{q} \sqrt{t_d}}{\sqrt{\frac{i_T}{q} + \frac{i_D}{q}}} \quad (2.33)$$

where,

$$\begin{aligned} \frac{i_T}{q} &= \text{target signal count rate (1/s)} \\ \frac{i_D}{q} &= \text{detector noise count rate (1/s)} \\ t_d &= \text{integration time (s)} \end{aligned}$$

Three tools are in place for the SNR evaluation: the target signal count rate, and the SNR expressions for imaging and spectrometry. The target signal count rate was developed from basic radiometry. Other elements required for the SNR evaluation are the background noise, detector noise, and integration time. Background noise is small compared to the target signal, and is assumed negligible. *Detector noise is modeled on a CCD detector, with  $\sigma_{rn} = 12e^-$ . Integration time is case dependent, but can be bounded by running models for a best case scenario with a long integration time, and then setting an SNR threshold and solving for the shortest possible integration time for a worst case scenario. When the signal is incident on more than one detector, the  $SNR_{pix}$  determines if enough signal is present in each pixel for imaging. The single pixel SNR is useful for spectrometry, when the diffraction limited spot falls on one detector.*

### III. Results

#### 3.1 Introduction

The target signal count rate, SNR and  $SNR_{pix}$  were calculated for four cases. Two cases concern hyperspectral imaging and two concern hyperspectrometry. This chapter outlines the procedures for running a case study and presents the results for the hyperspectral imaging and hyperspectrometry case studies.

#### 3.2 Procedure

To run a case study, the procedure involves specifying a configuration, determining the spectral reflectance of the target, running the radiometry model, and calculating the minimum integration time.

*3.2.1 Configuration.* The model configuration determines the system's imaging ability and the hypernormalized parameter. The imaging determination compares the target angular subtense  $\Delta \phi_{sat}$  (Equation 2.20) to the angular subtense of the diffraction limited spot,  $\Delta \phi_{min}$  (Equation 2.19). The  $\Delta \phi_{min}$  calculation uses a maximum wavelength of 900 nm to give the largest diffraction limited spot angular subtense for the wavelength region of 300–900 nm. If the system can image the target, the number of pixels,  $N_{pix}$ , can be determined (Equation 2.24) since  $\Delta \phi_{min} = das$ ,

$$N_{pix} = \frac{\Delta \phi_{sat}}{\Delta \phi_{min}}.$$

The hypernormalized parameter calculated in the configuration is a reference point used in the case studies. The reference hypernormalized parameter  $\Omega_{ref}$  is the maximum  $\Omega$  for normal incidence of the target-sensor angle ( $\theta_1$ ) and the source-target angle ( $\theta_2$ ).  $\Omega_{ref}$  determines the bound for the hypernormalized parameter in

the radiometry model, and is the basis of comparison between two models. Appendix A (page A-3) contains the Mathcad Configuration code.

**3.2.2 Spectral Reflectance Interpolation.** The spectral reflectance values for a given material are compiled in the *Matter.dat Surface Properties Data Compilation* (14). This compilation contains spectral reflectance values for materials commonly used on spacecraft. The spectral reflectance data is given in tabular (spectral reflectances for an increment of 10 nm) and graphical form. Figure 3.1 shows an example spectral reflectance plot for solar cells, Surface Material Code 23 (SMC-23).

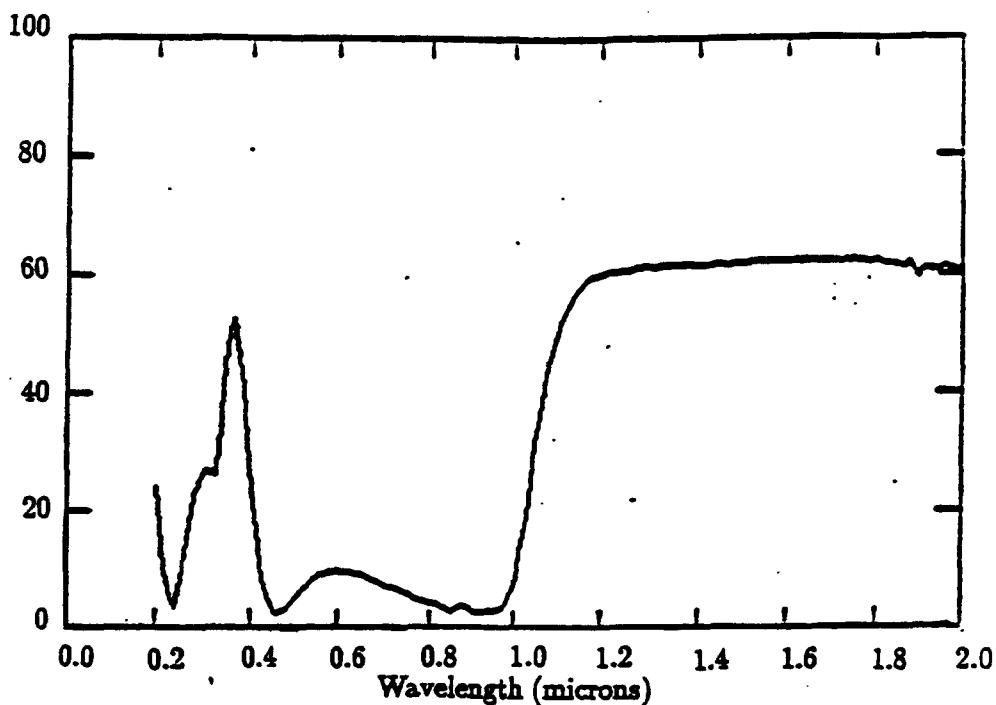


Figure 3.1 Spectral Reflectance (%), SMC-23: Solar Cell, Silicon

Appendix G contains the spectral reflectance graphs for the five materials used in the case studies. The wavelength increment in the compilation is  $\Delta \lambda = 10$  nm. To use the  $\Delta \lambda = 20$  nm and  $\Delta \lambda = 5$  nm models, a Mathcad interpolation routine converts the 10 nm increment into 20 nm and 5 nm increments. Interpolating to 5 nm assumes that the spectral reflectance values in the *Matter.dat Surface Properties Data Compilation* are continuous. (Appendix A, pages A-4 through A-6.)

**3.2.3 Radiometry Model.** The radiometry model calculates the count rate, SNR and  $SNR_{pix}$ . Inputs to the model include:

- wavelength lower and upper bound
- wavelength bandwidth
- spectral reflectance data file
- range of the hypernormalized parameter
- integration time
- detector noise
- fractional material areas

The radiometry model outputs data to graphs.

**3.2.3.1 Wavelength Lower and Upper Bound.** From Section 2.2.2.2, the wavelength region is 300–900 nm. To match the spectral reflectance values to the center of the wavelength bandwidth,  $\lambda_{lb} = 300 - (\Delta \lambda / 2)$  and  $\lambda_{ub} = 900 + (\Delta \lambda / 2)$ . The wavelength lower and upper bound, the wavelength bandwidth, and a counter ( $i$ ) are used to determine the limits of integration for the photon flux calculation.

**3.2.3.2 Wavelength Bandwidth.**  $\Delta \lambda = 20$  nm, 10 nm, or 5 nm.

**3.2.3.3 Spectral Reflectance Data File.** The spectral reflectance is read from a data file specific to material and wavelength. The term  $\rho_{23}$  means spectral reflectance for Surface Material Code 23 (SMC-23).

**3.2.3.4 Hypernormalized Parameter.** The hypernormalized parameter allows the modeling of a wide range of cases in one radiometry calculation. Section 3.3.1.5 illustrates the application of  $\Omega$  for Case (1). To accomplish the modeling, the bound of the hypernormalized parameter  $\Omega$  is varied by an order of magnitude

above and below  $\Omega_{ref}$ 's exponent. For example, if  $\Omega_{ref} = 10^{-11}$ , the range for  $\Omega$  is  $10^{-12} \dots 10^{-10}$ .

**3.2.3.5 Integration Time.** From Section 2.5, the integration time is  $t_d = 8$  s. This models a best case scenario. Section 3.2.4 discusses the best and worst case integration time approach for this analysis.

**3.2.3.6 Detector Noise.** From Section 2.4, the detector noise is  $i_D = 12 q \text{ sec}^{-1}$  or  $\sigma_{rn} = 12$ .

**3.2.3.7 Fractional Material Areas.** When a case study involves an object made of different materials, the fractional material areas are used to weight the target's count rate. For example, an object made of 70 percent solar array (SMC-23) and 30 percent aluminum (SMC-02) would have a count rate expression weighted as

$$i_{T(total)} = .70 i_{T(23)} + .30 i_{T(02)}$$

**3.2.4 Example Input and Output.** With all the input parameters defined, the radiometry model executes and presents the results in three graphs. An example of the input required and resulting output follows. The example is for Case (1),  $\Delta\lambda = 10$  nm.

Input parameters:

- wavelength lower and upper bound:  $\lambda_{lb} = 295$  nm and  $\lambda_{ub} = 905$  nm
- wavelength bandwidth:  $\Delta\lambda = 10$  nm
- spectral reflectance data file: smc02xx.dat (smc02=Surface Material Code 02; xx for 20 nm)
- range of the hypernormalized parameter:  $\Omega = 10^{-12} \dots 10^{-10}$

- integration time:  $t_d = 8 s$
- detector noise:  $i_D = 12 q \text{ sec}^{-1}$  or  $\sigma_{rn} = 12$
- fractional material areas: None (object is made entirely of SMC-02)

Output: The output from the radiometry model is three graphs; Figure 3.2, Figure 3.3, and Figure 3.4<sup>1</sup>. Figure 3.2 shows the count rate ( $i_T/q$ ) vs  $\Omega$  for Case (1),  $\Delta \lambda = 10 \text{ nm}$ . The graph is a log-log plot, with the target signal count rate,  $i_T/q$ , graphed on the vertical axis, and  $\Omega$  graphed on the horizontal axis. The vertical dashed line is the reference hypernormalized parameter,  $\Omega_{ref}$ , computed for the target. The legend for converting the counter( $i$ ) to the mean wavelength of the interval  $\bar{\lambda}$  (Appendix A, page A-8) is given in Table 3.1. This legend applies to all three

$i$	$\bar{\lambda}$ (nm)
16	450
26	550
36	650
46	750
56	850

Table 3.1 Legend, Case (1), 10 nm

graphs. Figure 3.3 shows the SNR vs  $\Omega$  for Case (1),  $\Delta \lambda = 10 \text{ nm}$ . The graph uses a log plot for the  $\Omega$  axis and normal plot for the SNR on the vertical axis. The vertical dashed line is the reference hypernormalized parameter,  $\Omega_{ref}$ , computed for the target. Figure 3.4 shows the  $SNR_{pix}$  vs  $z$  for Case (1),  $\Delta \lambda = 10 \text{ nm}$ .  $SNR_{pix}$  is plotted on the vertical axis, and  $z$ , the angles parameter, on the horizontal axis. The parameter  $z$  varies from 0-1, simulating encounter angles  $\theta_1$  and  $\theta_2$  going from 90 deg-0 deg. All graphs in this chapter and the appendices follow these three formats.

**3.2.5 Integration Time.** The integration time for this analysis considers a best case and worst case situation. The best case is for a stable target slowly

<sup>1</sup>Figures used in this chapter are duplicated in the appendix.

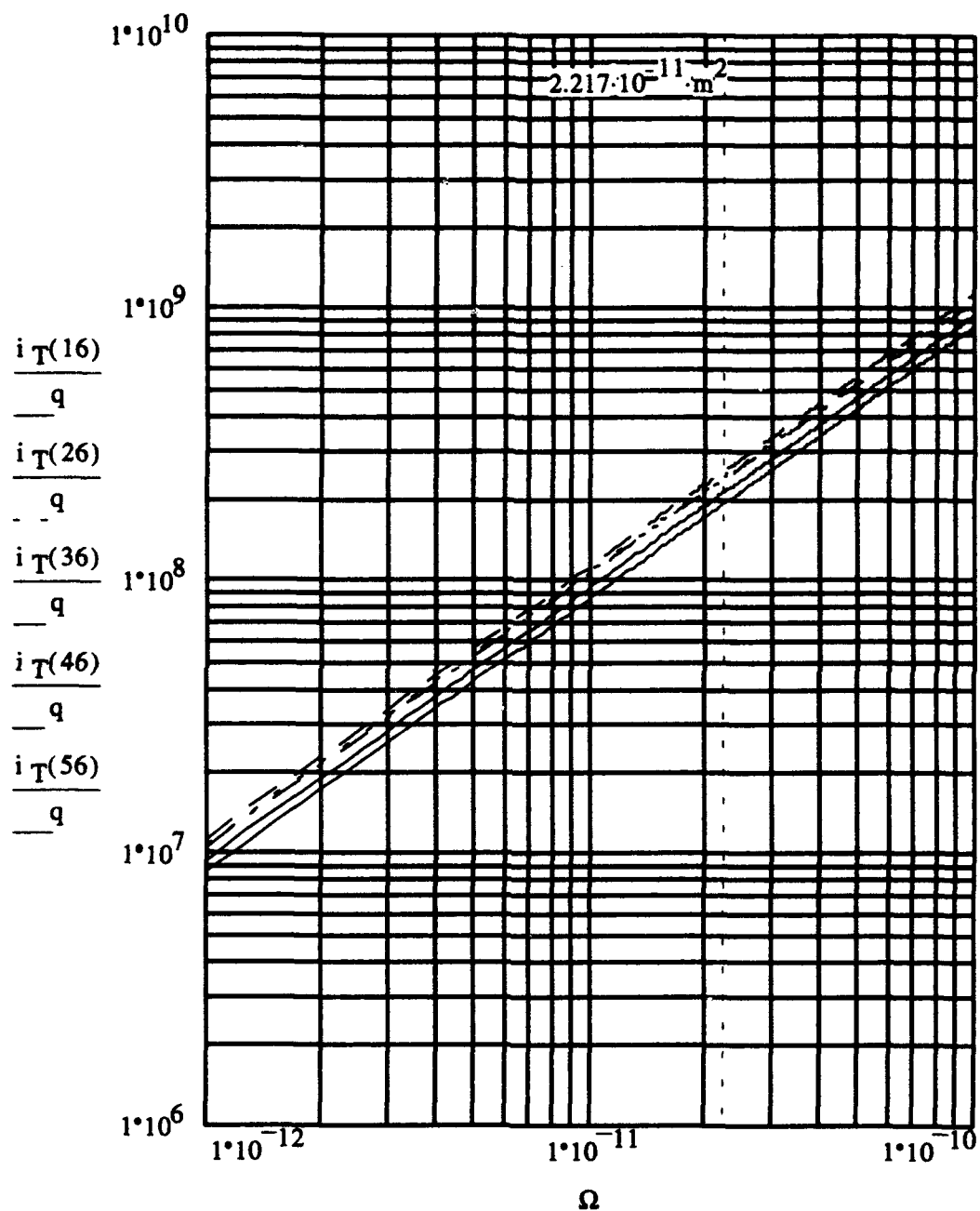


Figure 3.2 Case (1), Count Rate  $\frac{i_T}{q}$  (1/s) vs  $\Omega$  ( $\text{rad m}^2$ ), 10 nm

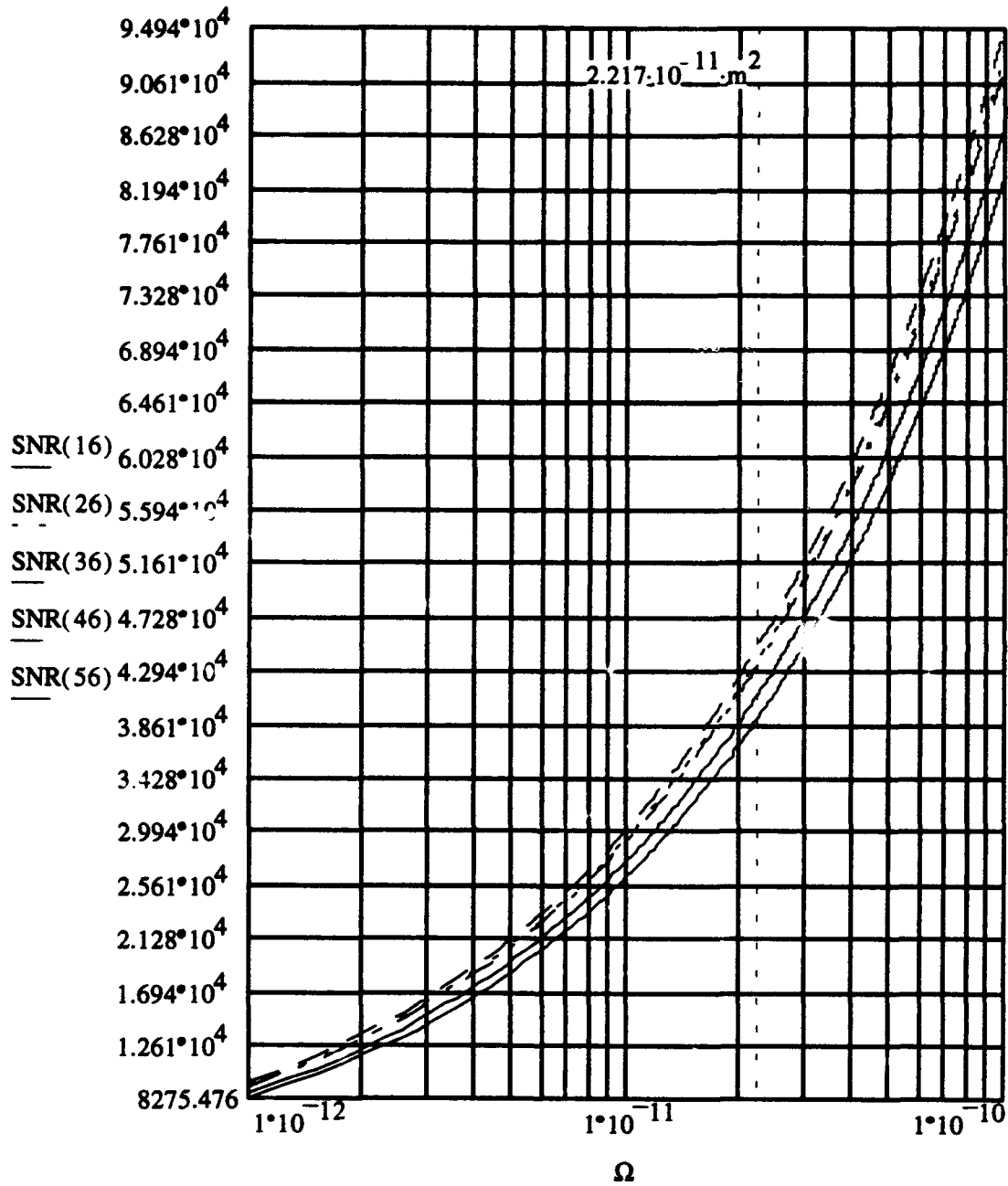


Figure 3.3 Case (1), SNR vs  $\Omega$  ( $\text{rad m}^2$ ), 10 nm



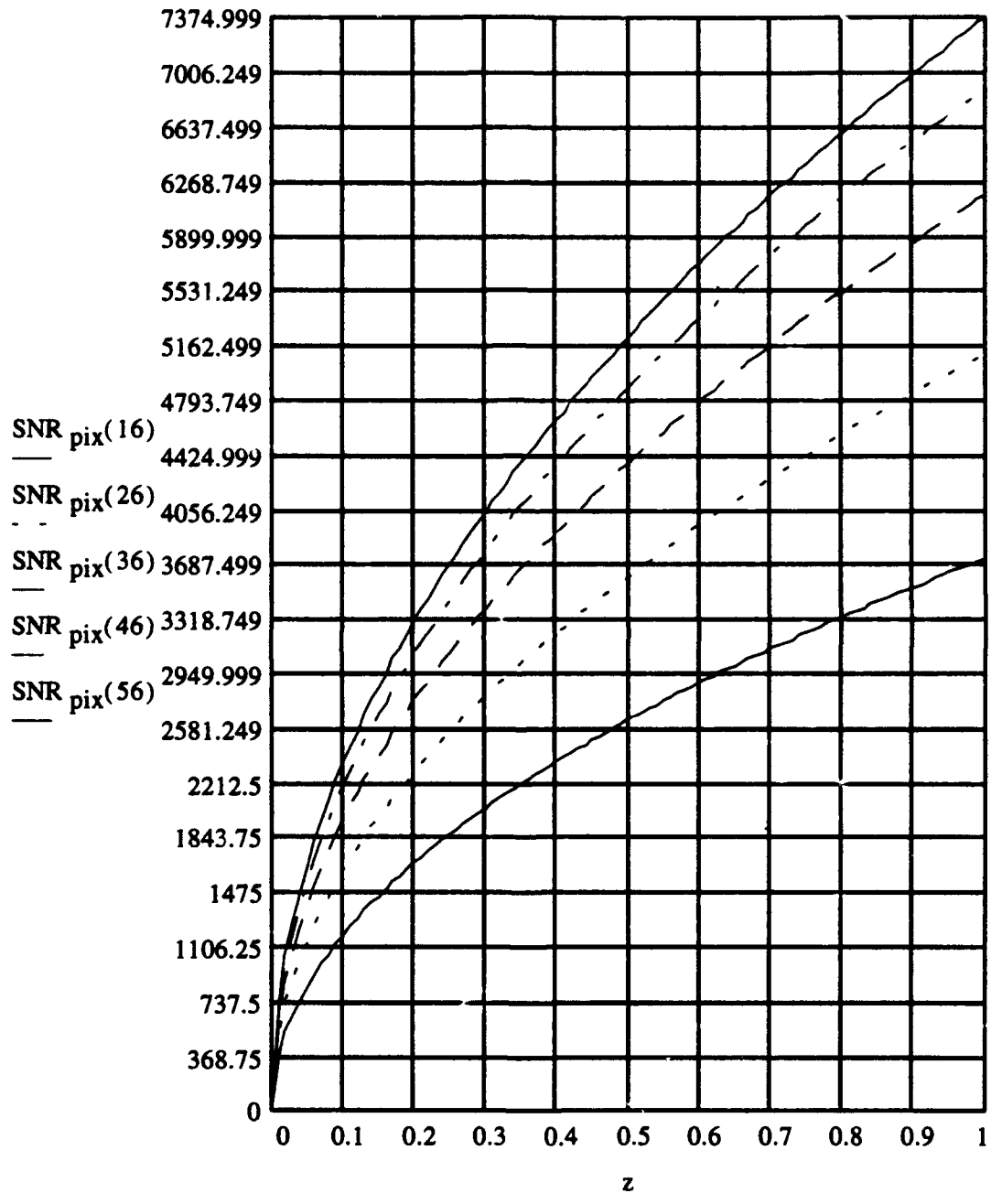


Figure 3.4 Case (1),  $SNR_{pix}$  vs  $z$ , 10 nm

crossing the field of view of the sensor, with little aspect change. For this situation, the integration time is set at  $t_d = 8$  s, the value used in the radiometry models. The worst case is when the target-sensor relative velocity is high, or the target is tumbling, causing radical aspect changes. In this case, the integration time required to achieve a minimum SNR or  $SNR_{pix}$  value was obtained by solving for the integration time in Equation 2.31 and Equation 2.33. When imaging is not possible, the equation for the integration time is

$$t_d = \frac{SNR^2 \left( \frac{i_T}{q} + \frac{i_D}{q} \right)}{\left( \frac{i_T}{q} \right)^2} \quad (3.1)$$

When imaging is possible, the equation for the integration time is

$$t_d = \frac{SNR_{pix}^2 (zH) \pm \sqrt{[SNR_{pix}^2 (zH)]^2 + 4 (zH)^2 SNR_{pix}^2 \sigma_{rn}^2}}{2 (zH)^2} \quad (3.2)$$

where,

$$H = P \rho \lambda^2$$

$$z = 1.22^2 \cos(\theta_1) \cos(\theta_2) \tau_0 \eta$$

For this analysis, the minimum  $SNR_{pix}$  and SNR thresholds are three.

### 3.3 Hyperspectral Imaging

The hyperspectral imaging case studies are for a rocket body in low earth orbit. The case studies are identical, except for Case (1) having an aluminum rocket body and Case (2) having the rocket body covered with white paint (9). After the individual case results are discussed, the two cases are compared with each

other. Three key elements in this comparison are signal strength, line order, and line separation.

### 3.3.1 Case One.

**3.3.1.1 Configuration.** Target: The modeled rocket body is 6 m long and 2 m in diameter. The range to the target is assumed to be 800 km.

Sensor: The sensor is a 1.6 m diameter telescope. The mean wavelengths of interest are 450 nm, 550 nm, 650 nm, 750 nm and 850 nm<sup>2</sup>.

Imaging determination: The maximum target angular subtense is

$$\Delta\phi_{sat} = 7.500 \times 10^{-6} \text{ rad}$$

and the angular subtense of the diffraction limited spot is

$$\Delta\phi_{min} = 6.863 \times 10^{-7} \text{ rad.}$$

$\Delta\phi_{min} < \Delta\phi_{sat}$ , so imaging is possible. The number of pixels exposed by the target is  $N_{pix} \approx 11$ .

Hypernormalized parameter: The reference hypernormalized parameter for normal incidence ( $\theta_1 = \theta_2 = 0 \text{ deg}$ ) is (Equation 2.12)

$$\Omega_{ref} = 2.217 \times 10^{-11} \text{ rad m}^2$$

The range of the hypernormalized parameter in the radiometry model is  $\Omega = 10^{-12} \dots 10^{-10} \text{ rad m}^2$ .

**3.3.1.2 Spectral Reflectance.** The rocket body is made of aluminum, SMC-02 (Figure F.1).

---

<sup>2</sup>For  $\Delta\lambda = 20 \text{ nm}$ , an increment of 20 nm beginning at 300 nm will only give wavelength intervals of interest at 440 nm, 540 nm, 640 nm, 740 nm, and 840 nm.

3.3.1.3 Radiometry results. Table 3.2, Summary of Results, Case (1), shows enough signal is present in each of the wavelength bandwidths to perform hyperspectral imaging. The count rate and SNR values in Table 3.2 correspond to the points where  $\Omega_{ref}$  intersects the plotted lines in Figures B.1–B.9, giving MIN and MAX values as a function of mean wavelength. The  $SNR_{pix}$  values correspond to value  $z = 1$  ( $\theta_1 = \theta_2 = 0$  deg). The lowest count rate is  $9.5 \times 10^7$ , which is roughly five orders of magnitude above the background count rate determined in Section 2.3. The lowest values of SNR and  $SNR_{pix}$  are well above the minimum threshold of three. Appendix B contains a complete set of graphs for Case (1),

CASE 1		Wavelength Bandwidth ( $\Delta \lambda$ )		
		20 nm	10 nm	5 nm
Count rate	MAX	$5.0 \times 10^8$	$2.5 \times 10^8$	$1.3 \times 10^8$
	MIN	$3.6 \times 10^8$	$1.9 \times 10^8$	$9.5 \times 10^7$
SNR	MAX	$6.4 \times 10^4$	$4.4 \times 10^4$	$3.2 \times 10^4$
	MIN	$5.4 \times 10^4$	$3.9 \times 10^4$	$2.7 \times 10^4$
$SNR_{pix}$	MAX	$1.0 \times 10^4$	$0.74 \times 10^4$	$0.52 \times 10^4$
	MIN	$0.50 \times 10^4$	$0.37 \times 10^4$	$0.26 \times 10^4$

Table 3.2 Summary of Results, Case (1)

Figure B.1 to Figure B.9. The set consists of a legend (Table B.1) converting  $i$  to  $\bar{\lambda}$  and graphs of count rate, SNR, and  $SNR_{pix}$  for each of the 20 nm, 10 nm, and 5 nm wavelength bandwidths. The 10 nm and 5 nm curves are very similar due to the interpolation of the spectral reflectance values (compare Figure B.5 to Figure B.8).

The line order and spacing show the target signal's dependence on wavelength and bandwidth. The order of the lines is determined by starting at the lowest plotted line (bottom) corresponding to the mean wavelength with the weakest target signal, and listing successive lines until reaching the line corresponding to the mean wavelength with the largest target signal (top). (Signal strength, line order, and line spacing are used as the basis of comparison between targets.) Line order is

ORDER	20 nm	10 nm	5 nm
Top 5	640	650	650
4	540	550	550
3	740	750	750
2	840	850	850
Bottom 1	440	450	450

Missing horizontal lines indicate overlapping wavelength intervals

Table 3.3 Line Order, Case (1)

not important for  $S R_{pix}$ , since  $SNR_{pix}$  is not dependent on target area, area of detecting optic, and range (see Section 2.6.1). The line order for Case (1), Table 3.3, does not change for the three wavelength bandwidths. Two lines overlap for the 20 nm bandwidth, the 540 nm–740 nm pair (Figure B.2). Overlapping lines do not have a line separating the two wavelength intervals. This convention is used in all line order tables. Possible reasons for the difference between the 20 nm and other cases are the wider wavelength interval and coarser spectral reflectance values from the interpolation of the spectral reflectance data file.

**3.3.1.4 Integration time.** Since imaging is possible, the minimum integration times are calculated using Equation 3.2. The minimum integration times for  $SNR_{pix} = 3$  for each wavelength bandwidth are given in Table 3.4. As the bandwidth decreases, the integration time increases. An integration time in microseconds is very small; however, encounter mechanics such as orbital velocity and target stability may necessitate a very small integration time.

$\Delta \lambda$	$t_d$
20 nm	12.8 $\mu\text{sec}$
10 nm	23.5 $\mu\text{sec}$
5 nm	47.1 $\mu\text{sec}$

Table 3.4 Minimum integration time, Case (1)

3.3.1.5 Using the hypernormalized parameter  $\Omega$ . Why use a hypernormalized parameter? The advantage is one graph indicates a wide range of target-sensor encounters. Three examples illustrate the use of the hypernormalized parameter  $\Omega$ : varying encounter angles; varying target range; and varying the diameter of the sensor's collecting optic. A requirement for these variations is to remain within the bounds of  $\Omega$  for Case (1),  $10^{-12} < \Omega < 10^{-10}$ . The illustrations will use Figure 3.3, Case 1, SNR, 10 nm to show how varying  $\Omega$  applies to the graphs. Since the illustrations use the single pixel SNR, the imaging determination will not be recalculated for varying range and collecting optic diameter.

Basic Case (1): For comparison purposes, Case (1)'s  $\Omega_{ref}$  for  $\theta_1 = \theta_2 = 0$  deg is (Equation 2.12)

$$\Omega_{ref} = 2.217 \times 10^{-11} \text{ radm}^2.$$

Single pixel SNR values from Table 3.2 are  $SNR_{MAX} = 4.4 \times 10^4$  and  $SNR_{MIN} = 3.9 \times 10^4$ .

Varying encounter angles: As the source-target angle and target-sensor angle approach 90 deg, the SNR will decrease. The hypernormalized parameter for  $\theta_1 = 75$  deg and  $\theta_2 = 75$  deg is

$$\Omega = 1.485 \times 10^{-12} \text{ radm}^2.$$

Single pixel SNR values from Figure 3.3 are  $SNR_{MAX} = 1.0 \times 10^4$  and  $SNR_{MIN} = 0.9 \times 10^4$ .

Varying range: As the range increases, the SNR will decrease. The hypernormalized parameter for  $r = 3000$  km is

$$\Omega = 1.576 \times 10^{-12} \text{ radm}^2.$$

Single pixel SNR values from Figure 3.3 are  $SNR_{MAX} = 1.0 \times 10^4$  and  $SNR_{MIN} = 0.9 \times 10^4$ .

Varying sensor collecting optic diameter: As the diameter decreases, the SNR will decrease. The hypernormalized parameter for  $D = .2m$  and  $r = 800 km$  is  $\Omega = 3.464 \times 10^{-13} radm^2$ , which is outside the bound of  $\Omega$ . For a shorter range,  $r = 440 km$ , the hypernormalized parameter is

$$\Omega = 1.385 \times 10^{-12} radm^2.$$

Single pixel SNR values from Figure 3.3 are  $SNR_{MAX} = 1.0 \times 10^4$  and  $SNR_{MIN} = 0.9 \times 10^4$ .

Each of the three different illustrations dropped the hypernormalized parameter to about the same value,  $\Omega \approx 1.5 \times 10^{-12}$ . The hypernormalized parameter was computed using the configuration code (Appendix A, page A-3), a quick calculation compared to the computationally intensive radiometry model. Without running the radiometry model again, the hypernormalized parameter modeled a variety of target-sensor encounters.

### 3.3.2 Case Two.

**3.3.2.1 Configuration.** The configuration for Case (2) is identical to Case (1).

**3.3.2.2 Spectral Reflectance.** The modeled rocket body is painted white, SMC-20, instead of having a bare aluminum surface (Figure F.2).

**3.3.2.3 Radiometry results.** Table 3.5, Summary of Results, Case(2), shows enough signal is present in each of the wavelength bandwidths to perform hyperspectral imaging. The count rate and SNR values in Table 3.5 correspond to the points where  $\Omega_{ref}$  intersects the plotted lines in Figures C.1-C.9, giving MIN

and MAX values as a function of mean wavelength. The  $SNR_{pix}$  values correspond to value  $z = 1$  ( $\theta_1 = \theta_2 = 0$  deg). The lowest count rate is  $1.3 \times 10^7$ , which is five orders of magnitude above the background count rate determined in Section 2.3. The lowest values of SNR and  $SNR_{pix}$  are well above the minimum threshold of three. Appendix C contains a complete set of graphs for Case (2), Figure C.1 to

CASE 2		Wavelength Bandwidth ( $\Delta \lambda$ )		
		20 nm	10 nm	5 nm
Count rate	MAX	$6.2 \times 10^8$	$3.1 \times 10^8$	$1.6 \times 10^8$
	MIN	$4.9 \times 10^8$	$2.5 \times 10^8$	$1.3 \times 10^8$
SNR	MAX	$7.0 \times 10^4$	$5.0 \times 10^4$	$3.5 \times 10^4$
	MIN	$6.2 \times 10^4$	$4.5 \times 10^4$	$3.2 \times 10^4$
$SNR_{pix}$	MAX	$1.2 \times 10^4$	$0.83 \times 10^4$	$0.58 \times 10^4$
	MIN	$0.58 \times 10^4$	$0.42 \times 10^4$	$0.30 \times 10^4$

Table 3.5 Summary of Results, Case (2)

Figure C.9. The set consists of a legend (Table C.1) converting  $i$  to  $\bar{\lambda}$  and graphs of count rate, SNR, and  $SNR_{pix}$  for each of the 20 nm, 10 nm and 5 nm wavelength bandwidths. The 10 nm and 5 nm curves are very similar due to the interpolation of the spectral reflectance values (compare Figure C.5 to Figure C.8). The line order for Case (2), Table 3.6, does not change for the three wavelength bandwidths. Two lines overlap for the 10 nm and 5 nm bandwidth, the 650 nm–550 nm pair. Possible reasons for the slight difference between the 20 nm and 10 nm plots are the wider wavelength interval and coarser spectral reflectance values from the interpolation of the spectral reflectance data file.

**3.3.2.4 Integration time.** The minimum integration times for each wavelength bandwidth for an  $SNR_{pix} = 3$  are given in Table 3.7. As the bandwidth decreases, the integration time increases. An integration time in microseconds is very small; however, encounter mechanics such as orbital velocity and target stability may necessitate a very small integration time.



ORDER	20 nm	10 nm	5 nm
Top 5	640	650	650
4	540	550	550
3	740	750	750
2	840	850	850
Bottom 1	440	450	450

Missing horizontal lines indicate overlapping wavelength intervals

Table 3.6 Line Order, Case (2)

$\Delta \lambda$	$t_d$
20 nm	9.6 $\mu$ sec
10 nm	17.7 $\mu$ sec
5 nm	35.4 $\mu$ sec

Table 3.7 Minimum integration time, Case (2)

*3.3.3 Comparison, Case One versus Case Two.* For this analysis, the three areas of comparison are the signal strength from the target, the line order, and line spacing. This comparison involves Case (1) and Case (2) single pixel SNR graphs with  $\Delta \lambda = 10$  nm. Legends for the Case (1) and Case (2) graphs are the same, and given in Table 3.1. Case (1) SNR 10 nm was used earlier in Section 3.2.3.8, (see Figure 3.3). The Case (2) counterpart, Case (2) SNR 10 nm is shown in Figure 3.5.

ORDER	20 nm		10 nm		5 nm	
	Case (1)	Case (2)	Case (1)	Case (2)	Case (1)	Case (2)
Top 5	640	640	650	650	650	650
4	540	540	550	550	550	550
3	740	740	750	750	750	750
2	840	840	850	850	850	850
Bottom 1	440	440	450	450	450	450

Missing horizontal lines indicate overlapping wavelength intervals

Table 3.8 Line Order, Case (1) and Case (2) Combined

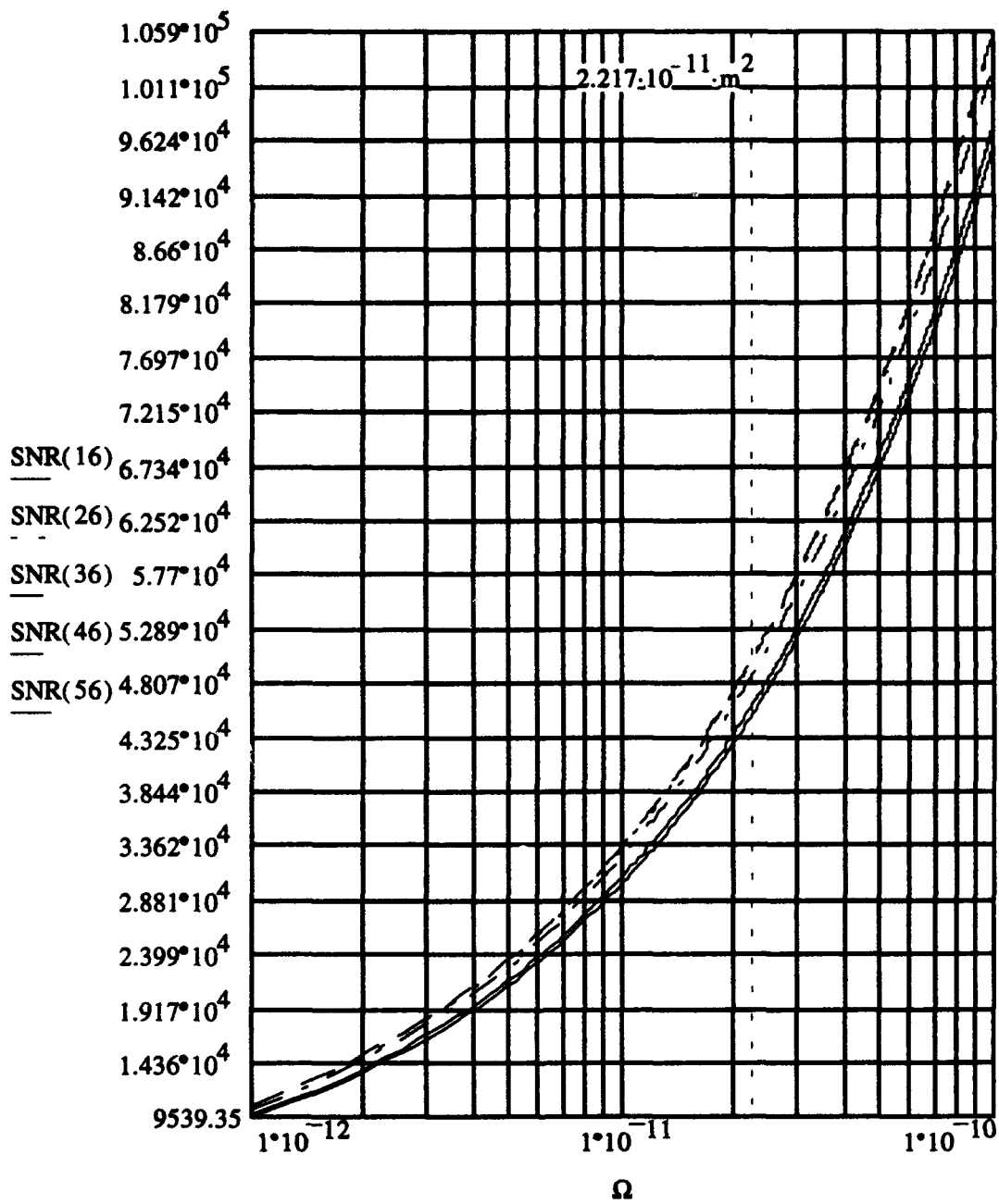


Figure 3.5 Case (2), SNR vs  $\Omega$  ( $\text{rad m}^2$ ), 10 nm

To aid the comparison, the line orders of Case (1) and Case (2) are combined in Table 3.8. The line spacing comparison is made using Table 3.8, Figure 3.3, and Figure 3.5.

<u>Area</u>	<u>Comparison</u>
Signal Strength	Case (2) has larger SNR values than Case (1).
Line Order	Line order is the same for the two cases.
Line Spacing	Line spacing is different for all bandwidths.

Space Object Identification information may be stored in the different target signal strengths in different spectral bands. The differences between Case (1) and Case (2) are from the different spectral reflectances of aluminum and white paint.

### 3.4 *Hyperspectrometry*

The two cases for hyperspectrometry involve geosynchronous communications satellites. The satellites are cylindrical with an antenna on top, but have different sizes (9). The results for each case are discussed individually, and then compared to each other.

#### 3.4.1 *Case Three.*

**3.4.1.1 Configuration.** Target: A cylindrical communications satellite is 7.6 m long and 3.64 m in diameter. The satellite has an antenna 2.4 m in diameter on top of the cylinder (1:12). The range to the target is 36,000 km, the altitude of a geosynchronous satellite.

Sensor: The sensor is a 1.6 m diameter telescope. Three regions of the electromagnetic spectrum are of interest: 300 nm–400 nm, Ultraviolet (UV); 380 nm–540 nm, Blue (B); and 480 nm–650 nm, Visible (V). Within each region, the mean wavelengths of interest are in increments of 20 nm. (9)

Imaging determination: The maximum target angular subtense is

$$\Delta\phi_{sat} = 2.778 \times 10^{-7} \text{ rad}$$

and the angular subtense of the diffraction limited spot is

$$\Delta\phi_{min} = 6.863 \times 10^{-7} \text{ rad}$$

$\Delta\phi_{min} > \Delta\phi_{sat}$ , so imaging is not possible.

Hypernormalized parameter: The reference hypernormalized parameter for normal incidence ( $\theta_1 = \theta_2 = 0$  deg) is

$$\Omega_{ref} = 2.936 \times 10^{-14} \text{ rad m}^2.$$

The range of the hypernormalized parameter in the radiometry model is

$$\Omega = 10^{-15} \dots 10^{-13} \text{ rad m}^2.$$

*3.4.1.2 Spectral Reflectance.* The satellite was modelled with three materials: solar cells, SMC-23 (Figure F.4); a mirrored thermal control band (assumed to be silver), SMC-18 (Figure F.3); and aluminized mylar, SMC-30 (Figure F.5). The thermal control band is approximately 1/7 the length of the cylinder. The fractional material areas are 73.7 percent solar cells, 12.3 percent silver, and 14.0 percent aluminized mylar, and yield a count rate expression of

$$i_{T(total)} = .737i_{T(23)} + .123i_{T(18)} + .140i_{T(30)}.$$

*3.4.1.3 Radiometry results.* Table 3.9, Summary of Results, Case(3), shows enough signal is present in each of the wavelength bandwidths to perform hyperspectrometry. The count rate and SNR values in Table 3.9 correspond to the points where  $\Omega_{ref}$  intersects the plotted lines in Figures D.1-D.18, giving MIN and

MAX values as a function of mean wavelength. The lowest count rate is  $1.9 \times 10^4$ , which is an order of magnitude above the background count rate determined in Section 2.3. The lowest value of the SNR is well above the minimum threshold of three.

CASE 3			Wavelength Bandwidth ( $\Delta \lambda$ )		
			20 nm	10 nm	5 nm
Count rate	UV	MAX	$2.5 \times 10^5$	$1.3 \times 10^5$	$6.4 \times 10^4$
		MIN	$7.5 \times 10^4$	$3.7 \times 10^4$	$1.9 \times 10^4$
	B	MAX	$2.7 \times 10^5$	$1.4 \times 10^5$	$5.4 \times 10^4$
		MIN	$7.8 \times 10^4$	$8.5 \times 10^4$	$3.2 \times 10^4$
	V	MAX	$2.9 \times 10^5$	$1.5 \times 10^5$	$7.0 \times 10^4$
		MIN	$1.1 \times 10^5$	$9.5 \times 10^4$	$4.9 \times 10^4$
SNR	UV	MAX	$1.4 \times 10^3$	$0.99 \times 10^3$	$0.73 \times 10^3$
		MIN	$0.75 \times 10^3$	$0.54 \times 10^3$	$0.38 \times 10^3$
	B	MAX	$1.5 \times 10^3$	$1.0 \times 10^3$	$0.71 \times 10^3$
		MIN	$1.1 \times 10^3$	$0.83 \times 10^3$	$0.58 \times 10^3$
	V	MAX	$1.5 \times 10^3$	$1.0 \times 10^3$	$0.75 \times 10^3$
		MIN	$1.2 \times 10^3$	$0.88 \times 10^3$	$0.62 \times 10^3$

Table 3.9 Summary of Results, Case (3)

Appendix D contains a complete set of graphs for Case (3), Figure D.1 to Figure D.18. The set consists of a legend (Table D.1) converting  $i$  to  $\bar{\lambda}$  and graphs of count rate and SNR for each of the 20 nm, 10 nm and 5 nm wavelength bandwidths. The 10 nm and 5 nm curves are very similar due to the interpolation of the spectral reflectance values (compare Figure D.10 to Figure D.16). The line order for Case (3) is separated into Ultraviolet (UV), Blue (B) and Visible(V) regions.

Table 3.10 shows the line order for the UV region. The 20 nm bandwidth has a different order than the 10 nm and 5 nm. Possible reasons for this difference are the wider wavelength interval and coarser spectral reflectance values from the interpolation of the spectral reflectance data file. Two lines overlap for the 10 nm and 5 nm bandwidth, the 380 nm-360 nm pair.

ULTRAVIOLET (UV)			
ORDER	20 nm	10 nm	5 nm
Top 6	360	380	380
5	380	360	360
4	340	400	400
3	400	340	340
2	320	320	320
Bottom 1	300	300	300

Missing horizontal lines indicate overlapping wavelength intervals

Table 3.10 Line Order, Case (3), UV

BLUE (B)			
ORDER	20 nm	10 nm	5 nm
Top 9	540	540	540
8	520	380	380
7	380	520	520
6	500	400	400
5	480	500	500
4	400	480	480
3	460	420	420
2	420	460	460
Bottom 1	440	440	440

Missing horizontal lines indicate overlapping wavelength intervals

Table 3.11 Line Order, Case (3), B

Table 3.11 shows the line order for the B region. The 20 nm bandwidth has a different order than the 10 nm and 5 nm. Possible reasons for this difference are the wider wavelength interval and coarser spectral reflectance values from the interpolation of the spectral reflectance data file. Two line pairs overlap: the 380 nm–540 nm pair for the 10 nm and 5 nm bandwidths, and the 380 nm–500 nm pair for the 20 nm bandwidth.

VISIBLE (V)			
ORDER	20 nm	10 nm	5 nm
Top 9	640	640	640
8	620	620	620
7	600	600	600
6	580	580	580
5	560	560	560
4	540	540	540
3	520	520	520
2	500	500	500
Bottom 1	480	480	480

Missing horizontal lines indicate overlapping wavelength intervals

Table 3.12 Line Order, Case (3), V

Table 3.12 shows the line order for the V region. The line order is the same for all three bandwidths. Three lines overlap, those for 600 nm, 620 nm, and 640 nm.

*3.4.1.4 Integration time.* Since imaging is not possible, Equation 3.1 was used to calculate the minimum integration time. The minimum integration times for an  $SNR = 3$  for each wavelength bandwidth are given in Table 3.13. As the bandwidth decreases, the integration time increases.

### *3.4.2 Case Four.*

*3.4.2.1 Configuration.* Target: A cylindrical communications satellite is 4.77 m long and 2.2 m in diameter. The satellite has an antenna 1.83 m in

$\Delta \lambda$	$t_d$
20 nm	125 $\mu\text{sec}$
10 nm	248 $\mu\text{sec}$
5 nm	496 $\mu\text{sec}$

Table 3.13 Minimum integration time, Case (3)

diameter on top of the cylinder (1:12). The range to the target is 36,000 km, the altitude of a geosynchronous satellite. Sensor: The sensor is a 1.6 m diameter telescope. Three regions of the electromagnetic spectrum are of interest: 300 nm–400 nm, Ultraviolet (UV); 380 nm–540 nm, Blue (B); and 480 nm–650 nm, Visible (V). Within each region, the mean wavelengths of interest are in increments of 20 nm (9).

Imaging determination: The maximum target angular subtense is

$$\Delta\phi_{sat} = 1.833 \times 10^{-7} \text{ rad}$$

and the angular subtense of the diffraction limited spot is

$$\Delta\phi_{min} = 6.863 \times 10^{-7} \text{ rad}$$

$\Delta\phi_{min} > \Delta\phi_{sat}$ , so imaging is not possible.

Hypernormalized parameter: The reference hypernormalized parameter for normal incidence ( $\theta_1 = \theta_2 = 0 \text{ deg}$ ) is

$$\Omega_{ref} = 1.197 \times 10^{-14} \text{ rad m}^2$$

The range of the hypernormalized parameter in the radiometry model is

$$\Omega = 10^{-15} \dots 10^{-13} \text{ rad m}^2.$$

**3.4.2.2 Spectral Reflectance.** The satellite was modelled with three materials: solar cells, SMC-23 (Figure F.4); a mirrored thermal control band (as-



sumed to be silver), SMC-18 (Figure F.3); and aluminized mylar, SMC-30 (Figure F.5). The thermal control band is approximately 1/7 the length of the cylinder. The fractional material areas are 68.7 percent solar cells, 11.5 percent silver, and 19.8 percent aluminized mylar, and yield a count rate expression of

$$i_{T(total)} = .687i_{T(23)} + .115i_{T(18)} + .198i_{T(30)}$$

3.4.2.3 Radiometry results. Table 3.14, Summary of Results, Case(4), shows enough signal is present in each of the wavelength bandwidths to perform hyperspectrometry. The count rate and SNR values in Table 3.9 correspond to the points where  $\Omega_{ref}$  intersects the plotted lines in Figures D.1-D.18, giving MIN and MAX values as a function of mean wavelength. The lowest count rate is  $8.0 \times 10^3$ , which is roughly an order of magnitude above the background count rate determined in Section 2.3. The lowest value of the SNR is well above the minimum threshold of three.

CASE 4			Wavelength Bandwidth ( $\Delta \lambda$ )		
			20 nm	10 nm	5 nm
Count rate	UV	MAX	$1.0 \times 10^5$	$5.5 \times 10^4$	$2.8 \times 10^4$
		MIN	$3.2 \times 10^4$	$1.7 \times 10^4$	$8.0 \times 10^3$
	B	MAX	$1.3 \times 10^5$	$6.0 \times 10^4$	$3.0 \times 10^4$
		MIN	$7.9 \times 10^4$	$4.0 \times 10^4$	$2.0 \times 10^4$
	V	MAX	$1.4 \times 10^5$	$6.7 \times 10^4$	$3.2 \times 10^4$
		MIN	$9.5 \times 10^4$	$4.7 \times 10^4$	$2.4 \times 10^4$
SNR	UV	MAX	$0.89 \times 10^3$	$0.66 \times 10^3$	$0.47 \times 10^3$
		MIN	$0.52 \times 10^3$	$0.36 \times 10^3$	$0.26 \times 10^3$
	B	MAX	$0.90 \times 10^3$	$0.69 \times 10^3$	$0.49 \times 10^3$
		MIN	$0.76 \times 10^3$	$0.56 \times 10^3$	$0.41 \times 10^3$
	V	MAX	$1.0 \times 10^4$	$0.72 \times 10^3$	$0.51 \times 10^3$
		MIN	$0.85 \times 10^3$	$0.60 \times 10^3$	$0.43 \times 10^3$

Table 3.14 Summary of Results, Case (4)

Appendix E contains a complete set of graphs for Case (4), Figure D.1 to Figure D.18. The set consists of a legend (Table E.1) converting  $i$  to  $\bar{\lambda}$  and graphs of count rate and SNR for each of the 20 nm, 10 nm, and 5 nm wavelength bandwidths. The 10 nm and 5 nm curves are very similar due to the interpolation of the spectral reflectance values (compare Figure E.10 to Figure E.16). The line order for Case (4) is separated into Ultraviolet (UV), Blue (B) and Visible(V) regions.

ULTRAVIOLET (UV)			
ORDER	20 nm	10 nm	5 nm
TOP 6	360	380	380
5	380	360	360
4	400	400	400
3	340	340	340
2	320	320	320
BOTTOM 1	300	300	300

Missing horizontal lines indicate overlapping wavelength intervals

Table 3.15 Line Order, Case (4), UV

Table 3.15 shows the line order for the UV region. The 20 nm bandwidth has a different order than the 10 nm and 5 nm. Possible reasons for this difference are the wider wavelength interval and coarser spectral reflectance values from the interpolation of the spectral reflectance data file. One line pair overlaps for the 20 nm bandwidth, the 400 nm-340 nm pair.

Table 3.16 shows the line order for the B region. The 20 nm bandwidth has a different order than the 10 nm and 5 nm. Possible reasons for this difference are the wider wavelength interval and coarser spectral reflectance values from the interpolation of the spectral reflectance data file. Two line pairs overlap for the 20 nm bandwidth, the 440 nm-420 nm pair and the 400 nm-460 nm pair. One line pair overlaps for the 10 nm and 5 nm bandwidths, the 460 nm-420 nm pair.

Table 3.17 shows the line order for the V region. The line order is the same for all three bandwidths. Three lines overlap, the 600 nm-620 nm-640 nm.

BLUE (B)			
ORDER	20 nm	10 nm	5 nm
Top 9	540	540	540
8	520	520	520
7	500	380	380
6	380	500	500
5	480	400	400
4	400	480	480
3	460	460	460
2	420	420	420
Bottom 1	440	440	440

Missing horizontal lines indicate overlapping wavelength intervals

Table 3.16 Line Order, Case (4), B

VISIBLE (V)			
ORDER	20 nm	10 nm	5 nm
Top 9	640	640	640
8	620	620	620
7	600	600	600
6	580	580	580
5	560	560	560
4	540	540	540
3	520	520	520
2	500	500	500
Bottom 1	480	480	480

Missing horizontal lines indicate overlapping wavelength intervals

Table 3.17 Line Order, Case (4), V

3.4.2.4 *Integration time.* The minimum integration times for an  $SNR = 3$  for each wavelength bandwidth are given in Table 3.18. As the bandwidth decreases, the integration time increases.

$\Delta \lambda$	$t_d$
20 nm	278 $\mu\text{sec}$
10 nm	553 $\mu\text{sec}$
5 nm	1000 $\mu\text{sec}$

Table 3.18 Minimum integration time, Case (4)

3.4.3 *Comparison, Case Three versus Case Four.* The three areas of comparison are the signal strength from the target, the line order, and line spacing. This comparison involves Case (3) and Case (4) single pixel SNR graphs with  $\Delta\lambda = 10$  nm. Legends for the Case (3) and Case (4) graphs are the same, and given in Table 3.19. Comparisons for Case (3) and Case (4) are broken into Ultraviolet, Blue, and Visible categories. To aid the comparison, the line orders from Case (3) and Case (4) are combined within each region. The line order tables contain all three wavelength bandwidths.

UV		B		V	
$i$	$\lambda$ (nm)	$i$	$\lambda$ (nm)	$i$	$\lambda$ (nm)
1	300	9	380	19	480
3	320	11	400	21	500
5	340	13	420	23	520
7	360	15	440	25	540
9	380	17	460	27	560
11	400	19	480	29	580
		21	500	31	600
		23	520	33	620
		25	540	35	640

Table 3.19 Legend, Case (3) and Case (4), 10 nm SNR graphs

3.4.3.1 *Ultraviolet comparison.* Figure 3.6 (Case (3), SNR (UV), 10 nm) and Figure 3.7 (Case (4), SNR (UV), 10 nm) show the two graphs compared in this section. Table 3.20 shows the combined line orders for Case (3) and Case (4), UV region. The line spacing comparison is made using Table 3.20, Figure 3.6, and Figure 3.7.

ULTRAVIOLET (UV)						
ORDER	20 nm		10 nm		5 nm	
	Case (3)	Case (4)	Case (3)	Case (4)	Case (3)	Case (4)
Top 6	360	360	380	380	380	380
5	380	380	360	360	360	360
4	340	400	400	400	400	400
3	400	340	340	340	340	340
2	320	320	320	320	320	320
Bottom 1	300	300	300	300	300	300

Missing horizontal lines indicate overlapping wavelength intervals

Table 3.20 Line Order, Case (3) and Case (4) Combined, UV

<u>Area</u>	<u>Comparison</u>
Signal Strength	Case (3) has larger SNR values than Case (4).
Line Order	Line order is nearly the same for the two cases.
Line Spacing	Line spacing is slightly different.

The main difference between Case (3) and Case (4) in the Ultraviolet region is in signal strength. Line order is the same for the 10 nm and 5 nm cases. The 20 nm graphs show slight differences in line order. These differences may be caused by the increased bandwidth and increased coarseness of the spectral reflectance. The line spacing between the two cases is only slightly different, with Case(4) having a number of lines that overlap. The Space Object Identification information for Case (3) and Case (4) UV lies primarily in the signal strength.

3.4.3.2 *Blue comparison.* Figure 3.8 (Case (3), SNR (B) 10 nm) and Figure 3.9 (Case (4), SNR (B), 10 nm) show the two graphs compared in this section.

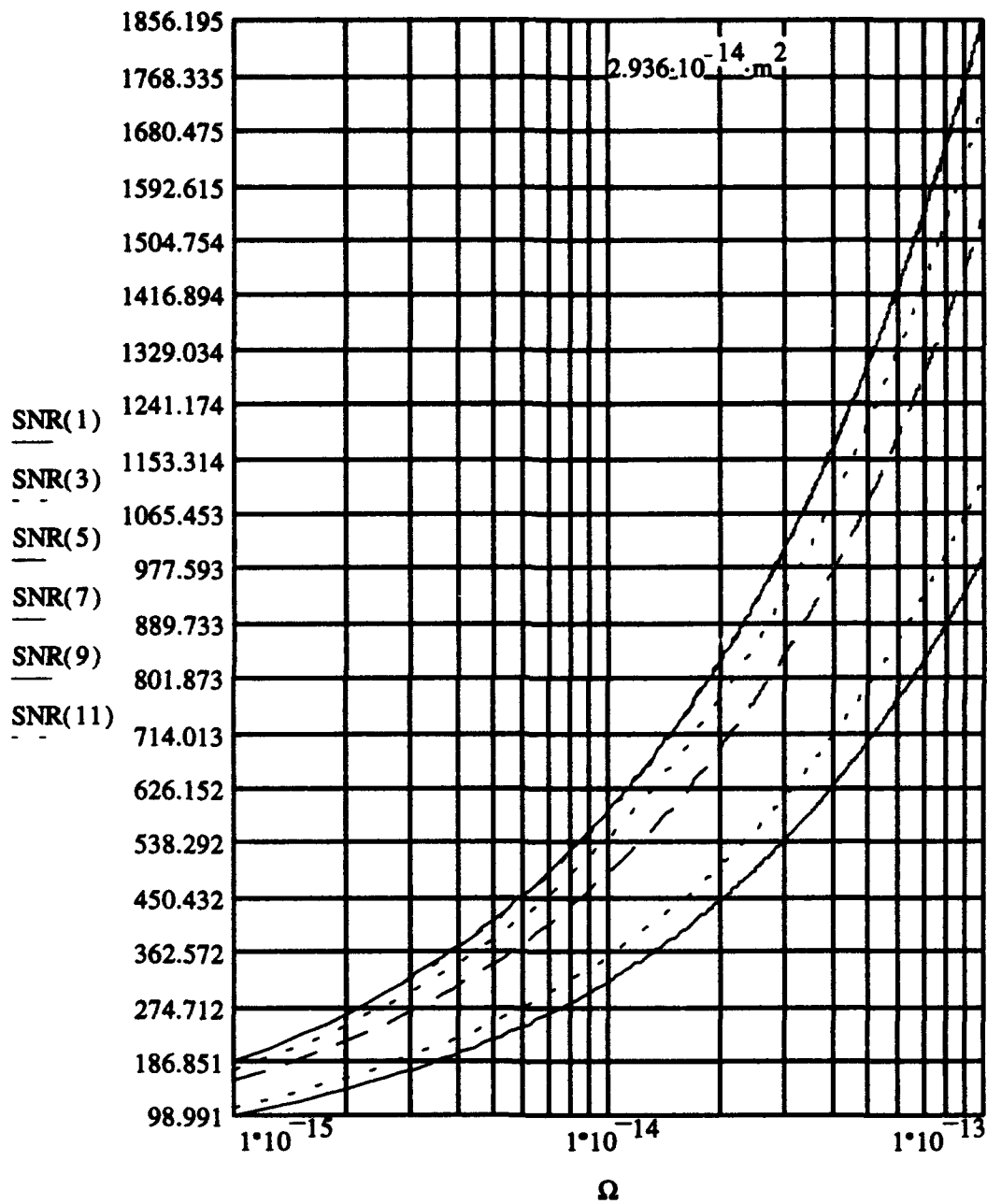


Figure 3.6 Case (3), SNR vs  $\Omega$  ( $\text{rad m}^2$ ) (UV), 10 nm

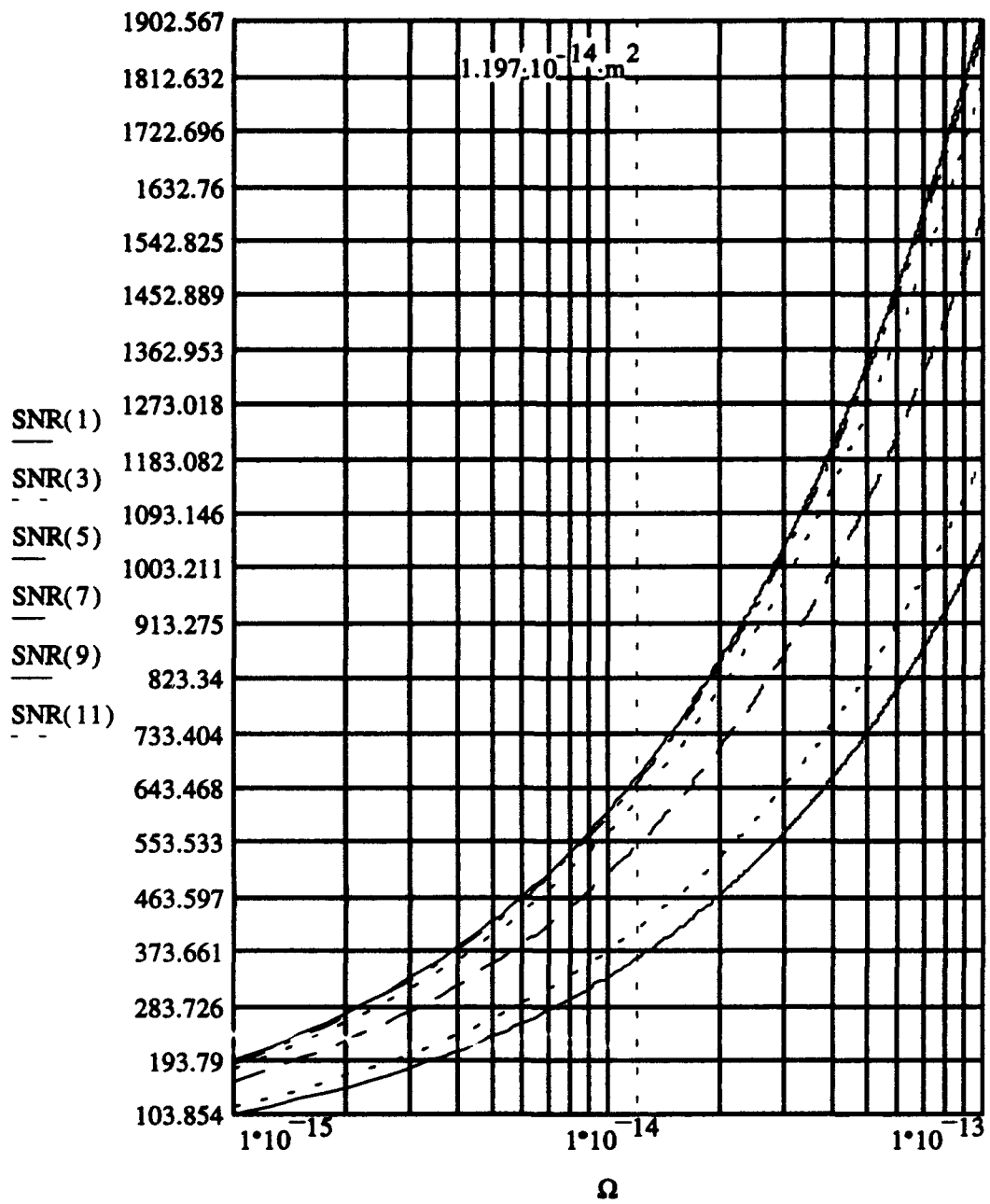


Figure 3.7 Case (4), SNR vs  $\Omega$  (rad m<sup>2</sup>) (UV), 10 nm

Table 3.21 shows the combined line orders for Case (3) and Case (4) Blue region. The line spacing comparison is made using Table 3.21, Figure 3.8, and Figure 3.9.

BLUE (B)						
ORDER	20 nm		10 nm		5 nm	
	Case(3)	Case(4)	Case(3)	Case(4)	Case(3)	Case(4)
Top 9	540	540	540	540	540	540
8	520	520	380	520	380	520
7	380	500	520	380	520	380
6	500	380	400	500	400	500
5	480	480	500	400	500	400
4	400	400	480	480	480	480
3	460	460	420	460	420	460
2	420	420	460	420	460	420
Bottom 1	440	440	440	440	440	440

Missing horizontal lines indicate overlapping wavelength intervals

Table 3.21 Line Order, Case (3) and Case (4) Combined, B

<u>Area</u>	<u>Comparison</u>
Signal Strength	Case (3) has larger SNR values than Case (4).
Line Order	Line order is different.
Line Spacing	Line spacing is different.

Differences exist in signal strength, line order, and line spacing between Case (3) and Case (4) in the B region. These differences apply to all wavelength bandwidths. Space Object Identification information may be stored in the different target signal strengths in different spectral bands. The differences between Case (3) and Case (4) are from the different sizes and fractional material areas.

*3.4.3.3 Visible comparison.* Figure 3.10 (Case (3), SNR (V) 10 nm) and Figure 3.11 (Case (4), SNR (V), 10 nm) show the two graphs compared in this section. Table 3.22 shows the combined line orders for Case (3) and Case (4), Visible region. The line spacing comparison is made using Table 3.22, Figure 3.10, and Figure 3.11.



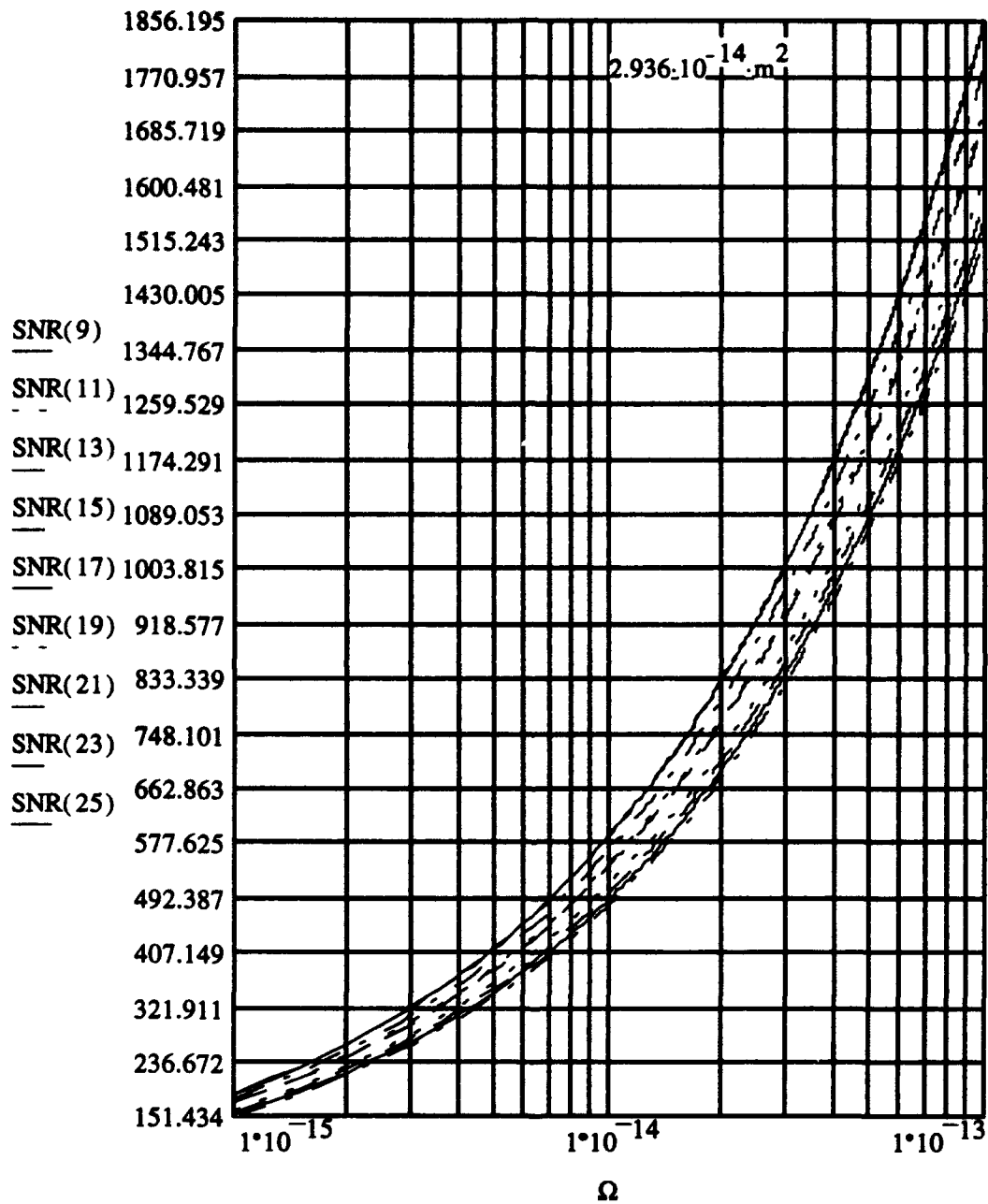


Figure 3.8 Case (3), SNR vs  $\Omega$  ( $\text{rad m}^2$ ) (B), 10 nm

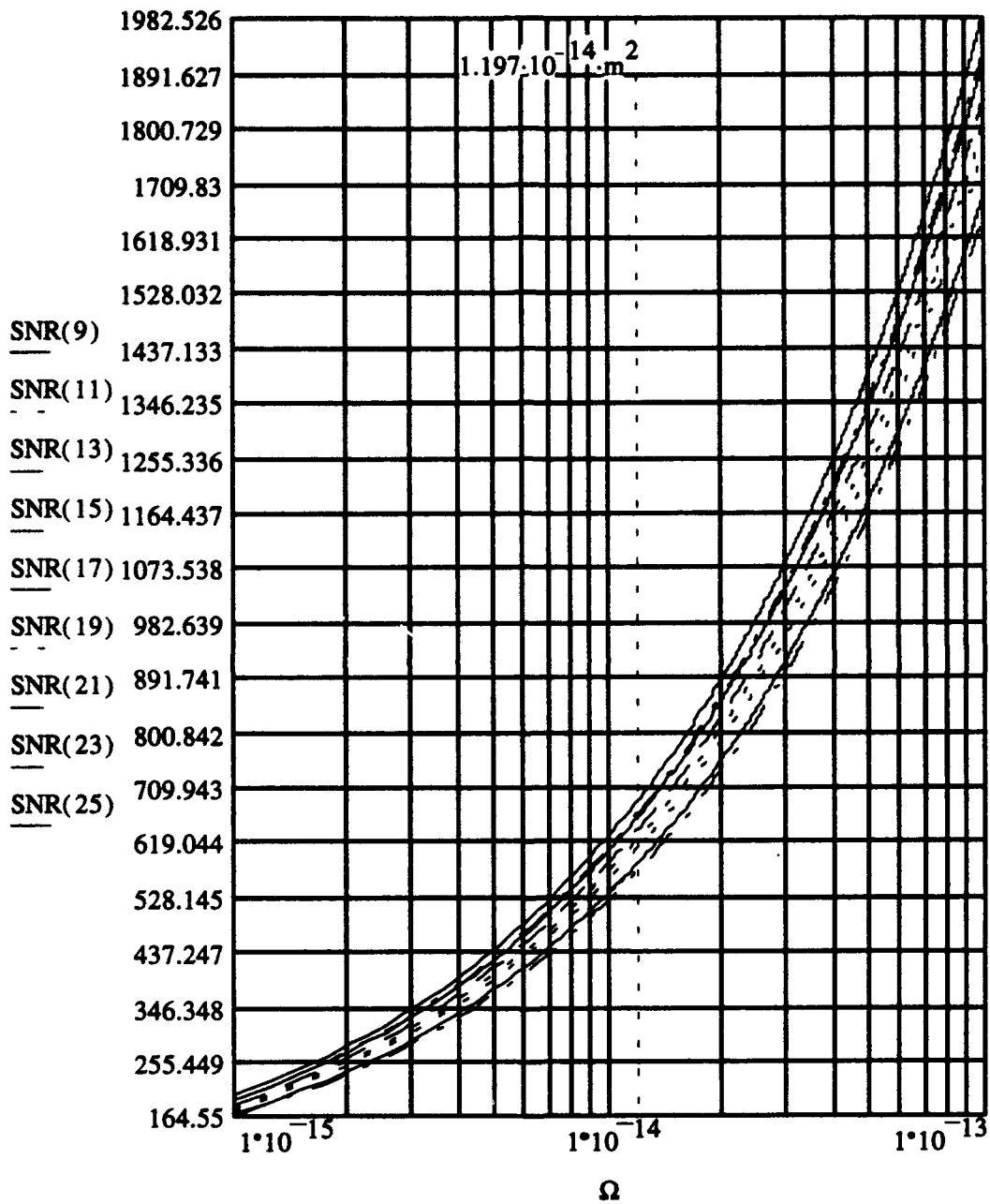


Figure 3.9 Case (4), SNR vs  $\Omega$  ( $\text{rad m}^2$ ) (B), 10 nm

VISIBLE (V)						
ORDER	20 nm		10 nm		5 nm	
	Case(3)	Case(4)	Case(3)	Case(4)	Case(3)	Case(4)
Top 9	640	640	640	640	640	640
8	620	620	620	620	620	620
7	600	600	600	600	600	600
6	580	580	580	580	580	580
5	560	560	560	560	560	560
4	540	540	540	540	540	540
3	520	520	520	520	520	520
2	500	500	500	500	500	500
Bottom 1	480	480	480	480	480	480

Missing horizontal lines indicate overlapping wavelength intervals

Table 3.22 Line Order, Case (3) and Case (4) Combined, V

<u>Area</u>	<u>Comparison</u>
Signal Strength	Case (3) has larger SNR values than Case (4).
Line Order	Line order is exactly the same for the two cases.
Line Spacing	Line spacing is slightly different.

The main difference between Case (3) and Case (4) in the UV region is in signal strength. The line spacing between the two cases is only slightly different, with Case(4) having lines grouped closer together. The Space Object Identification information for Case (3) and Case (4) Visible region lies primarily in the signal strength.

The blue region offers the most promise for discriminating between the two targets. The increased areas of the solar array, silver thermal band, and antenna probably caused the shift of the 380 nm and 520 nm lines. The 380 nm region marks a high rate of change for the spectral reflectance of the three materials (see Figures F.2, F.4, and F.5). For SOI analysis, looking for these regions of dramatic change in spectral reflectance would yield the most hyperspectral information.

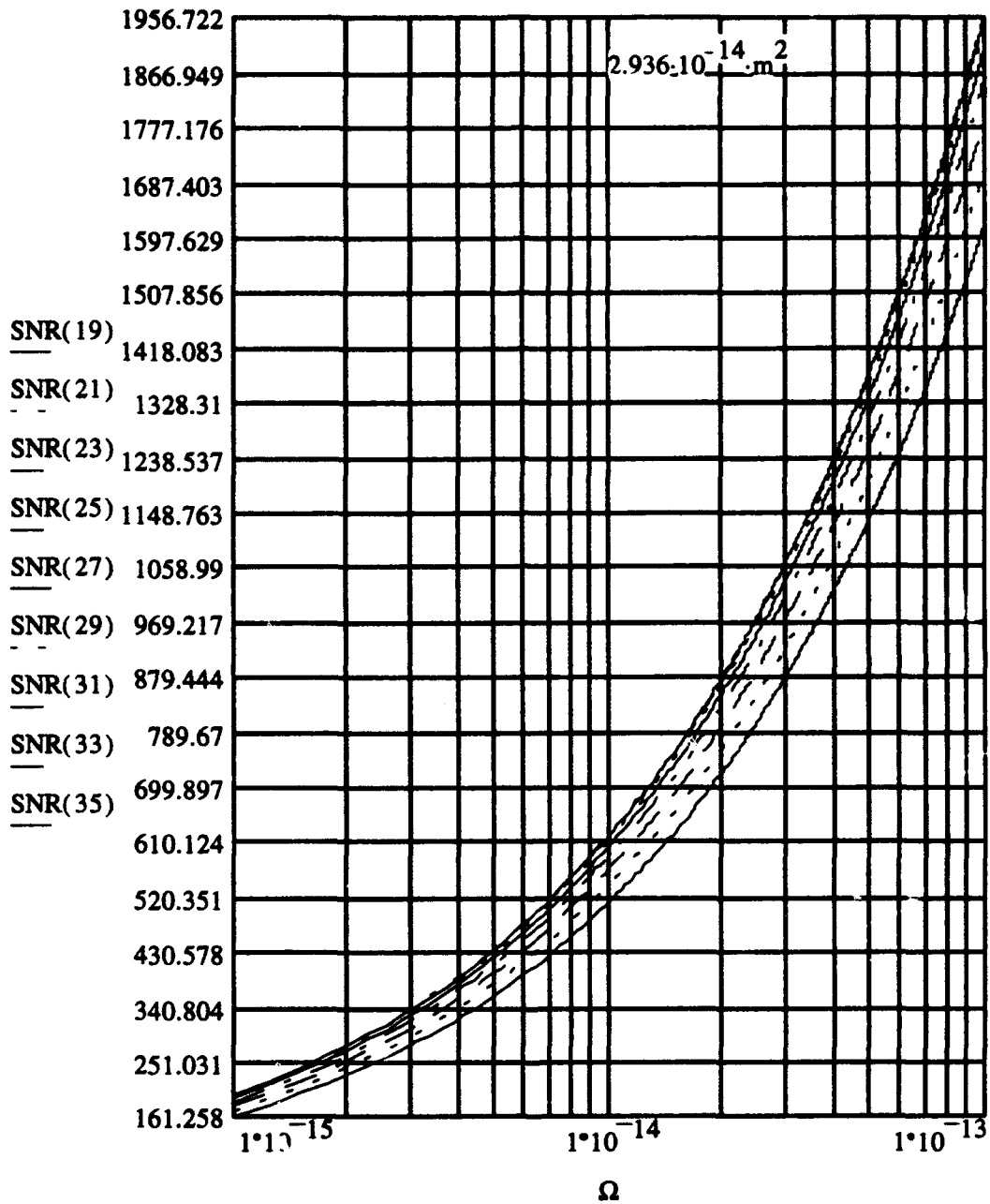


Figure 3.10 Case (3), SNR vs  $\Omega$  ( $rad m^2$ ) (V), 10 nm

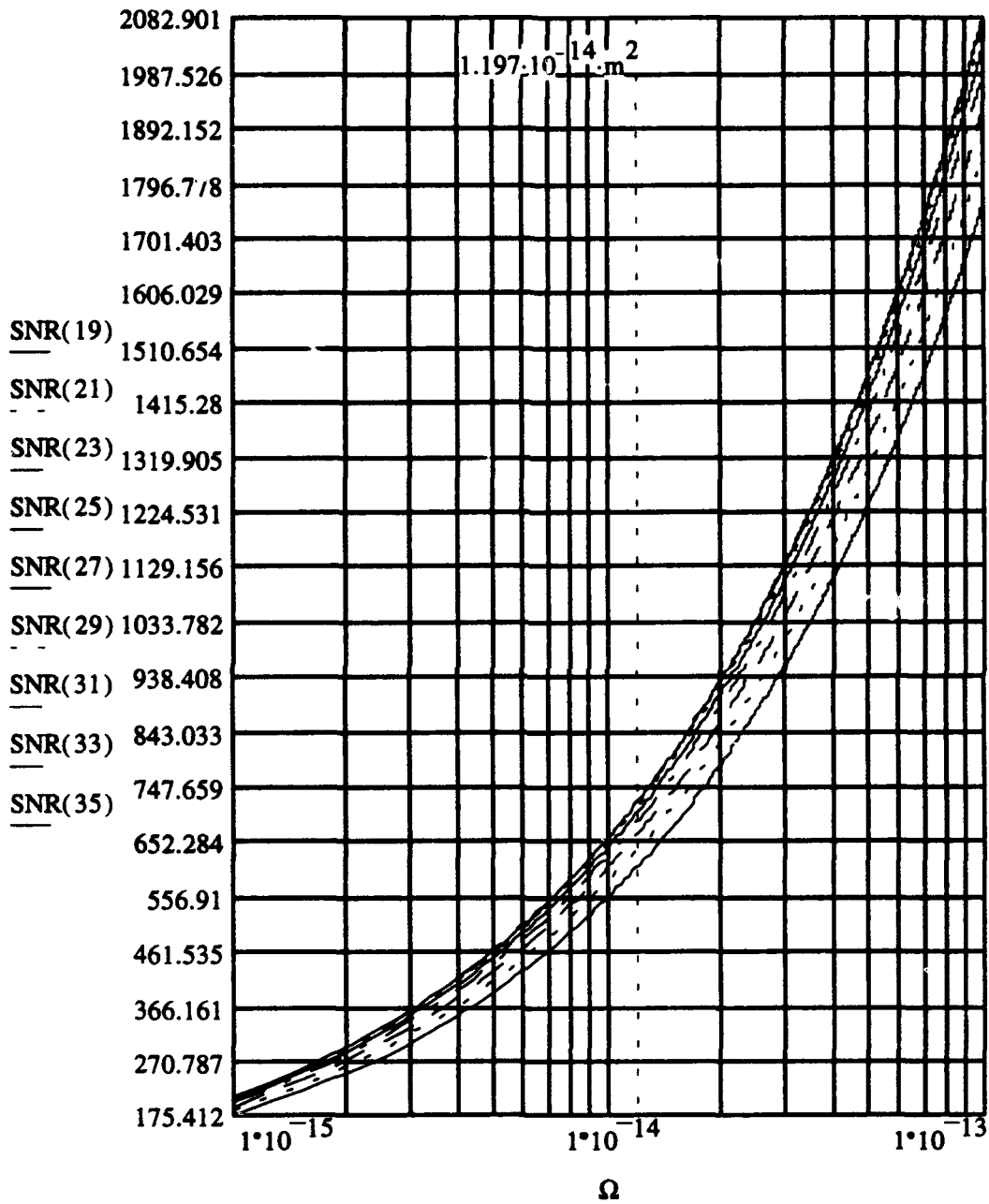


Figure 3.11 Case (4), SNR vs  $\Omega$  ( $rad m^2$ ) (V), 10 nm

All four cases had enough signal present for hyperspectral analysis in the three wavelength bandwidths tested. Differences between the cases exist in signal strength, line order, and line spacing. The signal strength, line order, and line spacing depend on the wavelength and wavelength bandwidth for a target. Differences in these areas indicate Space Object Identification information may be stored in the different target signal strengths in different spectral bands, and may serve as the foundation for SOI applications. The differences existed for all three of the wavelength bandwidths tested. The 20 nm bandwidth was consistently different from the 10 nm and 5 nm plots. Even so, the 20 nm bandwidth revealed differences between the case studies. For narrow wavelength bandwidths, lines for adjacent regions often overlapped.

## IV. Conclusions and Recommendations

### 4.1 Conclusions

Hyperspectral analysis is being proposed as a means of enhancing Space Object Identification capability. This study developed a mathematical simulation based on fundamental radiometry principles to evaluate the feasibility of hyperspectral analysis from a Signal to Noise perspective. For the SNR evaluation, the target signal, background and detector noise, and integration time had to be characterized. The target signal was characterized by the photon flux, spectral reflectivity, and a hypernormalized parameter that grouped all remaining variables into a single variable. The background noise was assumed small in comparison to the target signal, and detector noise was modeled from a CCD detector. The integration time was bounded using a best and worst case. The best case was applied to the radiometry model. The worst case was determined by selecting a minimum SNR threshold and solving for the integration time. Using these parameters, the single pixel SNR equation for hyperspectrometry and  $SNR_{pix}$  equation for hyperspectral imaging were developed. The count rate from the detector, the single pixel SNR, and  $SNR_{pix}$  are outputs of the radiometry model. The radiometry model was used for four case studies. Two cases involved hyperspectral imaging and two involved hyperspectrometry. The procedure for running a case study involved specifying a configuration, interpolating the spectral reflectances, and running the radiometry model. For the hyperspectral imaging case studies, the modeled target was a rocket body, made of aluminum in Case (1), and painted white in Case (2). For the hyperspectrometry case studies Case (3) and Case (4), the targets were two communication satellites, having the same shape but different sizes and fractional material areas. The case studies revealed the following main conclusions:

1. Enough signal is present for hyperspectral imaging and hyperspectrometry for wavelength bandwidths of  $\Delta \lambda = 20$  nm, 10 nm, and 5 nm.

2. The results for Case (1) and Case (2), and for Case (3) and Case (4), show differences in signal level as a function of wavelength and bandwidth which may serve as a basis for Space Object Identification. For Case (1) and Case (2), differences can be attributed to the different spectral reflectances between an aluminum and white object. For Case (3) and Case (4), the difference can be attributed to the different sizes and fractional material areas.

These conclusions prove the feasibility of hyperspectral measurements of space objects. A number of corollary issues regarding hyperspectral analysis were observed in the course of this analysis:

1. Two or more lines often overlapped in the count rate and SNR graphs. For the visible region in Case (3) and Case (4), three wavelength intervals (600 nm, 620 nm, and 640 nm) always overlapped. This problem is compounded when two regions are adjacent, especially at  $\Delta\lambda = 5$  nm.
2. All the wavelength bandwidths showed differences between the targets. If a bandwidth of  $\Delta\lambda = 20$  nm reveals significant SOI characteristics, making the wavelength bandwidth more narrow is not necessary. For data loading considerations, a  $\Delta\lambda = 5$  nm requires at least four times the data processing capability as a  $\Delta\lambda = 20$  nm.

#### 4.2 *Recommendations for Further Research*

This study demonstrated enough target signal is present to perform hyperspectral analysis. The following areas of research are offered as possibilities for further investigation:

1. Given a count rate from a detector, can the target's material composition be determined?
2. Develop a hyperspectral imaging simulation that links a target's spectral reflectance to spatial coordinates.



3. For a ground based sensor, investigate atmospheric effects on hyperspectral analysis.
4. What is the maximum wavelength bandwidth that would provide SOI information, and keep the data load at a minimum? Are there regions of the electromagnetic spectrum that reveal more SOI information than others? For example, in Case (3) and Case (4), the blue region revealed the greatest differences between the two targets.

In summary, enough signal is present for hyperspectral analysis of space objects. The case studies in this analysis show differences exist between targets which might be exploited for SOI purposes. Hyperspectral analysis warrants further investigation.

## Appendix A. Mathcad Models

### A.1 Model Configuration

Before running a case study, two things must be determined: the ability of the sensor to image the target and the reference hypernormalized parameter. The Mathcad configuration model (page A-3) calculates the target angular subtense and angular subtense of the diffraction limited spot. When  $\Delta\phi_{min} < \Delta\phi_{sat}$ , the sensor can image the target. Using the target and sensor parameters, the hypernormalized parameter  $\Omega$  is calculated for normal incidence. This value becomes the hypernormalized reference parameter,  $\Omega_{ref}$ .

### A.2 Spectral Reflectivity Interpolation

The spectral reflectances for a material are compiled in the *Matter.dat Surface Properties Data Compilation* (14). This compilation assigns a Surface Material Code (SMC) to a material and gives the spectral reflectances versus wavelength in increments of 10 nm. The Mathcad interpolation code (pages A-4 and A-6) generates spectral reflectances at 20 nm and 5 nm bandwidths. The code also produces plots of the spectral reflectances for each bandwidth to verify the interpolated values give a spectral reflectance curve close to the original spectral reflectance curve in the *Matter.dat Surface Properties Data Compilation*.

### A.3 Radiometry Model

The Mathcad radiometry code (page A-7) generates the count rate, SNR, and  $SNR_{pix}$  plots. The model requires the maximum and minimum wavelengths and wavelength bandwidth ( $\Delta\lambda$ ) to calculate the photon flux  $P$  using Planck's formula and the inverse square law. A counter ( $i$ ) is used as a reference pointer throughout the radiometry model, and corresponds to a wavelength interval. The last page of this appendix (page A-8) contains a counter to wavelength conversion for 20 nm, 10 nm

and 5 nm wavelength bandwidths. For example, if  $\Delta \lambda = 10$  nm, an  $i = 23$  is a 10 nm bandwidth centered on 520 nm. Spectral relectance data files are specific to material and wavelength. The data file associated with  $\rho_{02}$  for a 20 nm  $\Delta \lambda$  is smc02xx.dat, xx for 20 nm (x for 10 nm, and v for 5 nm). The hypernormalized parameter is varied by an order of magnitude above and below the reference hypernormalized parameter's exponent. The remaining input parameters are the integration time  $t_d$ , and the detector read noise  $\sigma_{rn}$ . Mathcad calculates the count rate, the overall SNR and the  $SNR_{pix}$  (if applicable), and outputs the results to graphs.

### Configuration

Target: Rocket body, 6 m long, 2 m in diameter. Range 800 km.

Case 1 Al and case 2 white paint.

Sensor: Diameter primary mirror = 1.6 m.

#### Target parameters:

$L_T := 6\text{-m}$  Length

$r := 800\text{-km}$  Range

$$\Delta\phi_{\text{sat}} := \frac{L_T}{r}$$

$$\Delta\phi_{\text{sat}} = 7.5 \cdot 10^{-6}$$

#### Sensor Parameters

$\lambda_{\text{max}} := 900\text{-nm}$  Max wavelength

$D := 1.6\text{-m}$  Sensor optic diameter

$$\Delta\phi_{\text{min}} := 1.22 \cdot \frac{\lambda_{\text{max}}}{D}$$

$$\Delta\phi_{\text{min}} = 6.863 \cdot 10^{-7}$$

$\Delta\phi_{\text{min}} < \Delta\phi_{\text{sat}}$  Can image target

Compute hypernormalized parameter that corresponds to above object:

#### Hypernormalized parameter

$$S_R := \pi \cdot \left(\frac{D}{2}\right)^2 \quad \text{Area of sensor optic}$$

$r = 800\text{-km}$  Range to target

$\theta_1 := 0$  Bound hypernormalized parameter at normal incidence

$\theta_2 := 0$

$\tau_o := .98$  Optical transmission

$S_T := 12\text{-m}^2$  Area of target

$\eta := .6$  Average quantum efficiency of detector

$$\Omega_{\text{ref}} := \frac{S_R}{r^2} \cdot \cos(\theta_1) \cdot \cos(\theta_2) \cdot \tau_o \cdot S_T \cdot \eta$$

$$\Omega_{\text{ref}} = 2.217 \cdot 10^{-11} \cdot \text{m}^2 \quad \text{Reference hypernormalized parameter}$$

## Interpolation

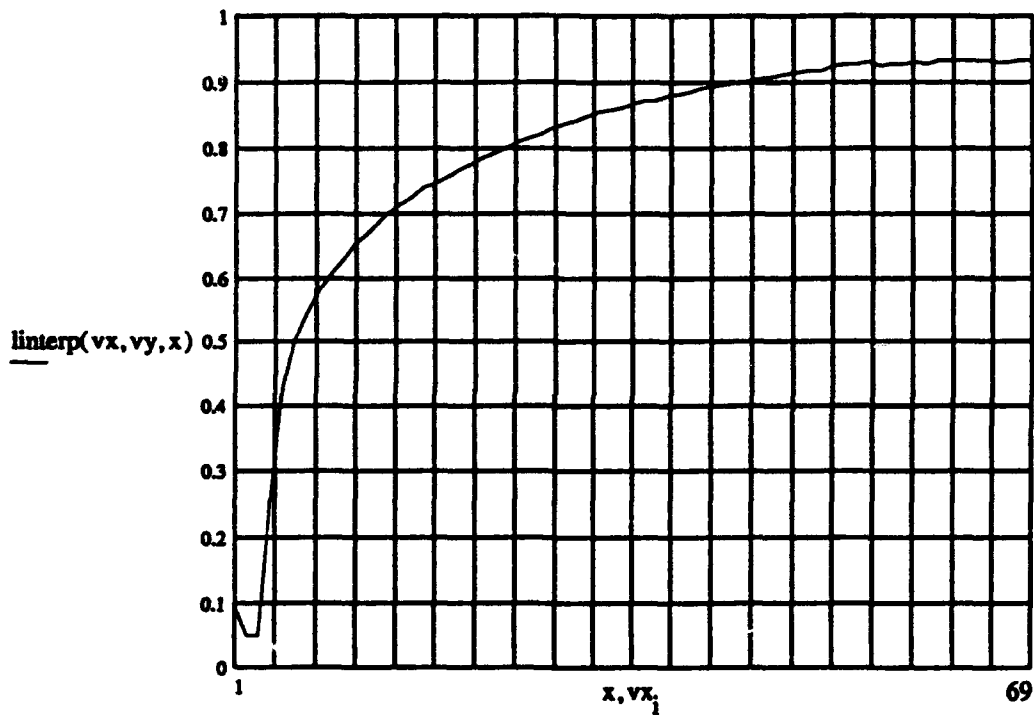
This file takes data from a .dat file built from the Matter.dat Surface Properties Data Compilation, and interpolates to build spectral reflectance vectors of 20 nm and 5 nm wavelength bandwidths.

```
i := 1..69
```

```
vxi := i            i vxi vyi x Counters and variables used to do the interpolation
```

```
vyi := READ(smcl8x)    Reads in data from the .dat file. To link variable name to filename, use "Associate Filename..." under File.
```

```
x := 1..69
```



10 nm (Original wavelength bandwidth)

Verify spectral reflectance graph is approximately equivalent to original the graph in the *Matter.dat Surface Properties Data Compilation*.

20 nm interpolation. The  $x_i$  is multiplied by the increment of  $2, \frac{20}{10}$  where 20 is the desired  $\Delta\lambda$  and 10 is the  $\Delta\lambda$  read in above.

$i := 1..35$

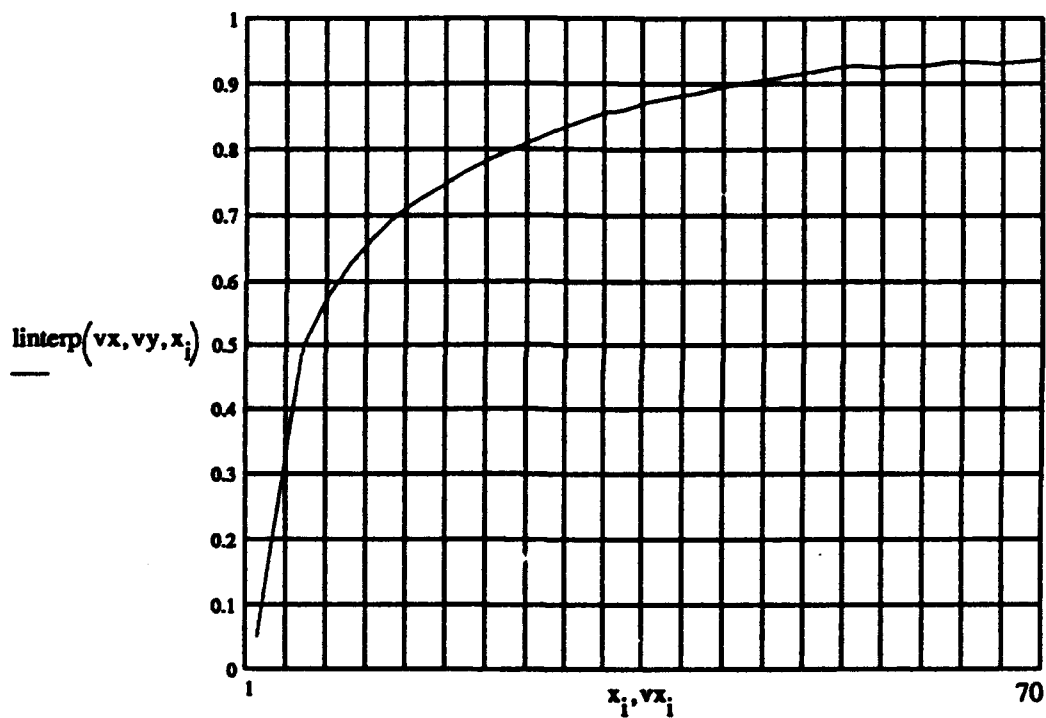
$x_i := i \frac{20}{10}$

$f := \overrightarrow{\text{linterp}(vx, vy, x)}$

length(f) = 36

WRITE(smc18xx) := f

Writes to INTRP^smc??xx.dat  
Change name to match SMC#.



20 nm Interpolation

Verify spectral reflectance graph is approximately equivalent to the original graph in the *Matter.dat Surface Properties Data Compilation*.

5 nm interpolation. The  $x_i$  is multiplied by the increment of  $.5, \frac{5}{10}$  where 5 is the desired  $\Delta\lambda$  and 10 is the  $\Delta\lambda$  read in above.

$i := 1..141$

$x_i := i \cdot \frac{5}{10}$

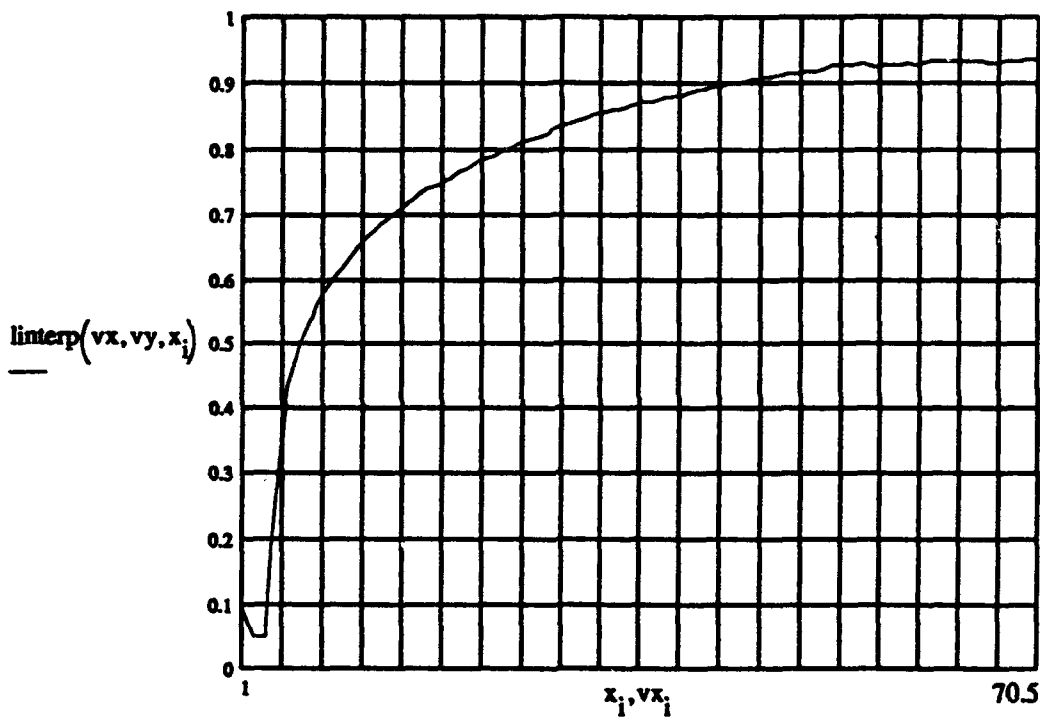
$f := \text{linterp}(vx, vy, x)$

$\text{length}(f) = 142$

$\text{WRITE}(smc18v) := f$

Writes to INTRP^smc??v.dat

Change name to match SMC#.



5 nm Interpolation

Verify spectral reflectance graph is approximately equivalent to the original graph in the *Matter.dat Surface Properties Data Compilation*.

### Radiometry

$\lambda_{lb} := 290\text{-nm}$      $\lambda_{ub} := 910\text{-nm}$     Wavelength lower and upper bound

$\Delta\lambda := 20\text{-nm}$     Wavelength bandwidth

$N := \frac{\lambda_{ub} - \lambda_{lb}}{\Delta\lambda}$      $N = 31$     Number of wavelength bands

$i := 1..N$     Counter

$b_i := i \cdot \Delta\lambda + \lambda_{lb}$     Upper limit incrementer for integral

$a_i := b_i - \Delta\lambda$     Lower limit incrementer for integral

$M_{bb}(\lambda) := \frac{2 \cdot \pi \cdot h \cdot c^2}{\lambda^5 \cdot \left( e^{\frac{h \cdot c}{\lambda \cdot k_B \cdot T}} - 1 \right)}$     Planck's formula

$x_i := \int_{a_i}^{b_i} \frac{M_{bb}(\lambda)}{h \cdot c \cdot \pi} \cdot \lambda \, d\lambda$      $P_i := x_i \cdot \left( \frac{R_{sun}}{r_{sun}} \right)^2$     Photon flux

$\rho_{02_i} := \text{READ}(\text{smc02xx})$     Spectral reflectivity

$\Omega := 10^{-12} \cdot \text{m}^2, 10^{-11.9} \cdot \text{m}^2 .. 10^{-10} \cdot \text{m}^2$     Range of  $\Omega$

$i_T(i) := q \cdot \Omega \cdot P_i \cdot \rho_{02_i}$     COUNT RATE CALCULATION

$t_d := 8 \cdot \text{sec}$     Integration time

$i_D := 12 \cdot q \cdot \text{sec}^{-1}$     Detector noise

$\sigma_m := 12$     noise

$\text{SNR}(i) := \frac{\frac{i_T(i)}{q} \cdot \sqrt{t_d}}{\sqrt{\frac{i_T(i)}{q} + \frac{i_D}{q}}}$

SNR CALCULATION

$\lambda_{mn_i} := \frac{a_i + b_i}{2}$     Mean wavelength     $z := 0, .01 .. 1.0$     Angles parameter

$\text{SNR}_{pix}(i) := \frac{z \cdot (\lambda_{mn_i})^2 \cdot P_i \cdot \rho_{02_i} \cdot t_d}{\sqrt{z \cdot (\lambda_{mn_i})^2 \cdot P_i \cdot \rho_{02_i} \cdot t_d + \sigma_m^2}}$      $\text{SNR}_{pix}$  CALCULATION



**20 nm bandwidth**

1 300	11 500	21 700	31 900
2 320	12 520	22 720	32 920
3 340	13 540	23 740	33 940
4 360	14 560	24 760	34 960
5 380	15 580	25 780	35 980
6 400	16 600	26 800	
7 420	17 620	27 820	
8 440	18 640	28 840	
9 460	19 660	29 860	
10 480	20 680	30 880	

**10 nm bandwidth**

1 300	11 400	21 500	31 600	41 700	51 800	61 900
2 310	12 410	22 510	32 610	42 710	52 810	62 910
3 320	13 420	23 520	33 620	43 720	53 820	63 920
4 330	14 430	24 530	34 630	44 730	54 830	64 930
5 340	15 440	25 540	35 640	45 740	55 840	65 940
6 350	16 450	26 550	36 650	46 750	56 850	66 950
7 360	17 460	27 560	37 660	47 760	57 860	67 960
8 370	18 470	28 570	38 670	48 770	58 870	68 970
9 380	19 480	29 580	39 680	49 780	59 880	69 980
10 390	20 490	30 590	40 690	50 790	60 890	70 990

**5 nm bandwidth**

1 300	11 350	21 400	31 450	41 500	51 550	61 600
2 305	12 355	22 405	32 455	42 505	52 555	62 605
3 310	13 360	23 410	33 460	43 510	53 560	63 610
4 315	14 365	24 415	34 465	44 515	54 565	64 615
5 320	15 370	25 420	35 470	45 520	55 570	65 620
6 325	16 375	26 425	36 475	46 525	56 575	66 625
7 330	17 380	27 430	37 480	47 530	57 580	67 630
8 335	18 385	28 435	38 485	48 535	58 585	68 635
9 340	19 390	29 440	39 490	49 540	59 590	69 640
10 345	20 395	30 445	40 495	50 545	60 595	70 645
71 650	81 700	91 750	101 800	111 850	121 900	131 950
72 655	82 705	92 755	102 805	112 855	122 905	132 955
73 660	83 710	93 760	103 810	113 860	123 910	133 960
74 665	84 715	94 765	104 815	114 865	124 915	134 965
75 670	85 720	95 770	105 820	115 870	125 920	135 970
76 675	86 725	96 775	106 825	116 875	126 925	136 975
77 680	87 730	97 780	107 830	117 880	127 930	137 980
78 685	88 735	98 785	108 835	118 885	128 935	138 985
79 690	89 740	99 790	109 840	119 890	129 940	139 990
80 695	90 745	100 795	110 845	120 895	130 945	140 995

## Appendix B. Case (1): 20 nm, 10 nm and 5 nm Graphs

### B.1 Legend

The legend for Case (1) graphs is given in Table B.1.

20 nm		10 nm		5 nm	
$i$	$\lambda$ (nm)	$i$	$\lambda$ (nm)	$i$	$\lambda$ (nm)
8	440	16	450	31	450
13	540	26	550	51	550
18	640	36	650	71	650
23	740	46	750	91	750
28	840	56	850	111	850

Table B.1 Legend, Case (1)

### B.2 20 nm graphs

Figure B.1 shows the target signal count rate  $i_T/q$  vs  $\Omega$  for Case (1),  $\Delta\lambda = 20$  nm. The vertical dashed line is the reference hypernormalized parameter,  $\Omega_{ref}$ , computed for the target.

Figure B.2 shows the SNR vs  $\Omega$  for Case (1),  $\Delta\lambda = 20$  nm. The vertical dashed line is the reference hypernormalized parameter,  $\Omega_{ref}$ , computed for the target.

Figure B.3 shows the  $SNR_{pix}$  vs  $z$  for Case (1),  $\Delta\lambda = 20$  nm.

### B.3 10 nm graphs

Figure B.4 shows the target signal count rate  $i_T/q$  vs  $\Omega$  for Case (1),  $\Delta\lambda = 10$  nm. The vertical dashed line is the reference hypernormalized parameter,  $\Omega_{ref}$ , computed for the target.

Figure B.5 shows the SNR vs  $\Omega$  for Case (1),  $\Delta\lambda = 10$  nm. The vertical dashed line is the reference hypernormalized parameter,  $\Omega_{ref}$ , computed for the target.

Figure B.6 shows the  $SNR_{pix}$  vs  $z$  for Case (1),  $\Delta\lambda = 10$  nm.

#### B.4 5 nm graphs

Figure B.7 shows the target signal count rate  $i_T/q$  vs  $\Omega$  for Case (1),  $\Delta\lambda = 5$  nm. The vertical dashed line is the reference hypernormalized parameter,  $\Omega_{ref}$ , computed for the target.

Figure B.8 shows the SNR vs  $\Omega$  for Case (1),  $\Delta\lambda = 5$  nm. The vertical dashed line is the reference hypernormalized parameter,  $\Omega_{ref}$ , computed for the target.

Figure B.9 shows the  $SNR_{pix}$  vs  $z$  for Case (1),  $\Delta\lambda = 5$  nm.

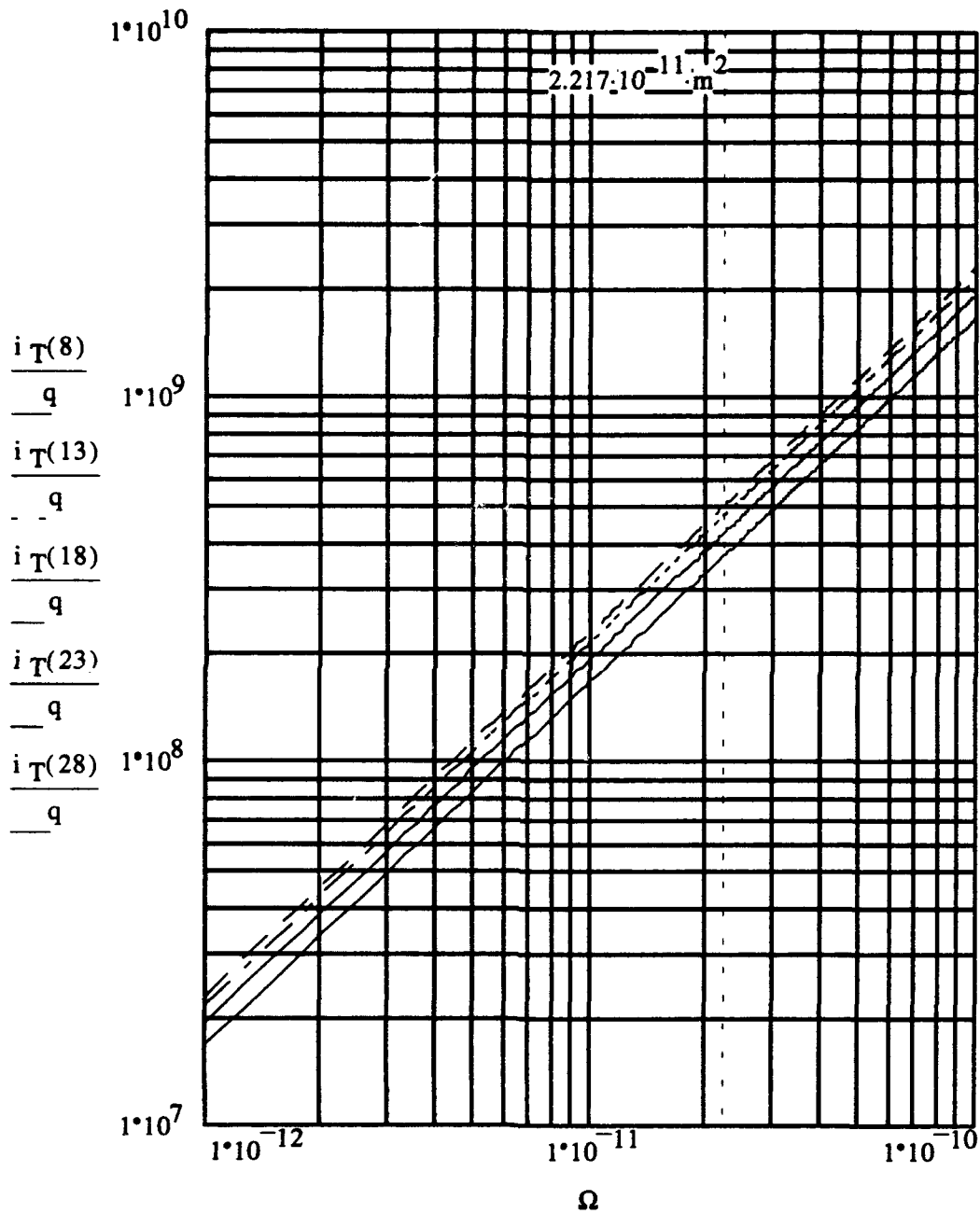


Figure B.1 Case (1), Count Rate  $\frac{i_T}{q}$  (1/s) vs  $\Omega$  ( $\text{rad m}^2$ ), 20 nm

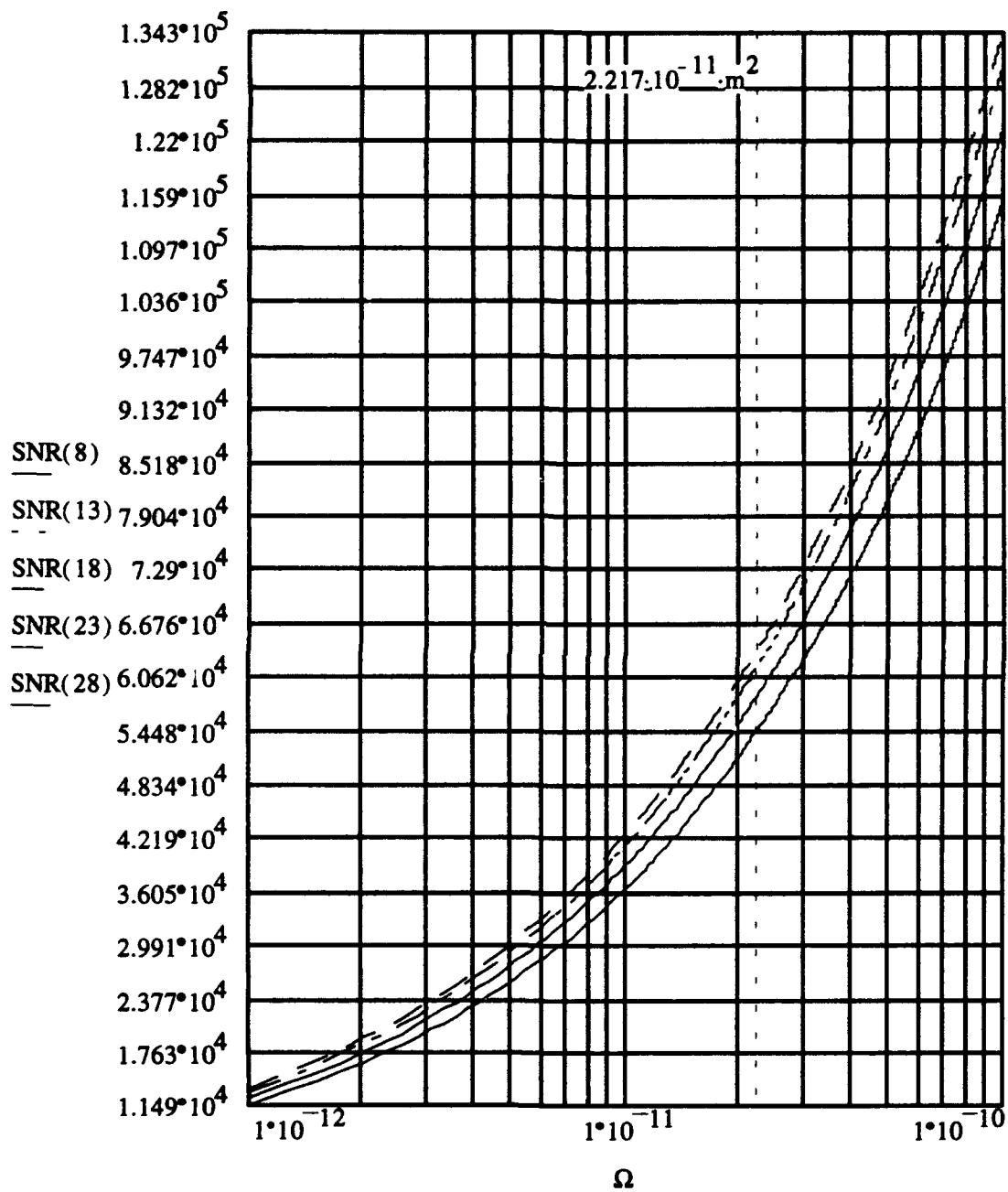


Figure B.2 Case (1), SNR vs  $\Omega$  ( $\text{rad m}^2$ ), 20 nm

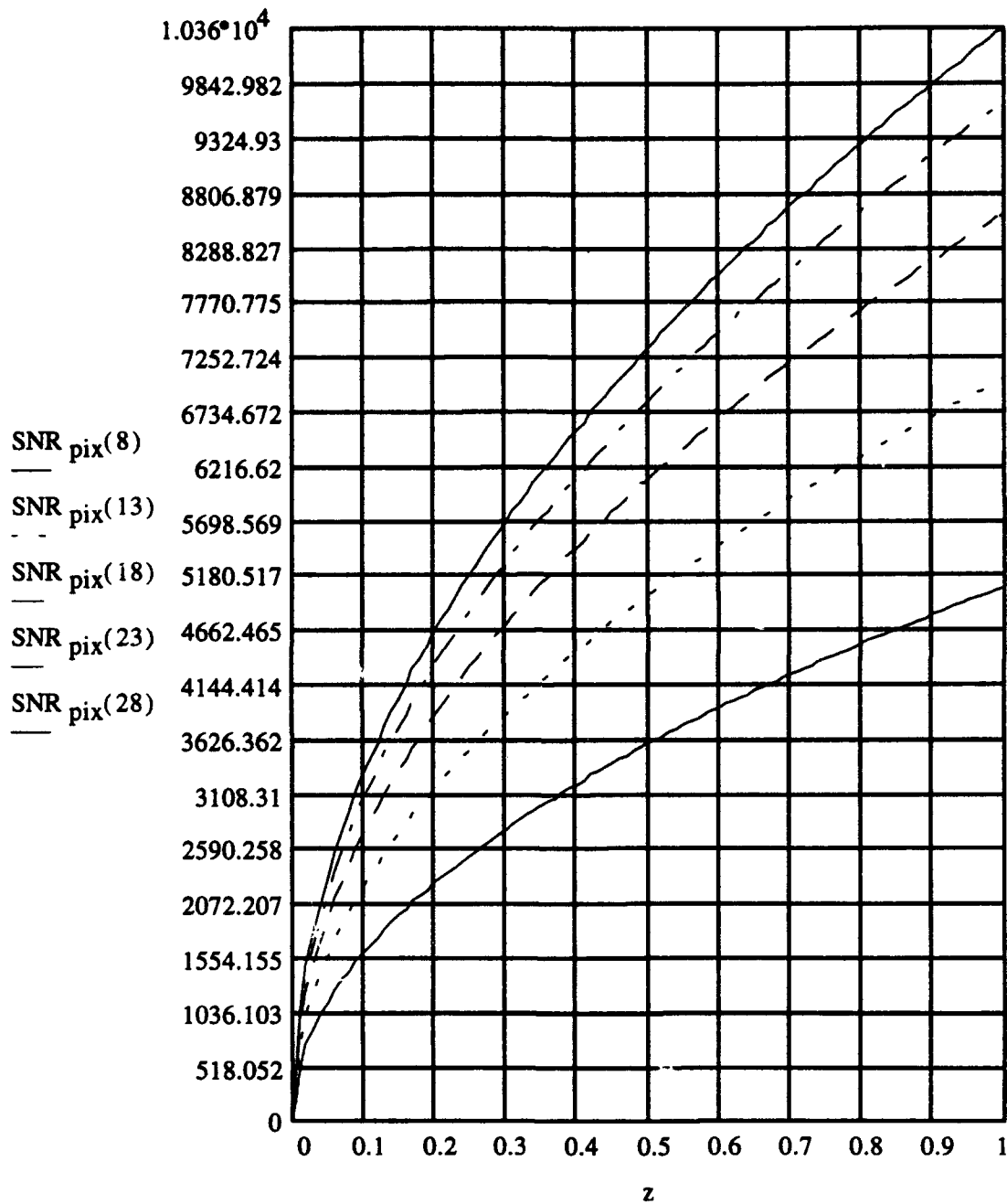


Figure B.3 Case (1),  $SNR_{pix}$  vs  $z$ , 20 nm

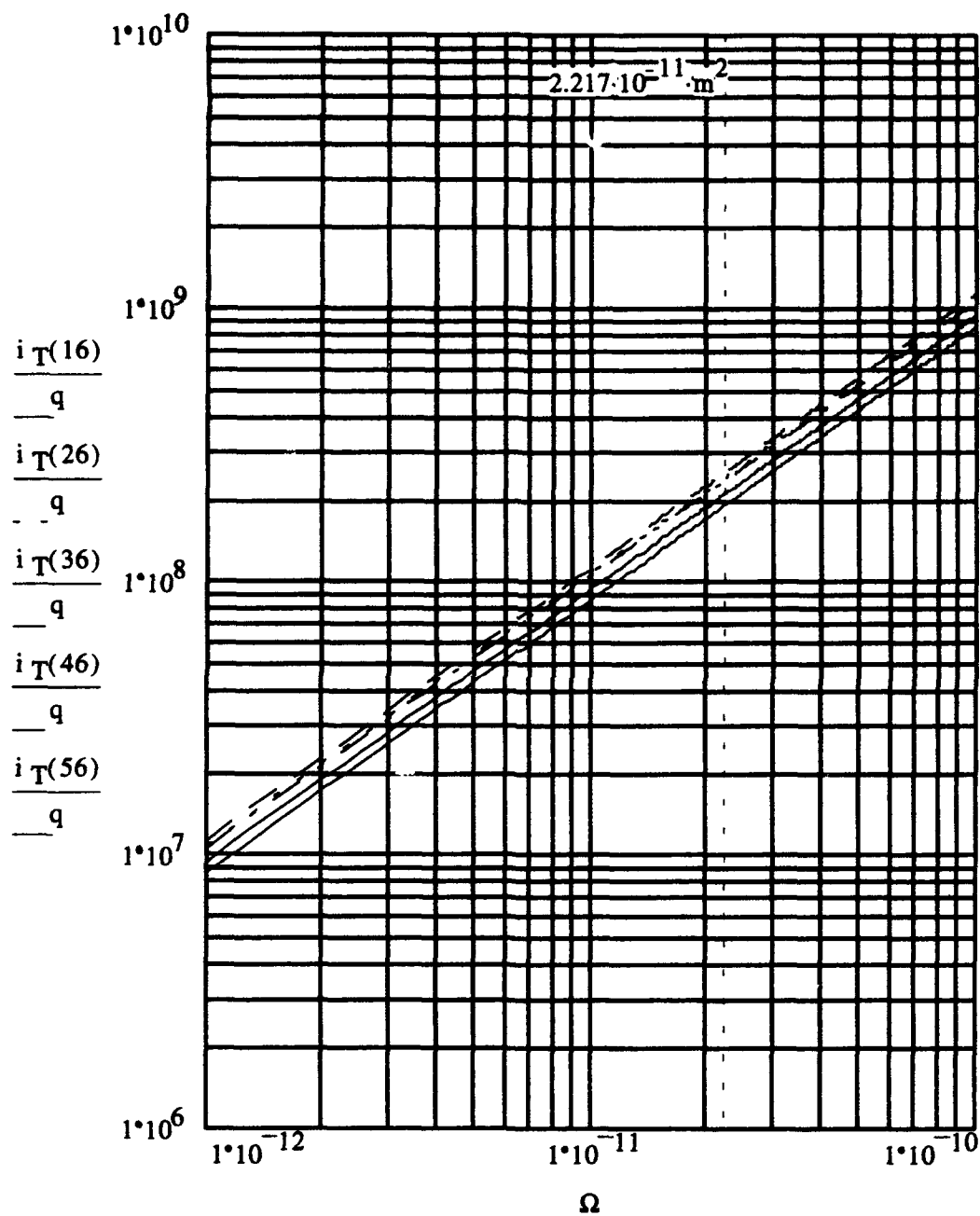


Figure B.4 Case (1), Count Rate  $\frac{i_T}{q}$  (1/s) vs  $\Omega$  (rad m<sup>2</sup>), 10 nm

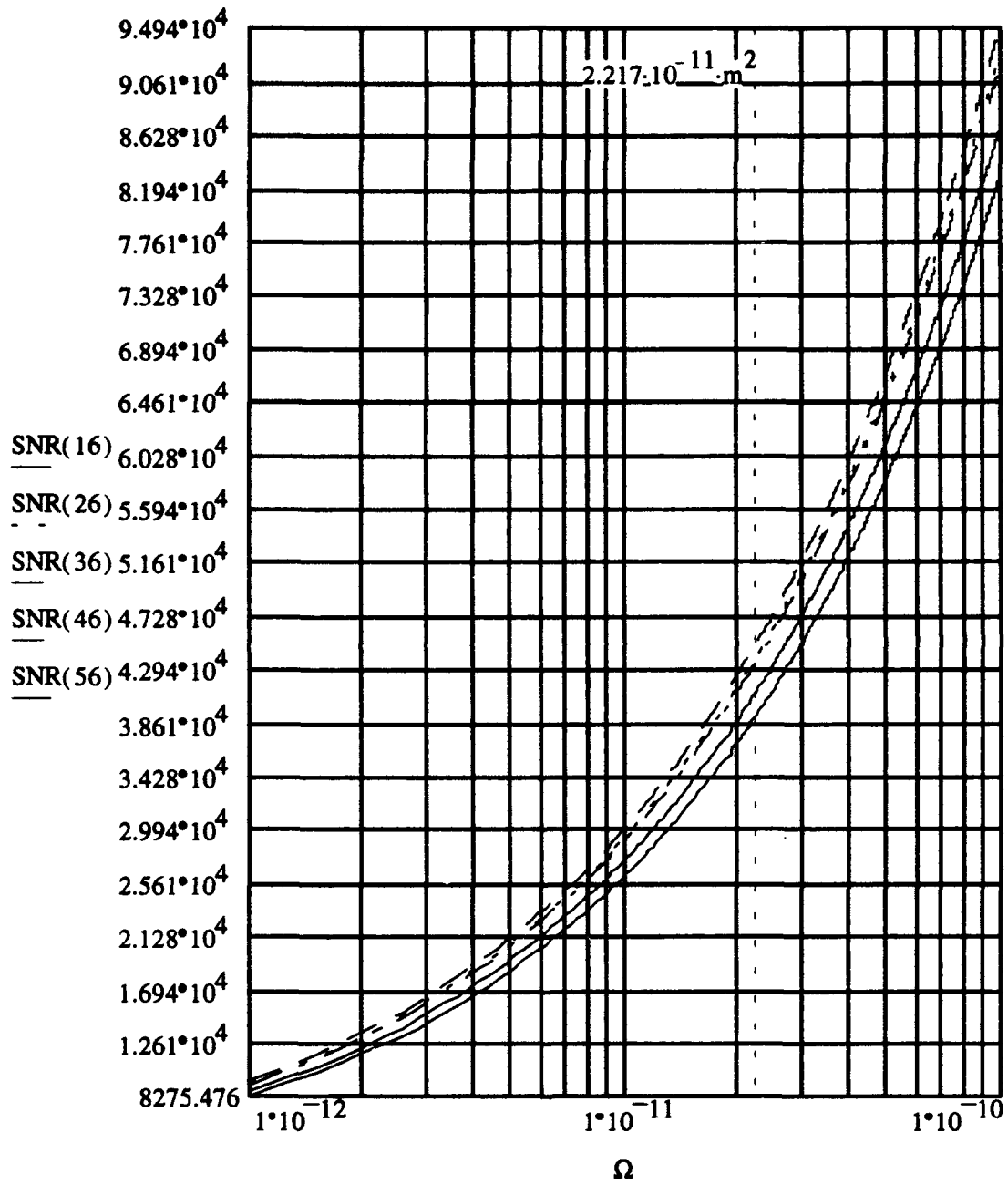


Figure B.5 Case (1), SNR vs  $\Omega$  ( $\text{rad m}^2$ ), 10 nm



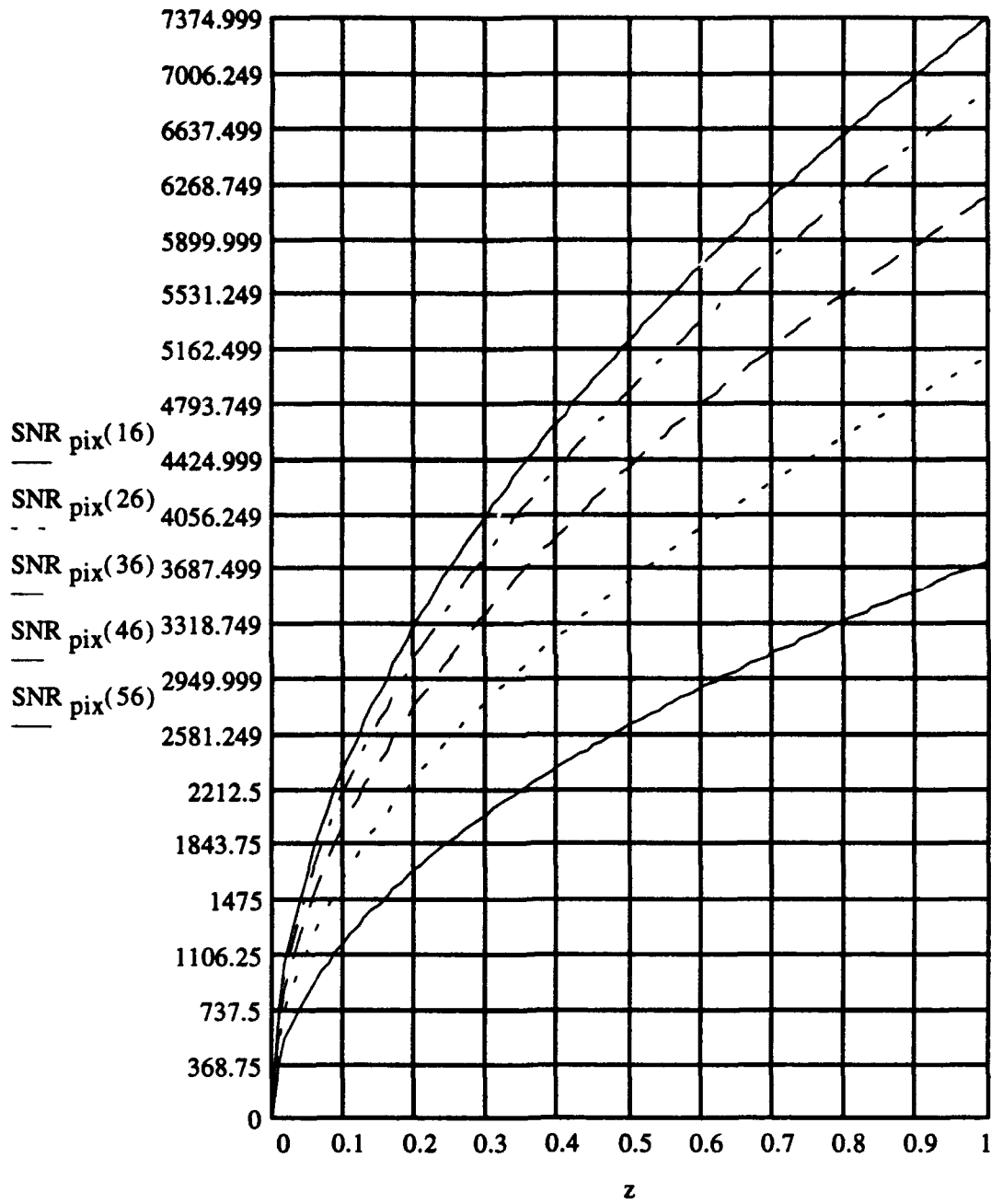


Figure B.6 Case (1),  $SNR_{pix}$  vs  $z$ , 10 nm

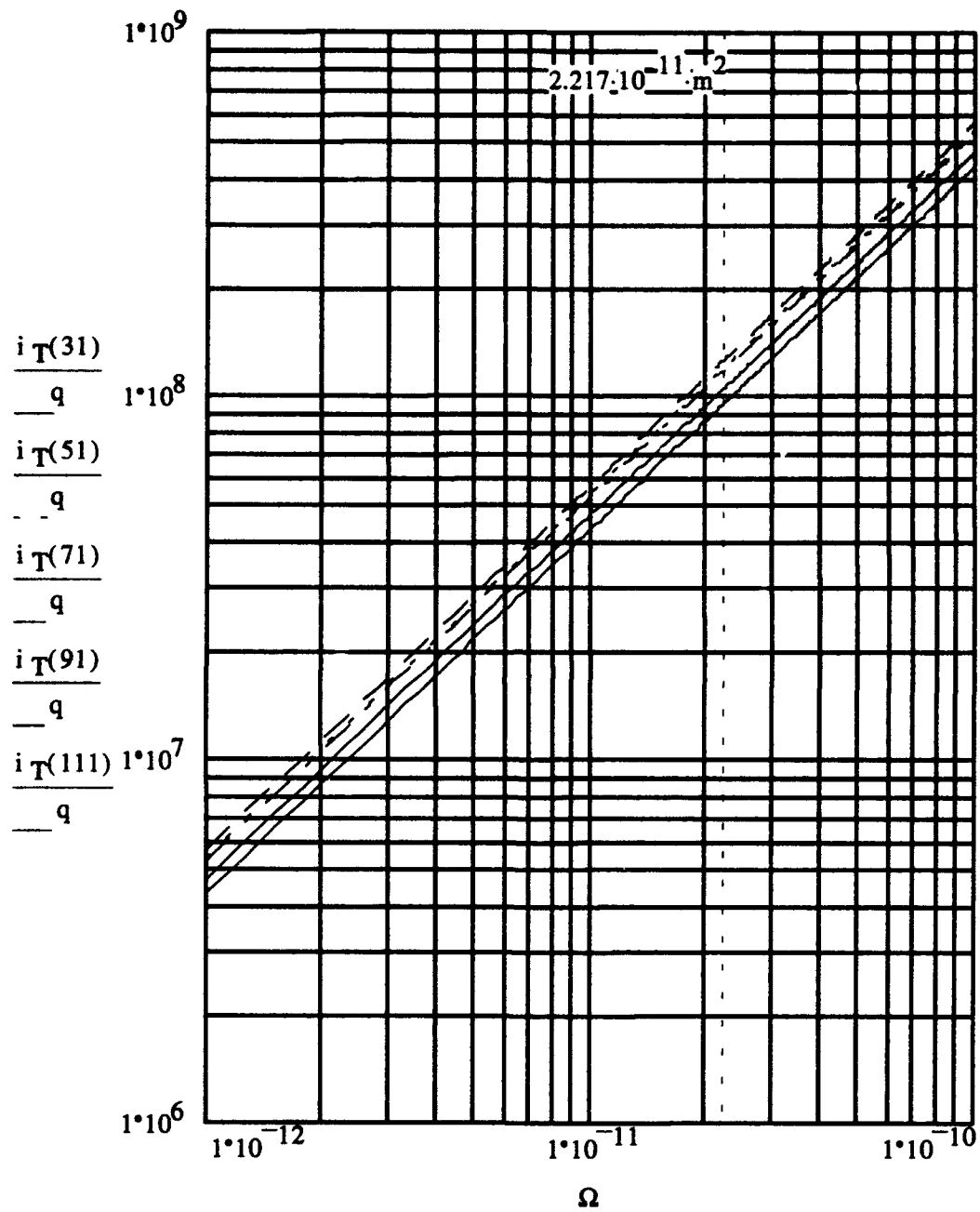


Figure B.7 Case (1), Count Rate  $\frac{i_T}{q}$  (1/s) vs  $\Omega$  ( $\text{rad m}^2$ ), 5 nm

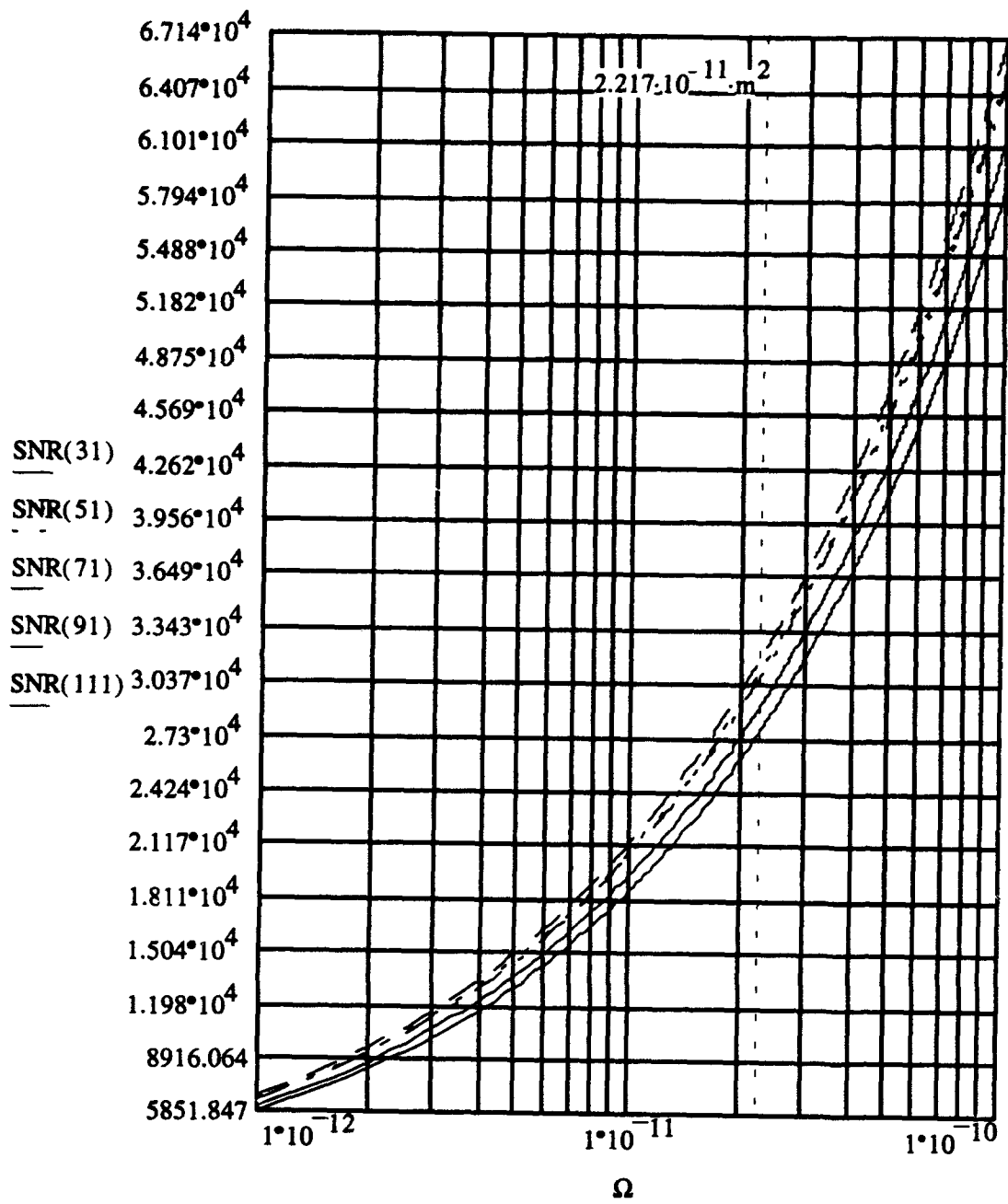


Figure B.8 Case (1), SNR vs  $\Omega$  ( $\text{rad m}^2$ ), 5 nm

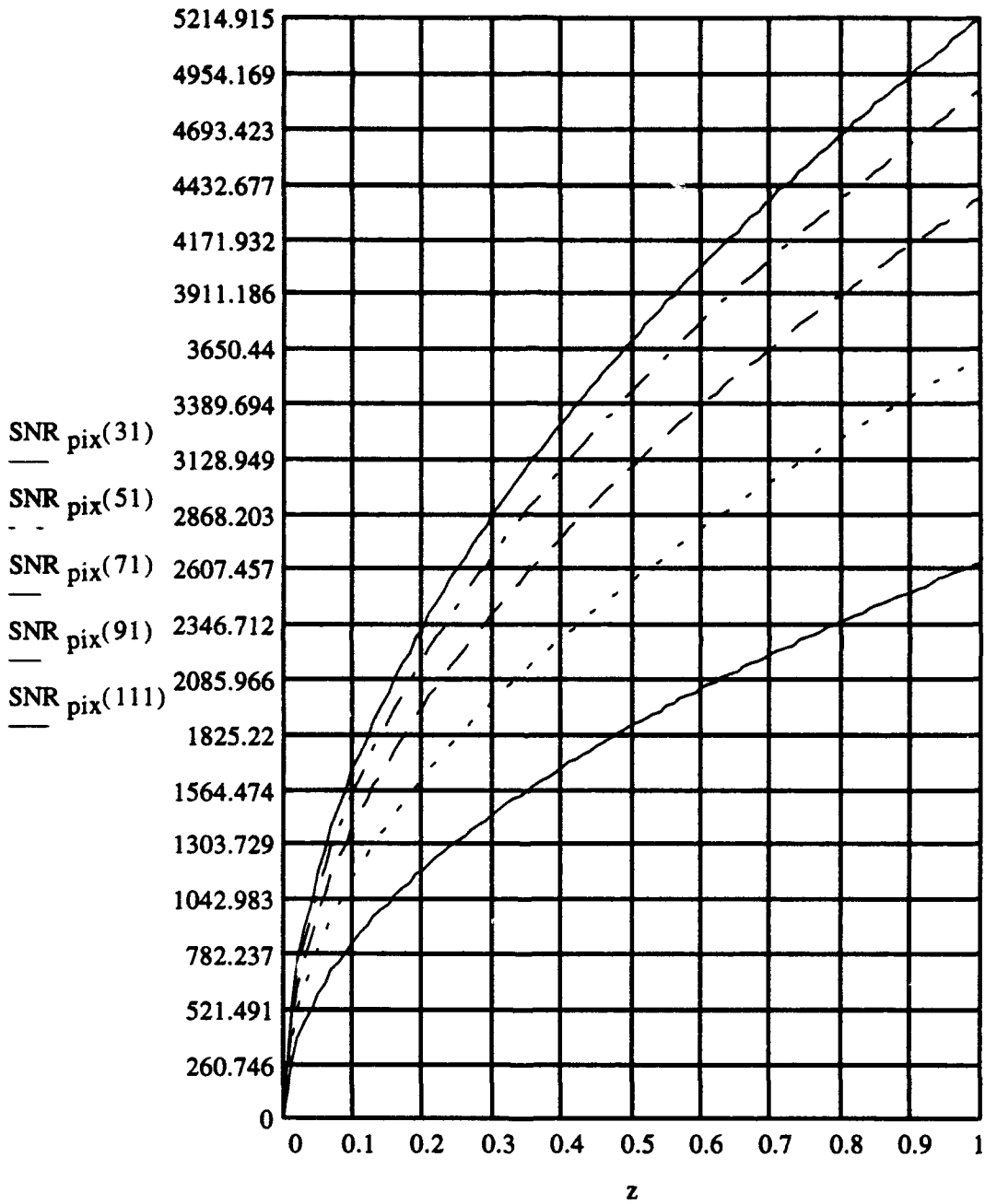


Figure B.9 Case (1),  $SNR_{pix}$  vs  $z$ , 5 nm

## Appendix C. Case (2): 20 nm, 10 nm and 5 nm Graphs

### C.1 Legend

The legend for Case (2) graphs is given in Table C.1.

20 nm		10 nm		5 nm	
$i$	$\lambda$ (nm)	$i$	$\lambda$ (nm)	$i$	$\lambda$ (nm)
8	440	16	450	31	450
13	540	26	550	51	550
18	640	36	650	71	650
23	740	46	750	91	750
28	840	56	850	111	850

Table C.1 Legend, Case (2)

### C.2 20 nm graphs

Figure C.1 shows the target signal count rate  $i_T/q$  vs  $\Omega$  for Case (2),  $\Delta\lambda = 20$  nm. The vertical dashed line is the reference hypernormalized parameter,  $\Omega_{ref}$ , computed for the target.

Figure C.2 shows the SNR vs  $\Omega$  for Case (2),  $\Delta\lambda = 20$  nm. The vertical dashed line is the reference hypernormalized parameter,  $\Omega_{ref}$ , computed for the target.

Figure C.3 shows the  $SNR_{pix}$  vs  $z$  for Case (2),  $\Delta\lambda = 20$  nm.

### C.3 10 nm graphs

Figure C.4 shows the target signal count rate  $i_T/q$  vs  $\Omega$  for Case (2),  $\Delta\lambda = 10$  nm. The vertical dashed line is the reference hypernormalized parameter,  $\Omega_{ref}$ , computed for the target.

Figure C.5 shows the SNR vs  $\Omega$  for Case (2),  $\Delta\lambda = 10$  nm. The vertical dashed line is the reference hypernormalized parameter,  $\Omega_{ref}$ , computed for the target.

Figure C.6 shows the  $SNR_{pix}$  vs  $z$  for Case (2),  $\Delta\lambda = 10$  nm.

#### C.4 5 nm graphs

Figure C.7 shows the target signal count rate  $i_T/q$  vs  $\Omega$  for Case (2),  $\Delta\lambda = 5$  nm. The vertical dashed line is the reference hypernormalized parameter,  $\Omega_{ref}$ , computed for the target.

Figure C.8 shows the SNR vs  $\Omega$  for Case (2),  $\Delta\lambda = 5$  nm. The vertical dashed line is the reference hypernormalized parameter,  $\Omega_{ref}$ , computed for the target.

Figure C.9 shows the  $SNR_{pix}$  vs  $z$  for Case (2),  $\Delta\lambda = 5$  nm.

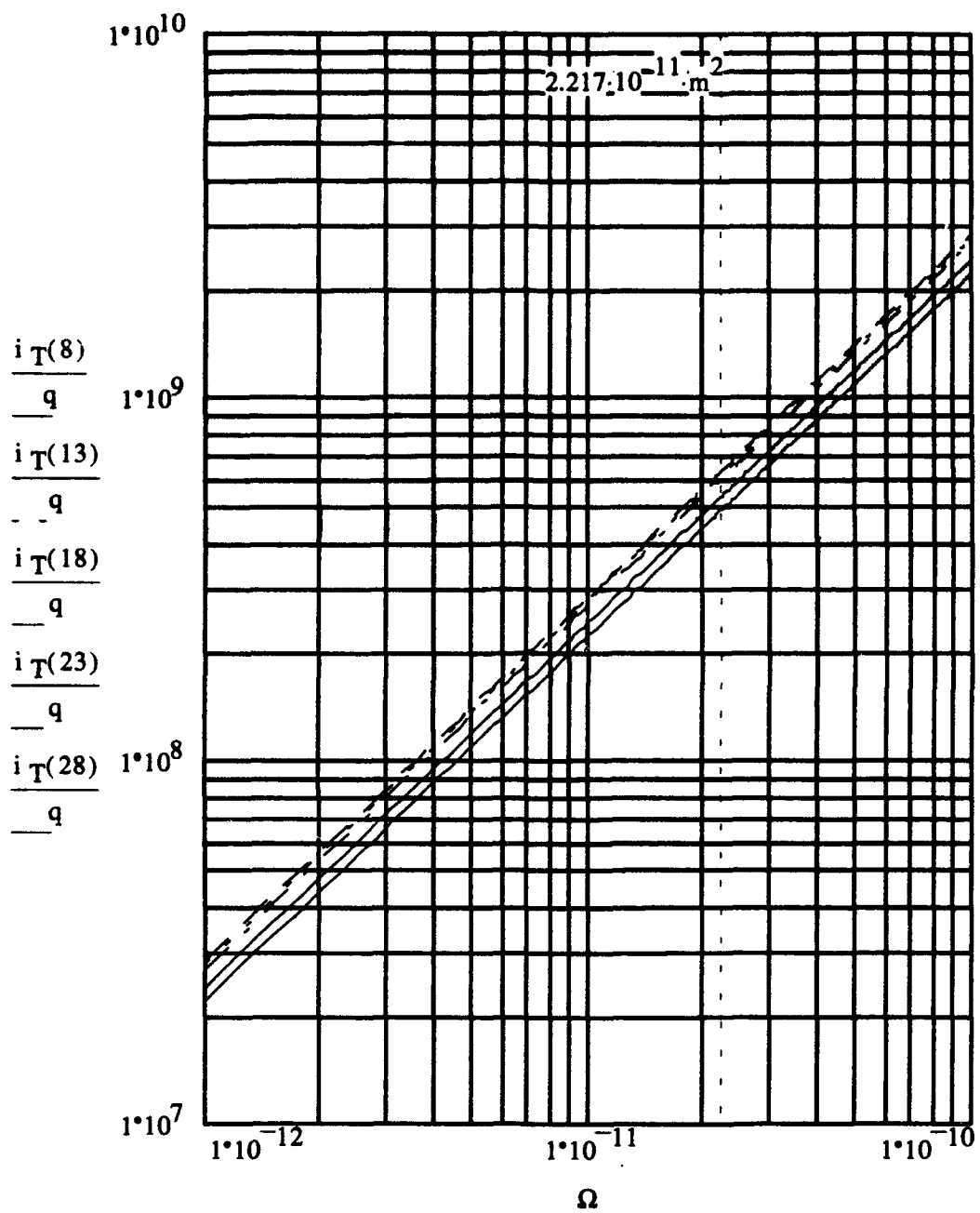


Figure C.1 Case (2), Count Rate  $\frac{i_T}{q}$  (1/s) vs  $\Omega$  (rad m<sup>2</sup>), 20 nm

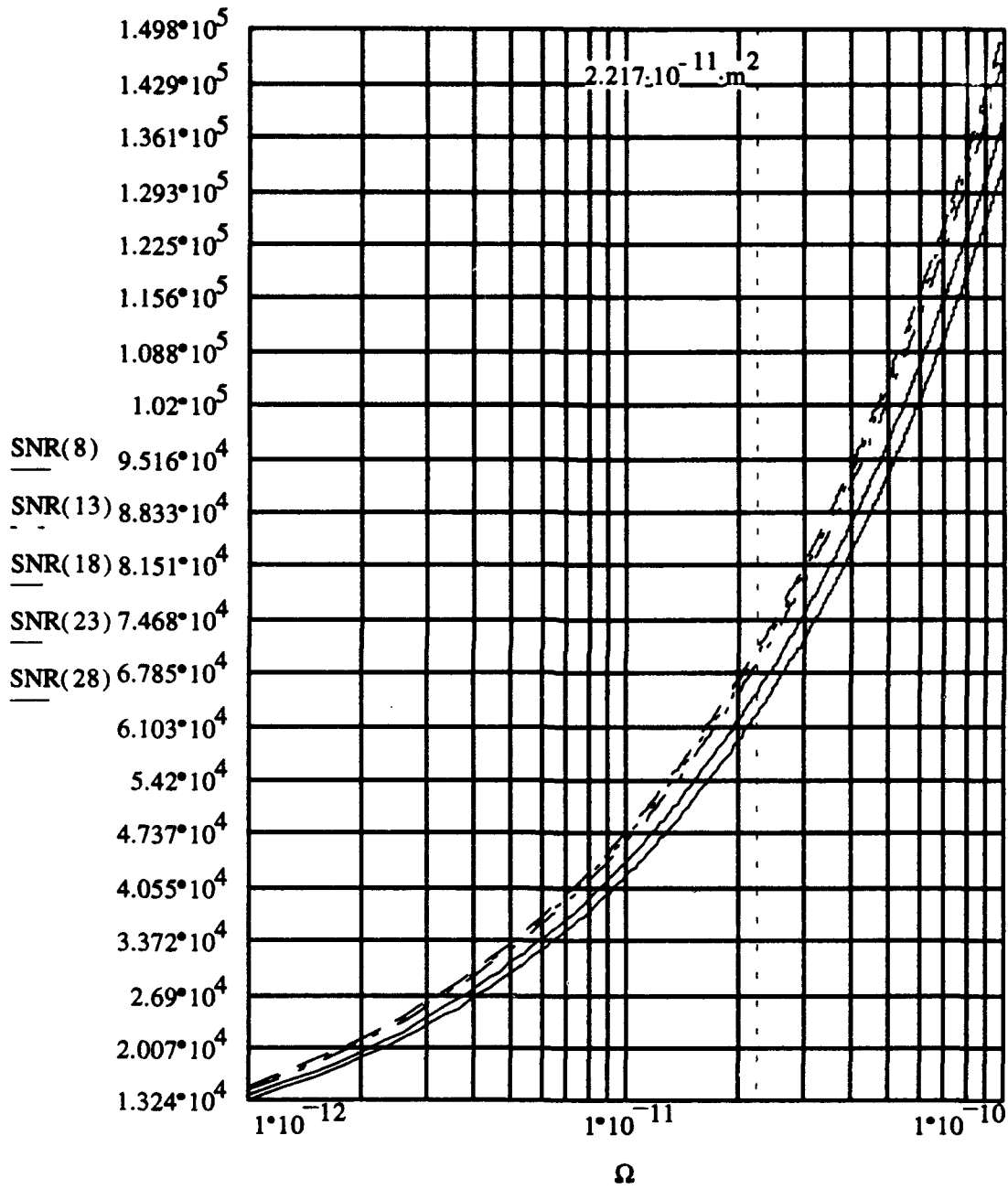


Figure C.2 Case (2), SNR vs  $\Omega$  ( $\text{rad m}^2$ ), 20 nm



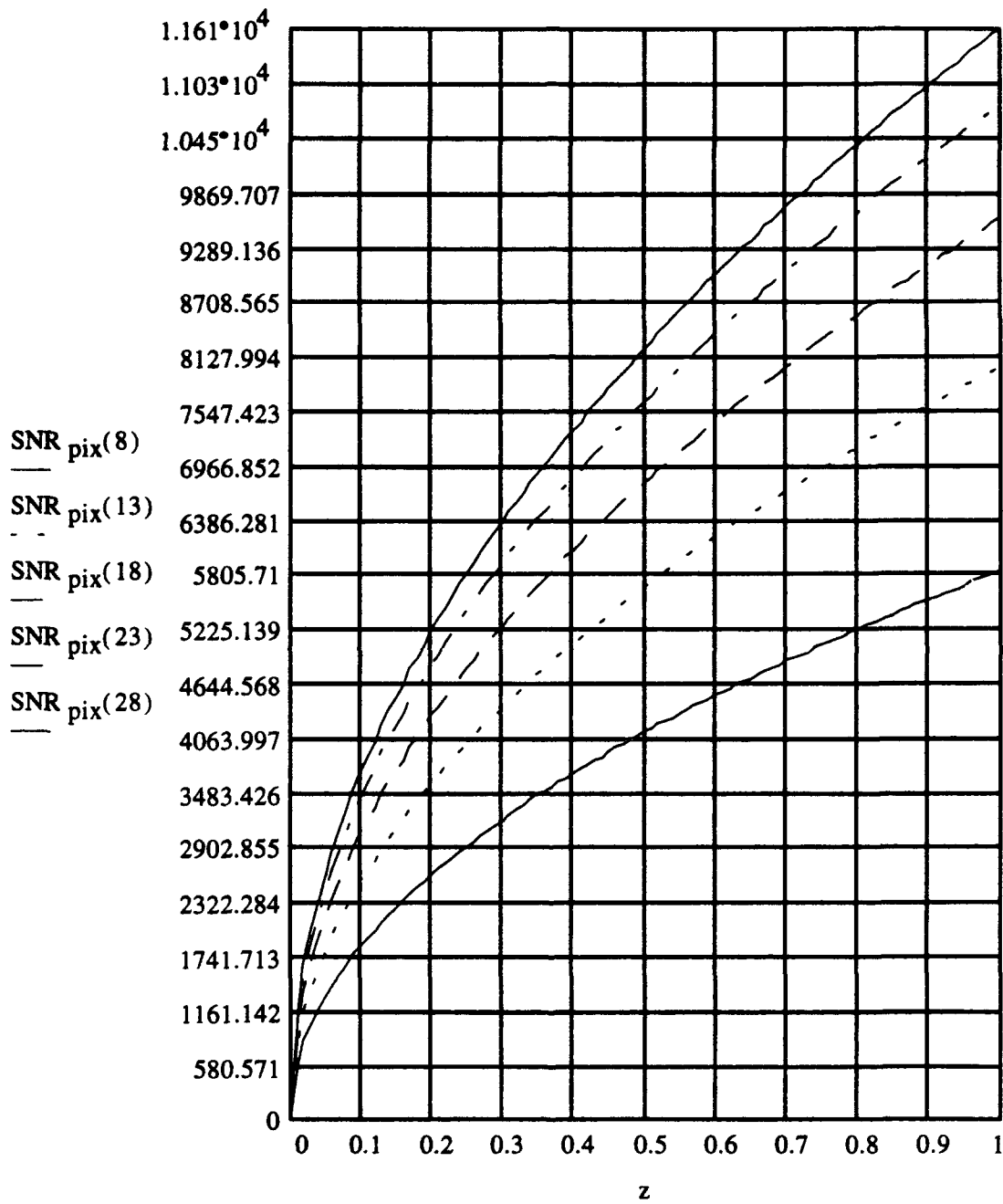


Figure C.3 Case (2),  $SNR_{pix}$  vs  $z$ , 20 nm

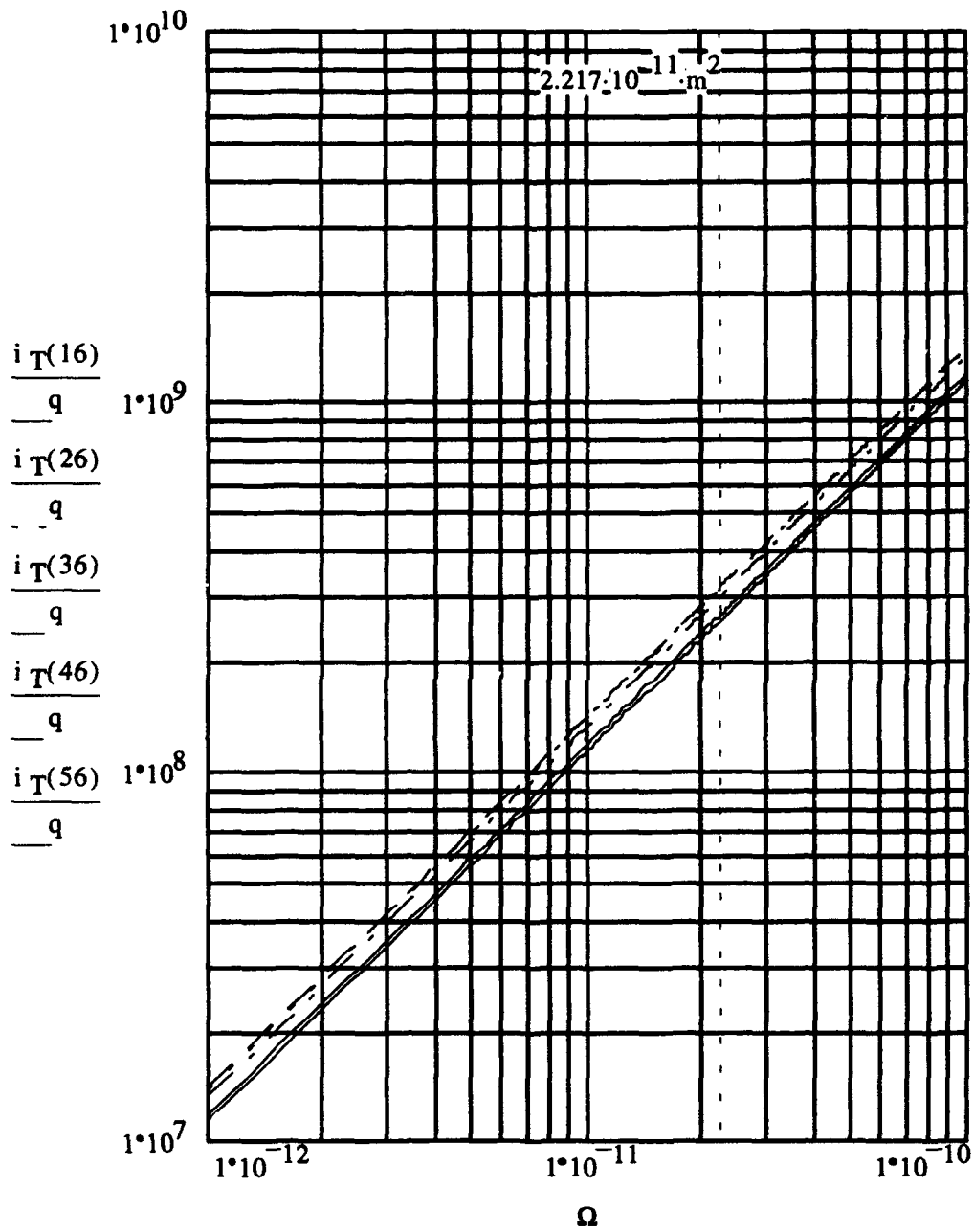


Figure C.4 Case (2), Count Rate  $\frac{i_T}{q}$  (1/s) vs  $\Omega$  ( $\text{rad m}^2$ ), 10 nm

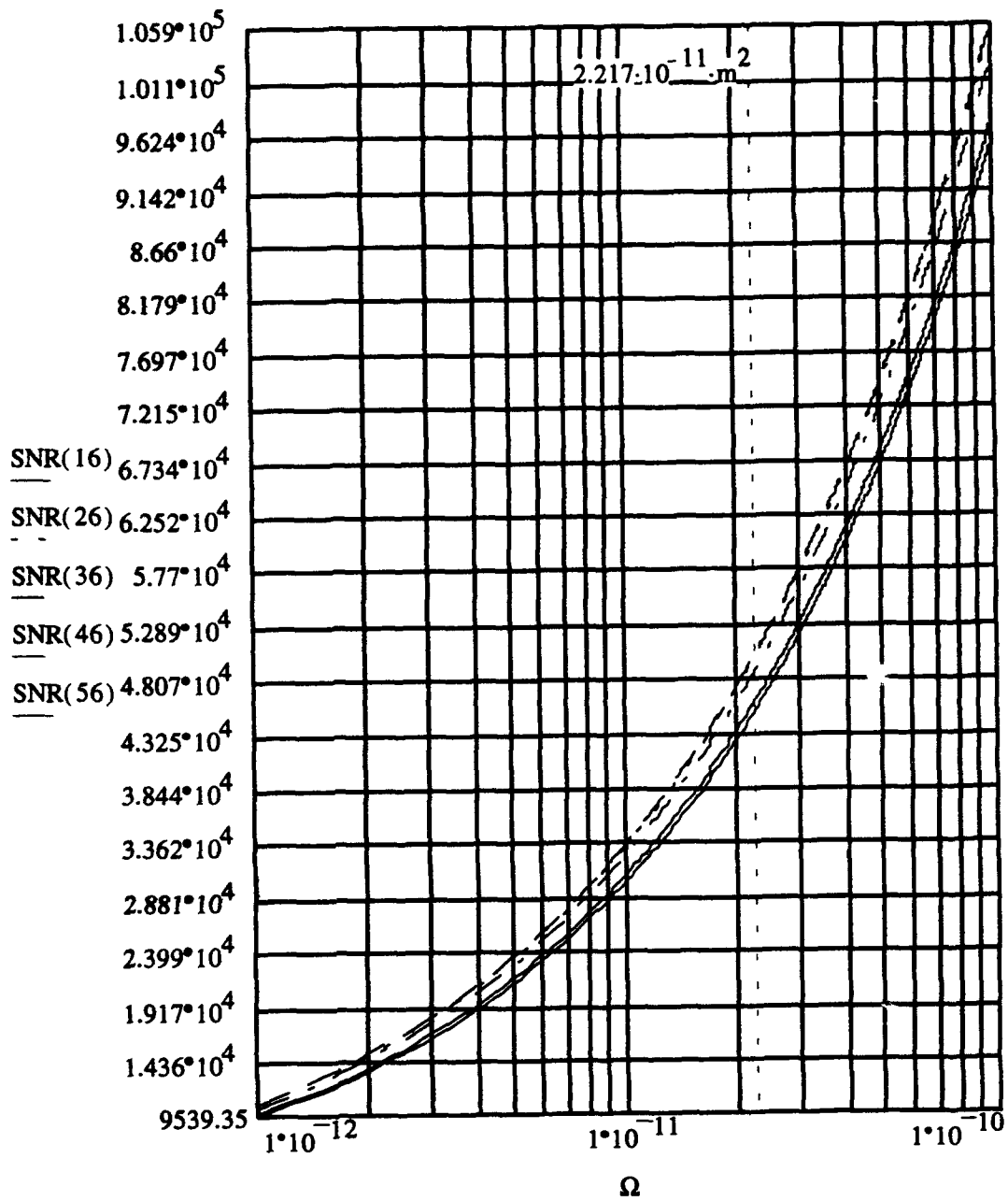


Figure C.5 Case (2), SNR vs  $\Omega$  ( $\text{rad m}^2$ ), 10 nm

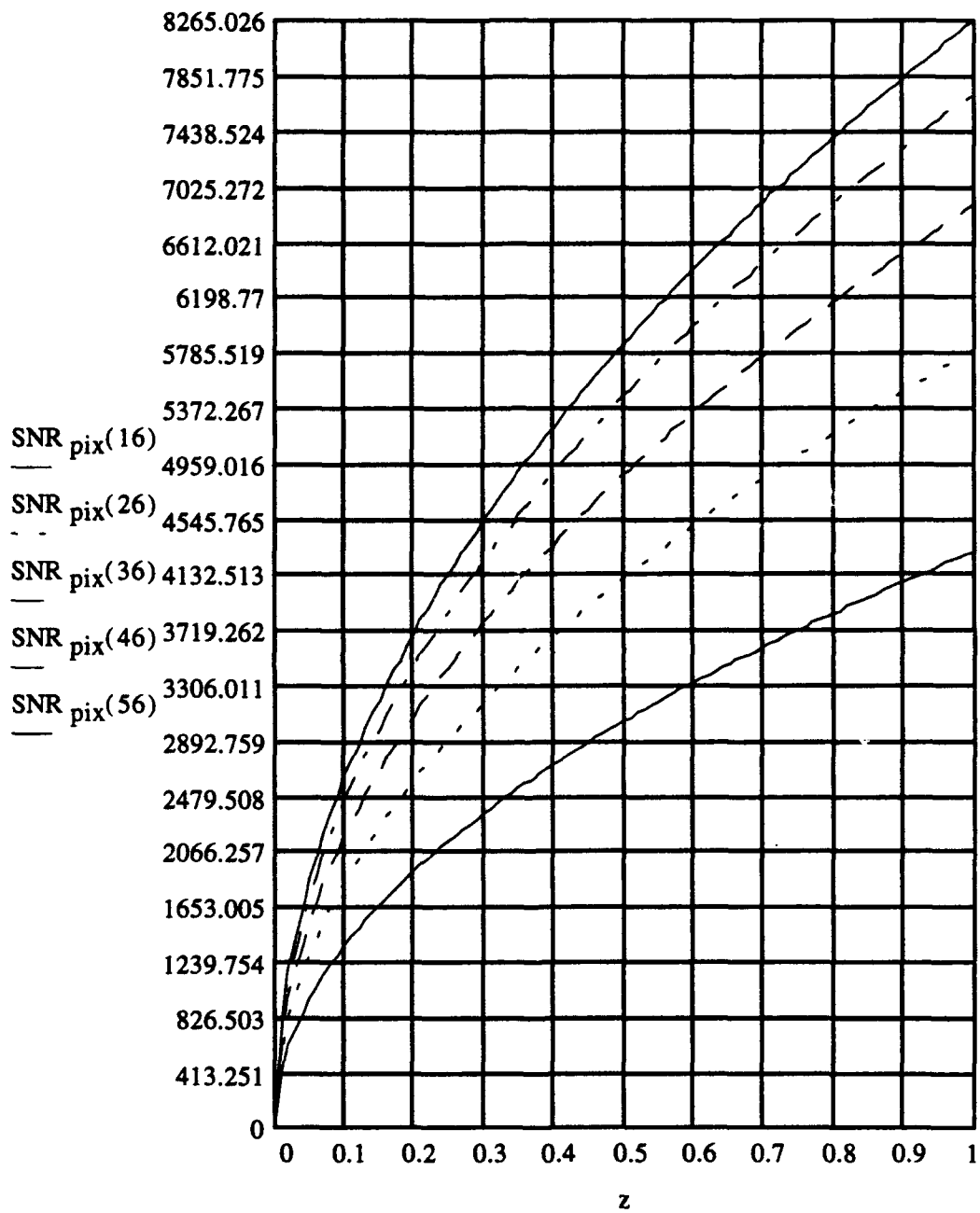


Figure C.6 Case (2),  $SNR_{pix}$  vs  $z$ , 10 nm

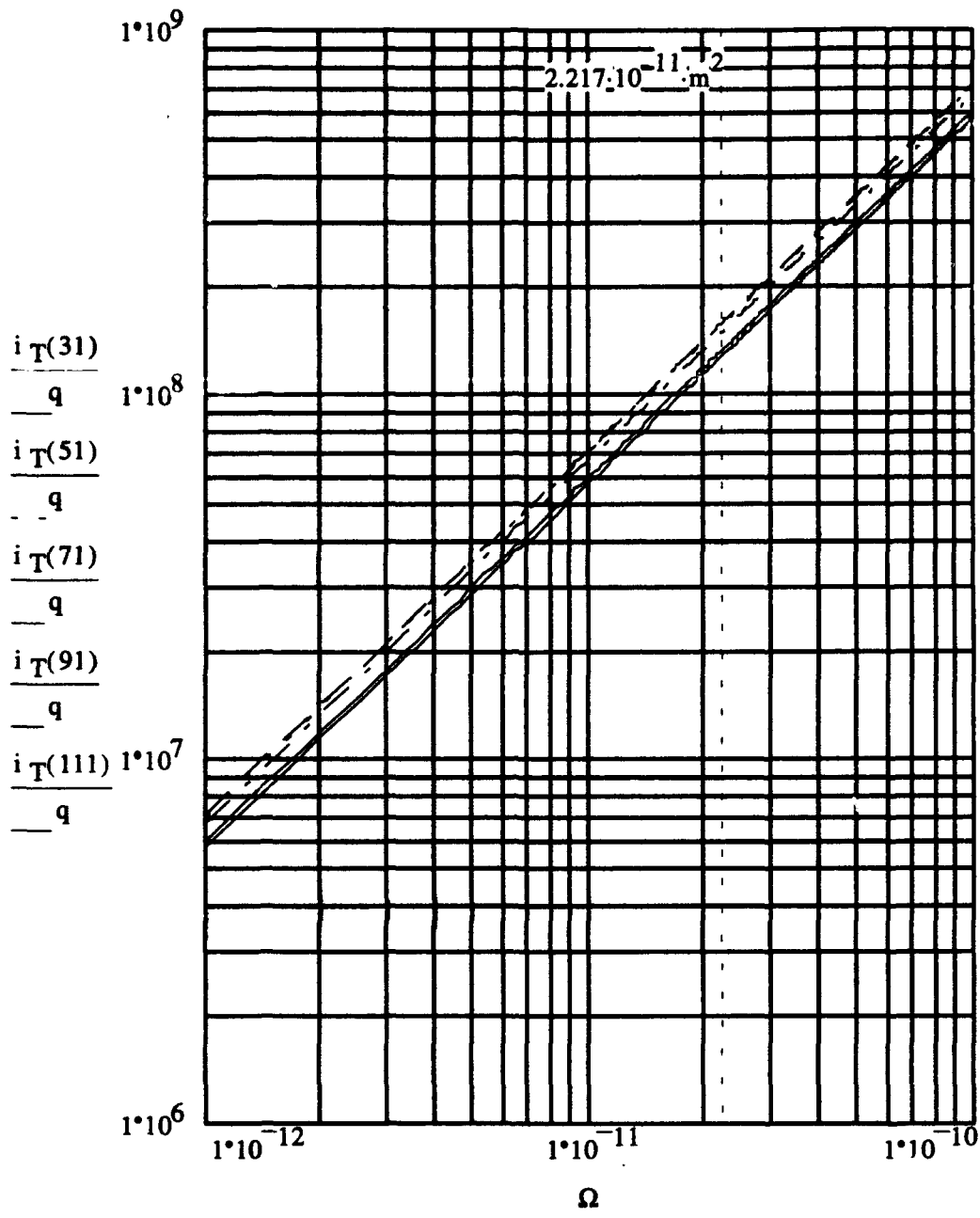


Figure C.7 Case (2), Count Rate  $\frac{i_T}{q}$  (1/s) vs  $\Omega$  ( $\text{rad m}^2$ ), 5 nm

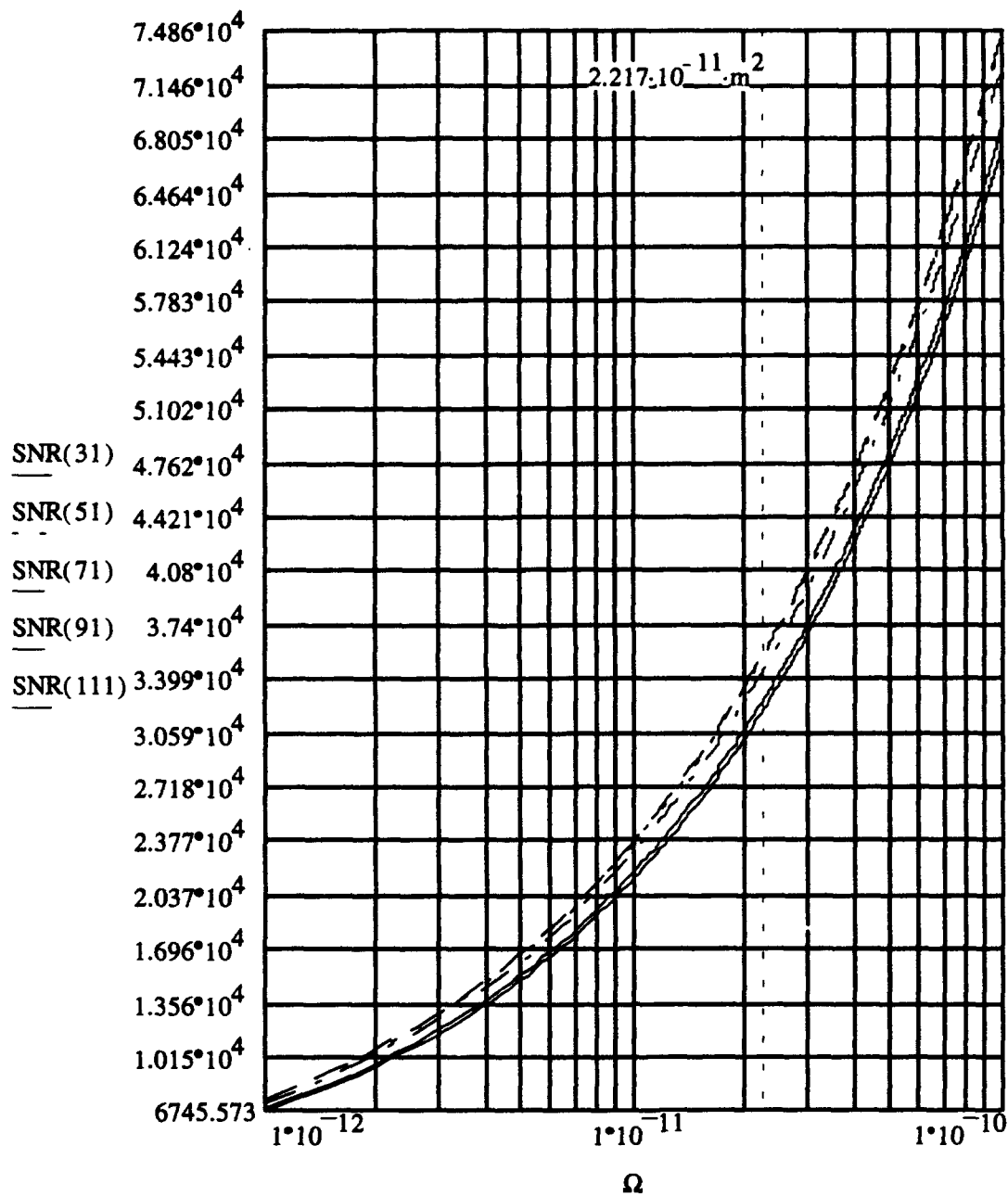


Figure C.8 Case (2), SNR vs  $\Omega$  ( $\text{rad m}^2$ ), 5 nm

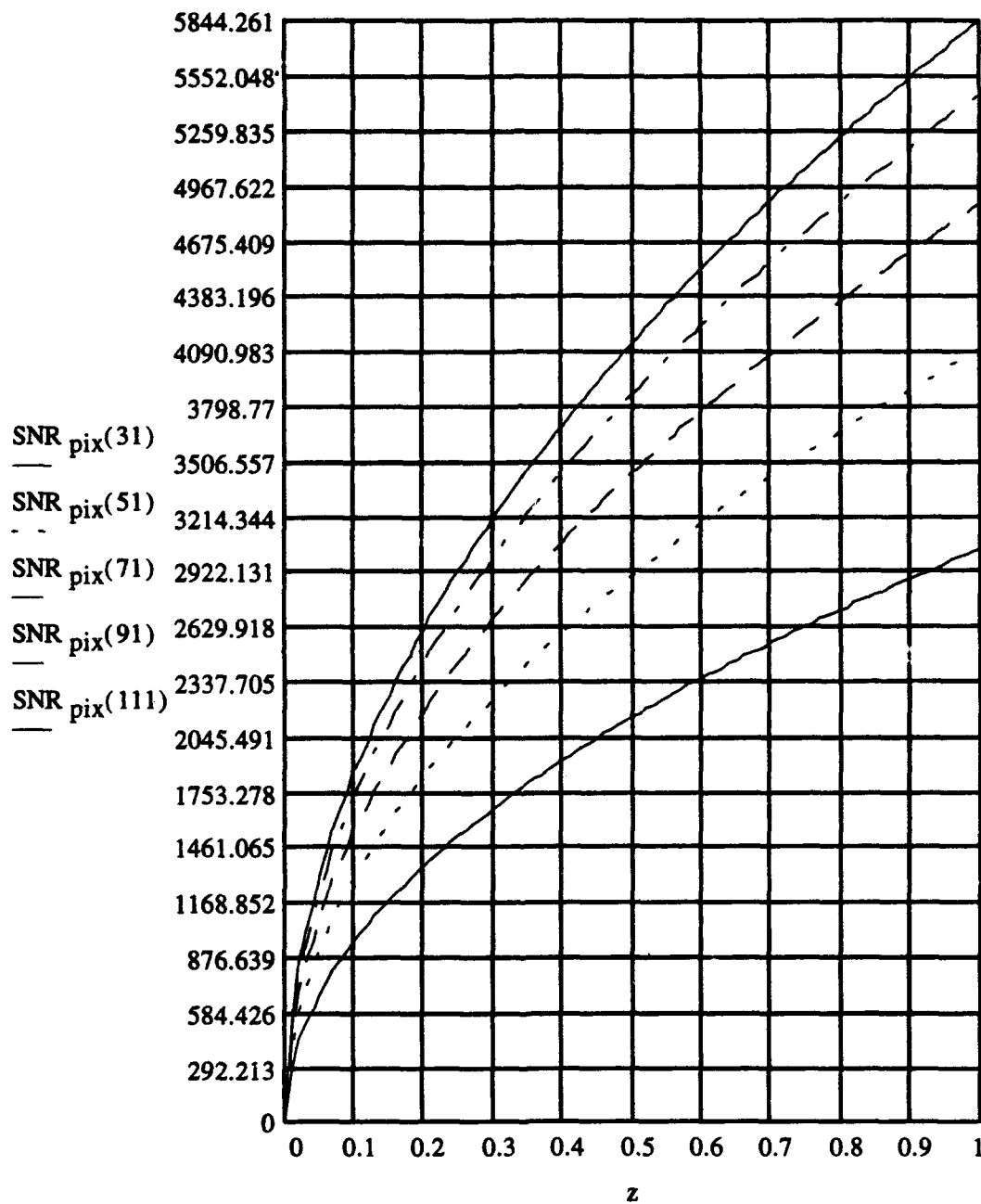


Figure C.9 Case (2),  $SNR_{pix}$  vs  $z$ , 5 nm

*Appendix D. Case (3): 20 nm, 10 nm and 5 nm Graphs*

*D.1 Legend*

Table D.1 shows the legend for Case (3) graphs.

	i			$\bar{\lambda}$ (nm)
	20 nm	10 nm	5 nm	
UV	1	1	1	300
	2	3	5	320
	3	5	9	340
	4	7	13	360
	5	9	17	380
	6	11	21	400
B	5	9	17	380
	6	11	21	400
	7	13	25	420
	8	15	29	440
	9	17	33	460
	10	19	37	480
	11	21	41	500
	12	23	45	520
V	10	19	37	480
	11	21	41	500
	12	23	45	520
	13	25	49	540
	14	27	53	560
	15	29	57	580
	16	31	61	600
	17	33	65	620
	18	35	69	640

Table D.1 Legend, Case (3)



## D.2 20 nm graphs

D.2.1 *Ultraviolet (UV), 300 nm - 400 nm.* Figure D.1 shows the target signal count rate  $i_T/q$  vs  $\Omega$  for Case (3),  $\Delta\lambda = 20$  nm. The vertical dashed line is the reference hypernormalized parameter,  $\Omega_{ref}$ , computed for the target.

Figure D.2 shows the SNR vs  $\Omega$  for Case (3),  $\Delta\lambda = 20$  nm. The vertical dashed line is the reference hypernormalized parameter,  $\Omega_{ref}$ , computed for the target.

D.2.2 *Blue (B), 380 nm - 540 nm.* Figure D.3 shows the target signal count rate  $i_T/q$  vs  $\Omega$  for Case (3),  $\Delta\lambda = 20$  nm. The vertical dashed line is the reference hypernormalized parameter,  $\Omega_{ref}$ , computed for the target.

Figure D.4 shows the SNR vs  $\Omega$  for Case (3),  $\Delta\lambda = 20$  nm. The vertical dashed line is the reference hypernormalized parameter,  $\Omega_{ref}$ , computed for the target.

D.2.3 *Visible (V), 480 nm - 650 nm.* Figure D.5 shows the target signal count rate  $i_T/q$  vs  $\Omega$  for Case (3),  $\Delta\lambda = 20$  nm. The vertical dashed line is the reference hypernormalized parameter,  $\Omega_{ref}$ , computed for the target.

Figure D.6 shows the SNR vs  $\Omega$  for Case (3),  $\Delta\lambda = 20$  nm. The vertical dashed line is the reference hypernormalized parameter,  $\Omega_{ref}$ , computed for the target.

## D.3 10 nm graphs

D.3.1 *Ultraviolet (UV), 300 nm - 400 nm.* Figure D.7 shows the target signal count rate  $i_T/q$  vs  $\Omega$  for Case (3),  $\Delta\lambda = 10$  nm. The vertical dashed line is the reference hypernormalized parameter,  $\Omega_{ref}$ , computed for the target.

Figure D.8 shows the SNR vs  $\Omega$  for Case (3),  $\Delta\lambda = 10$  nm. The vertical dashed line is the reference hypernormalized parameter,  $\Omega_{ref}$ , computed for the target.

*D.3.2 Blue (B), 380 nm - 540 nm.* Figure D.9 shows the target signal count rate  $i_T/q$  vs  $\Omega$  for Case (3),  $\Delta\lambda = 10$  nm. The vertical dashed line is the reference hypernormalized parameter,  $\Omega_{ref}$ , computed for the target.

Figure D.10 shows the SNR vs  $\Omega$  for Case (3),  $\Delta\lambda = 10$  nm. The vertical dashed line is the reference hypernormalized parameter,  $\Omega_{ref}$ , computed for the target.

*D.3.3 Visible (V), 480 nm - 650 nm.* Figure D.11 shows the target signal count rate  $i_T/q$  vs  $\Omega$  for Case (3),  $\Delta\lambda = 10$  nm. The vertical dashed line is the reference hypernormalized parameter,  $\Omega_{ref}$ , computed for the target.

Figure D.12 shows the SNR vs  $\Omega$  for Case (3),  $\Delta\lambda = 10$  nm. The vertical dashed line is the reference hypernormalized parameter,  $\Omega_{ref}$ , computed for the target.

#### *D.4 5 nm graphs*

*D.4.1 Ultraviolet (UV), 300 nm - 400 nm.* Figure D.13 shows the target signal count rate  $i_T/q$  vs  $\Omega$  for Case (3),  $\Delta\lambda = 5$  nm. The vertical dashed line is the reference hypernormalized parameter,  $\Omega_{ref}$ , computed for the target.

Figure D.14 shows the SNR vs  $\Omega$  for Case (3),  $\Delta\lambda = 5$  nm. The vertical dashed line is the reference hypernormalized parameter,  $\Omega_{ref}$ , computed for the target.

*D.4.2 Blue (B), 380 nm - 540 nm.* Figure D.15 shows the target signal count rate  $i_T/q$  vs  $\Omega$  for Case (3),  $\Delta\lambda = 5$  nm. The vertical dashed line is the reference hypernormalized parameter,  $\Omega_{ref}$ , computed for the target.

Figure D.16 shows the SNR vs  $\Omega$  for Case (3),  $\Delta\lambda = 5$  nm. The vertical dashed line is the reference hypernormalized parameter,  $\Omega_{ref}$ , computed for the target.

*D.4.3 Visible (V), 480 nm - 650 nm.* Figure D.17 shows the target signal count rate  $i_T/q$  vs  $\Omega$  for Case (3),  $\Delta\lambda = 5$  nm. The vertical dashed line is the reference hypernormalized parameter,  $\Omega_{ref}$ , computed for the target.

Figure D.18 shows the SNR vs  $\Omega$  for Case (3),  $\Delta\lambda = 5$  nm. The vertical dashed line is the reference hypernormalized parameter,  $\Omega_{ref}$ , computed for the target.

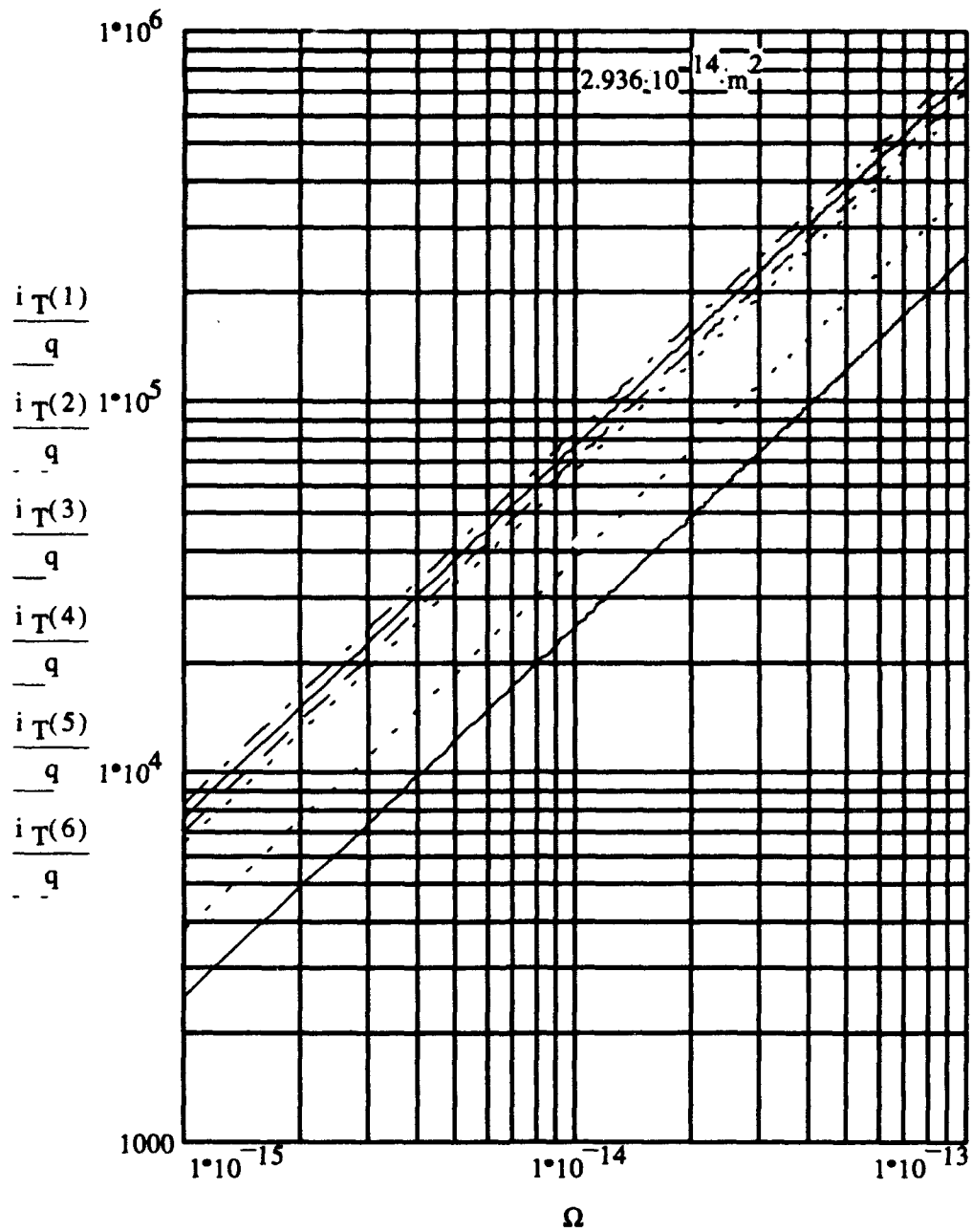


Figure D.1 Case (3), Count Rate  $\frac{i_T}{q}$  (1/s) vs  $\Omega$  ( $\text{rad m}^2$ ) (UV), 20 nm

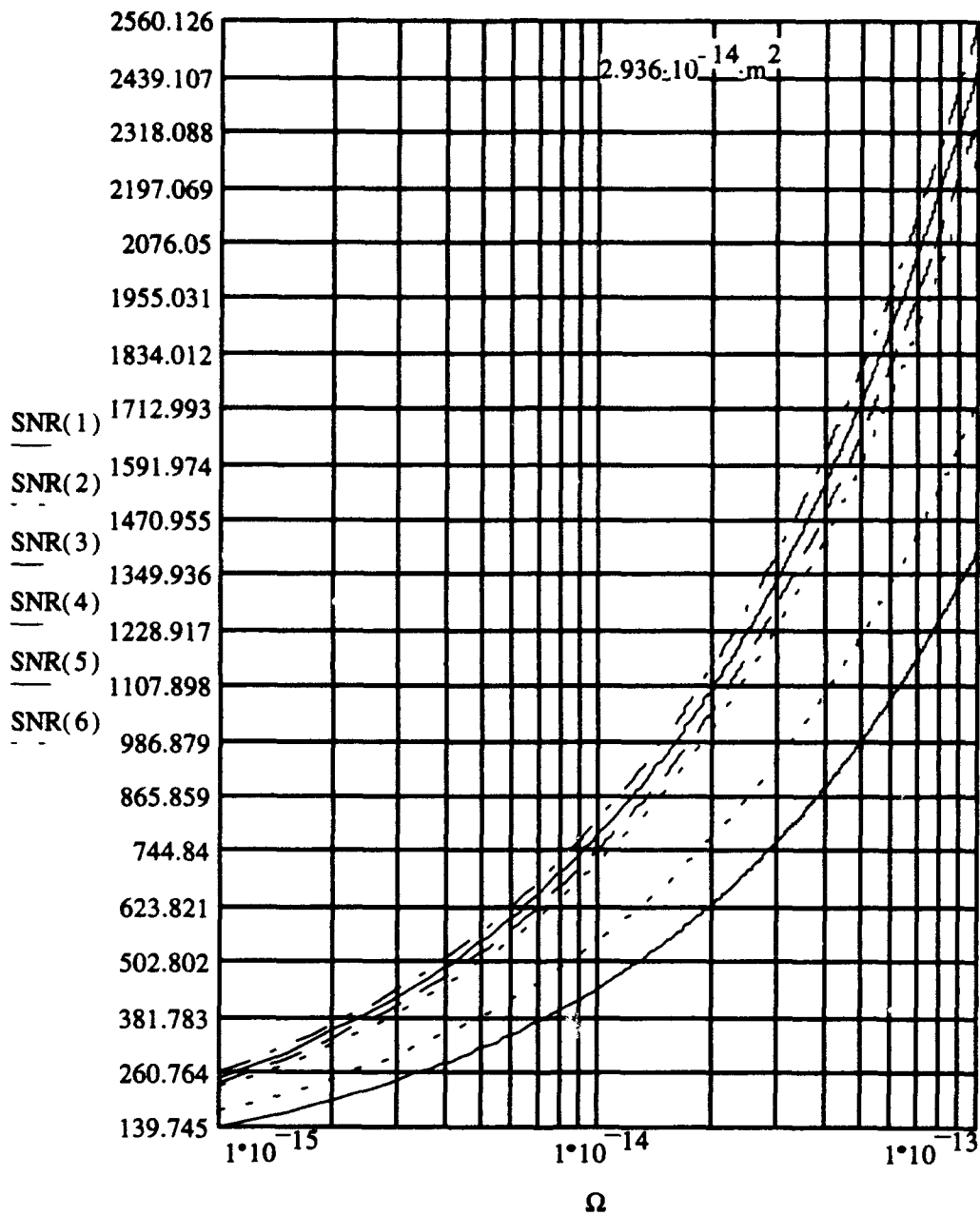


Figure D.2 Case (3), SNR vs  $\Omega$  ( $\text{rad m}^2$ ) (UV), 20 nm

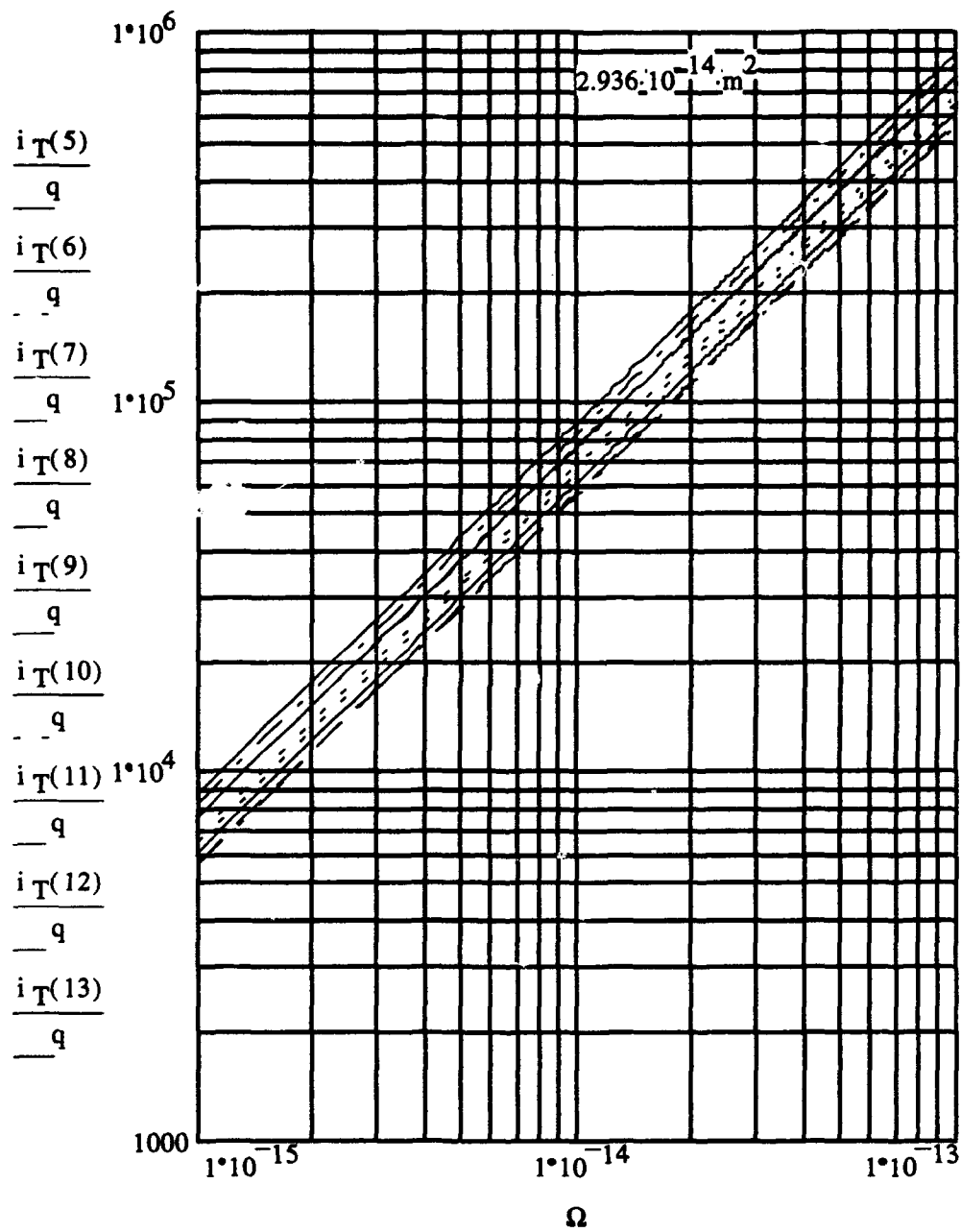


Figure D.3 Case (3), Count Rate  $\frac{i_T}{q}$  (1/s) vs  $\Omega$  ( $\text{rad m}^2$ ) (B), 20 nm

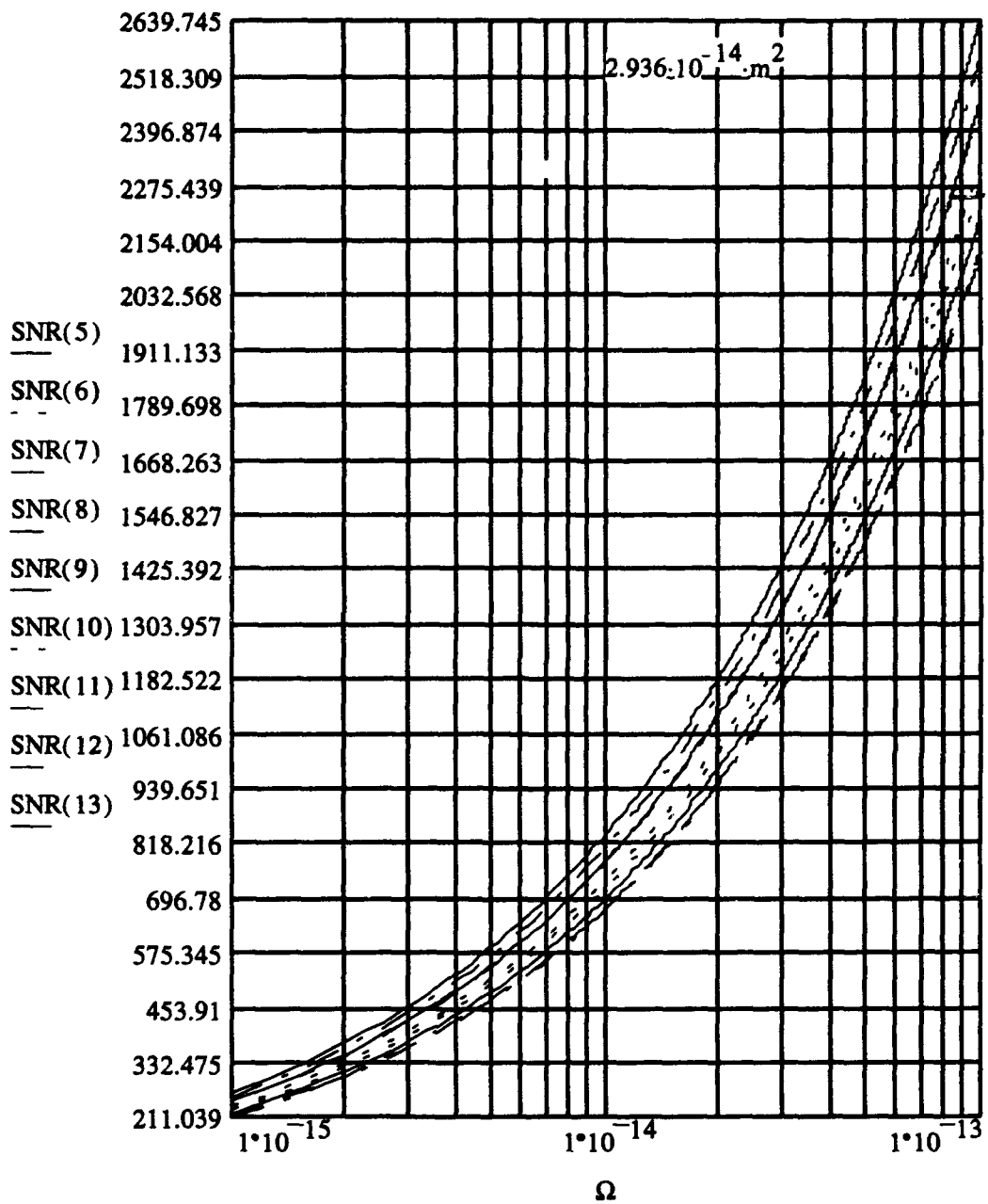


Figure D.4 Case (3), SNR vs  $\Omega$  (rad m<sup>2</sup>) (B), 20 nm

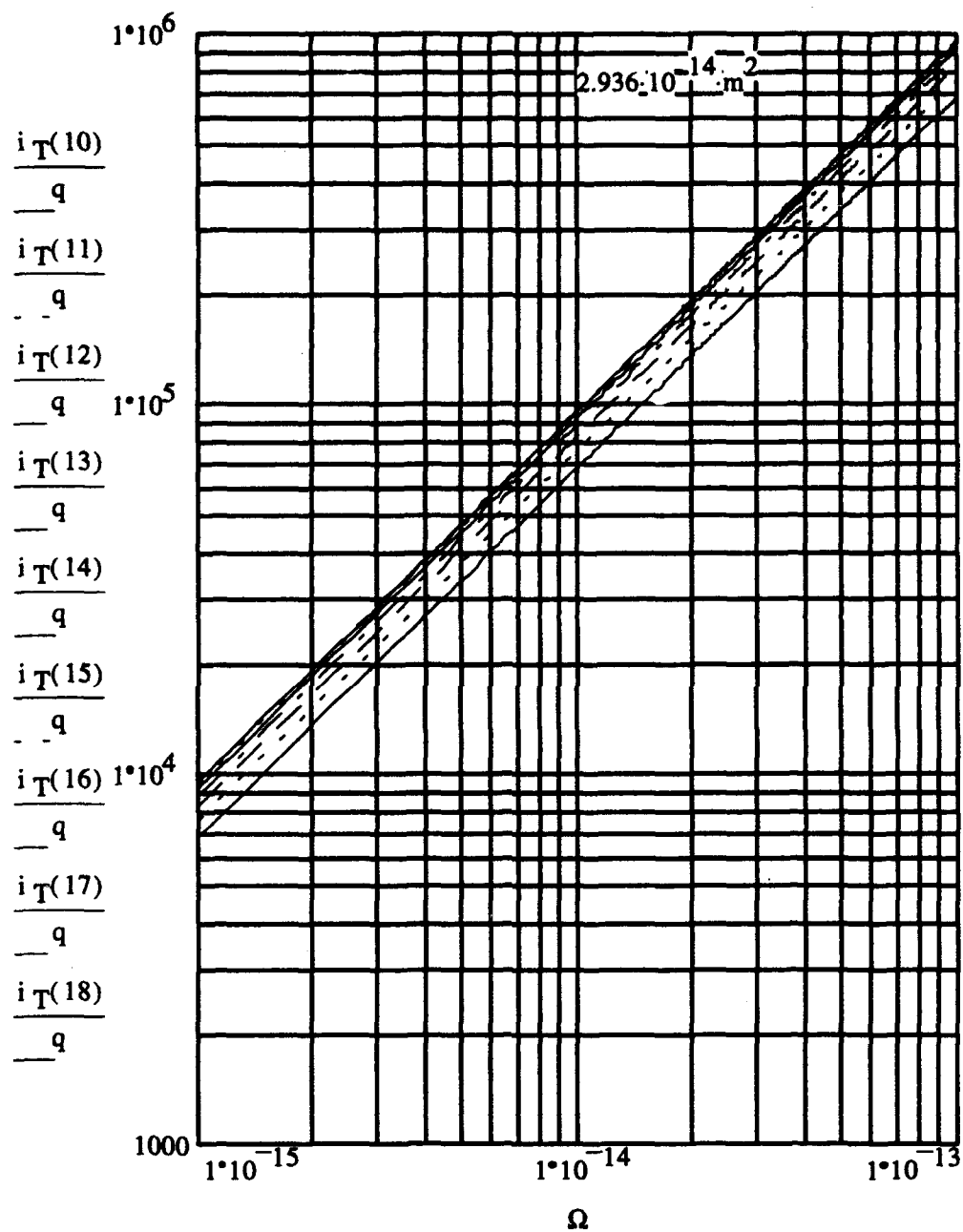


Figure D.5 Case (3), Count Rate  $\frac{i_T}{q}$  (1/s) vs  $\Omega$  (rad m<sup>2</sup>) (V), 20 nm



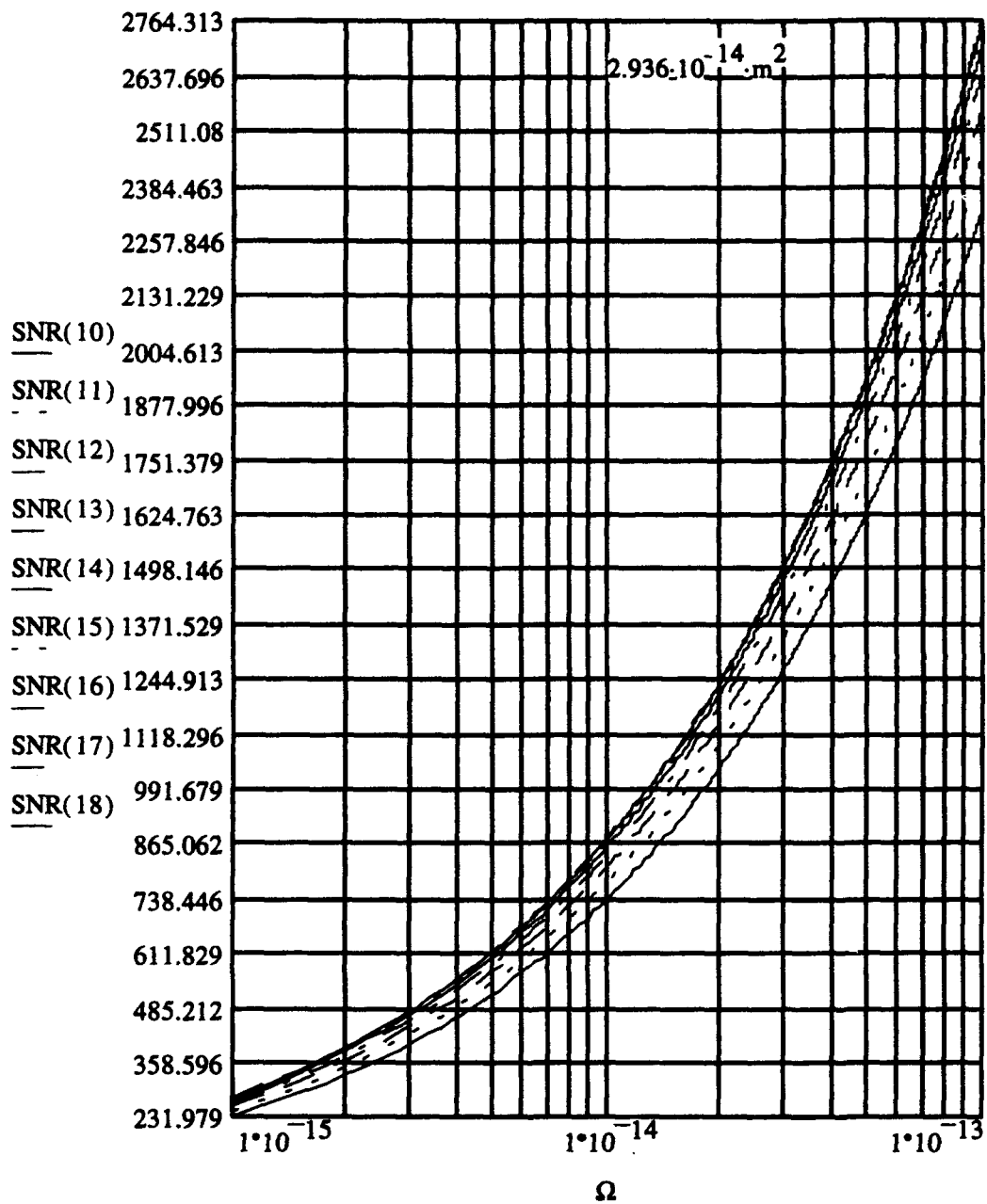


Figure D.6 Case (3), SNR vs  $\Omega$  ( $\text{rad m}^2$ ) (V), 20 nm

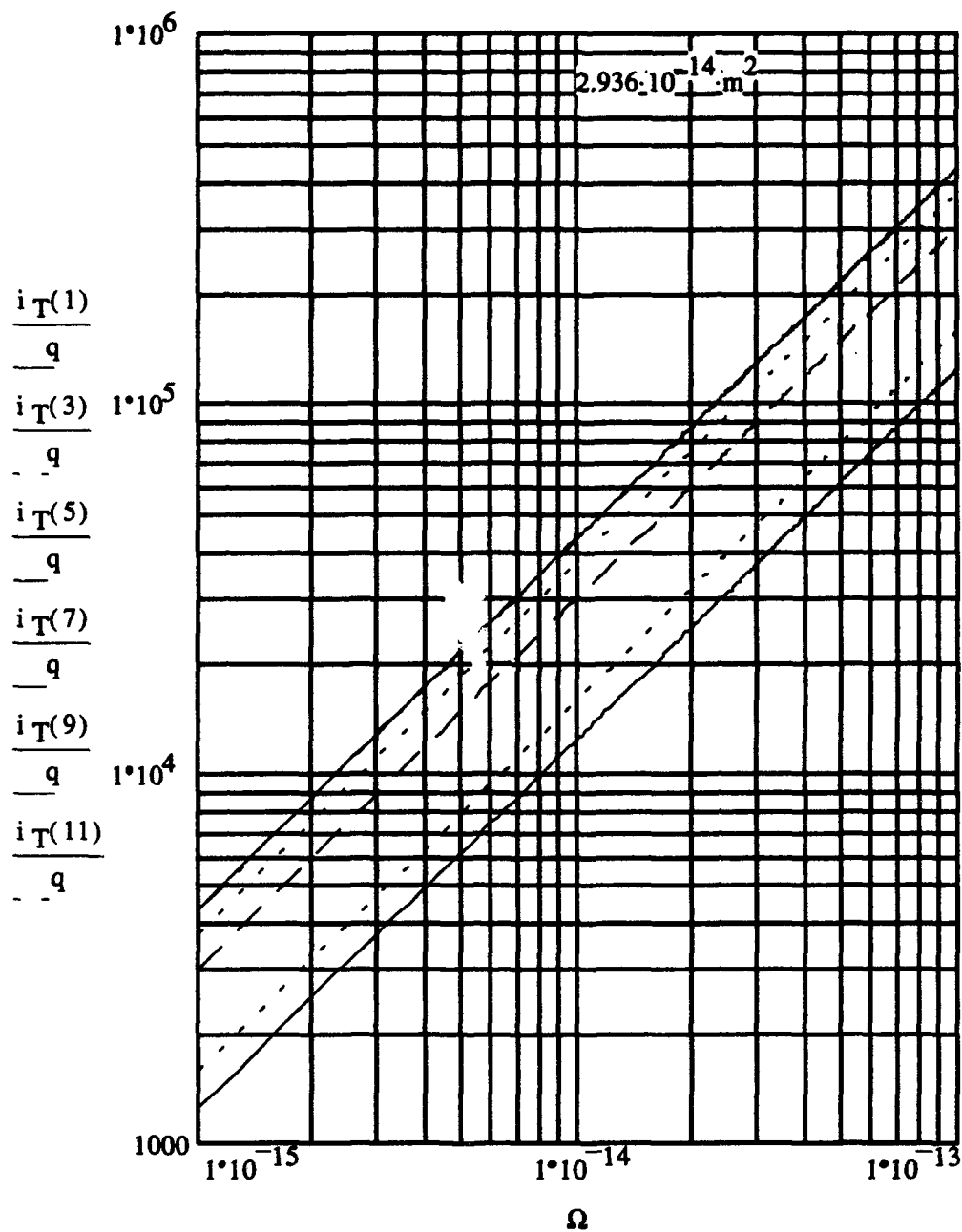


Figure D.7 Case (3), Count Rate  $\frac{i_T}{q}$  (1/s) vs  $\Omega$  ( $\text{rad m}^2$ ) (UV), 10 nm

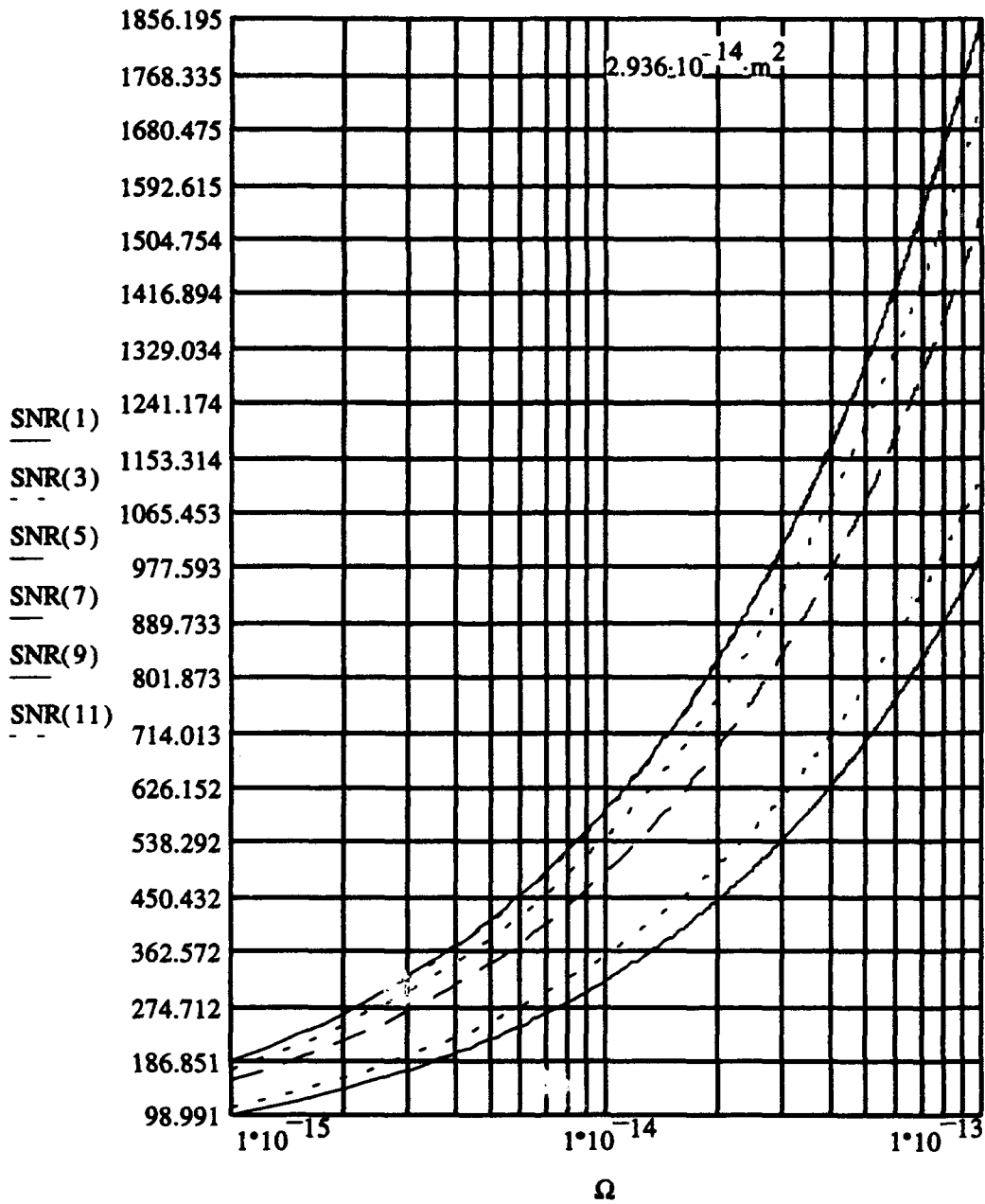


Figure D.8 Case (3), SNR vs  $\Omega$  ( $\text{rad m}^2$ ) (UV), 10 nm

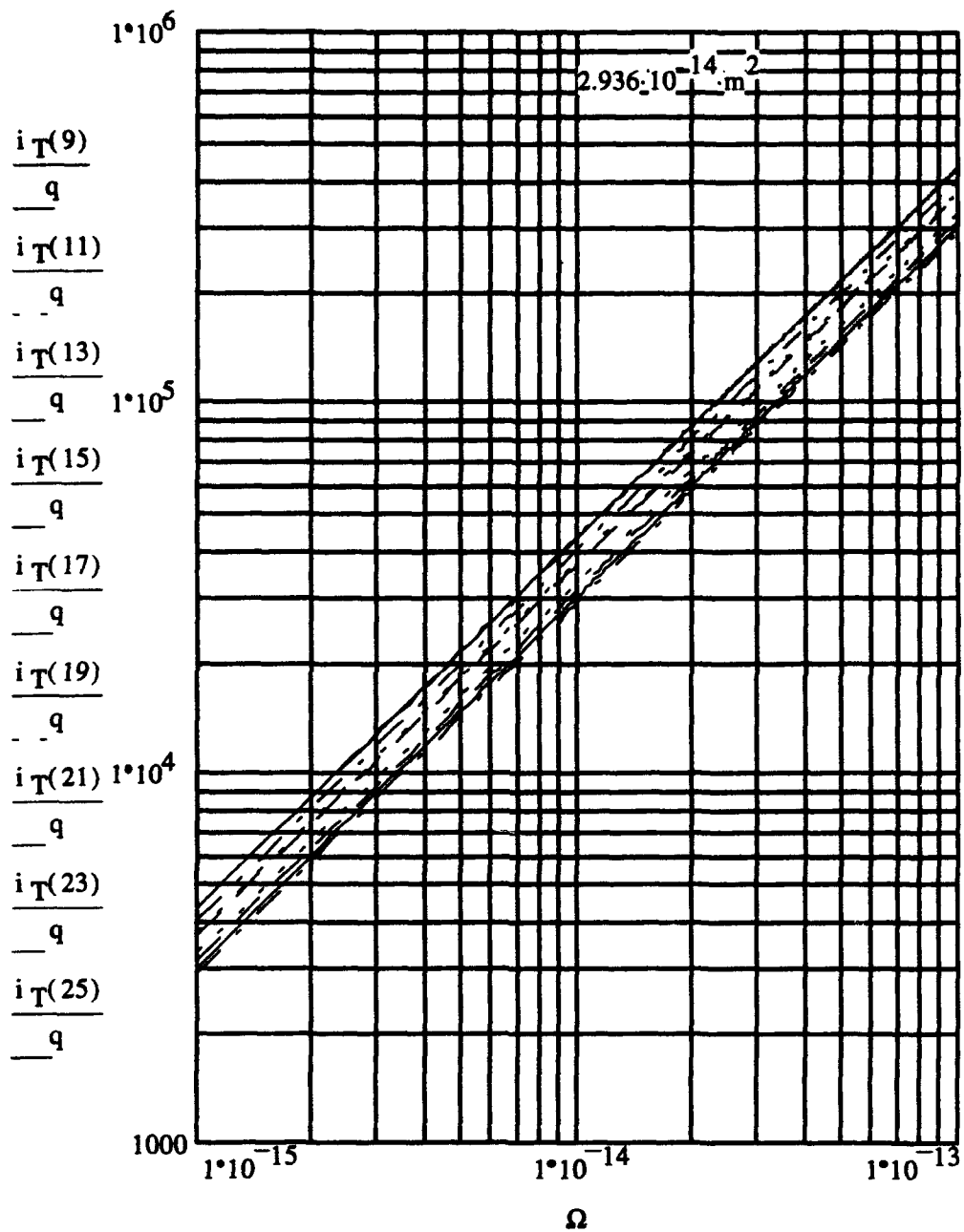


Figure D.9 Case (3), Count Rate  $\frac{i_T}{q}$  (1/s) vs  $\Omega$  ( $\text{rad m}^2$ ) (B), 10 nm

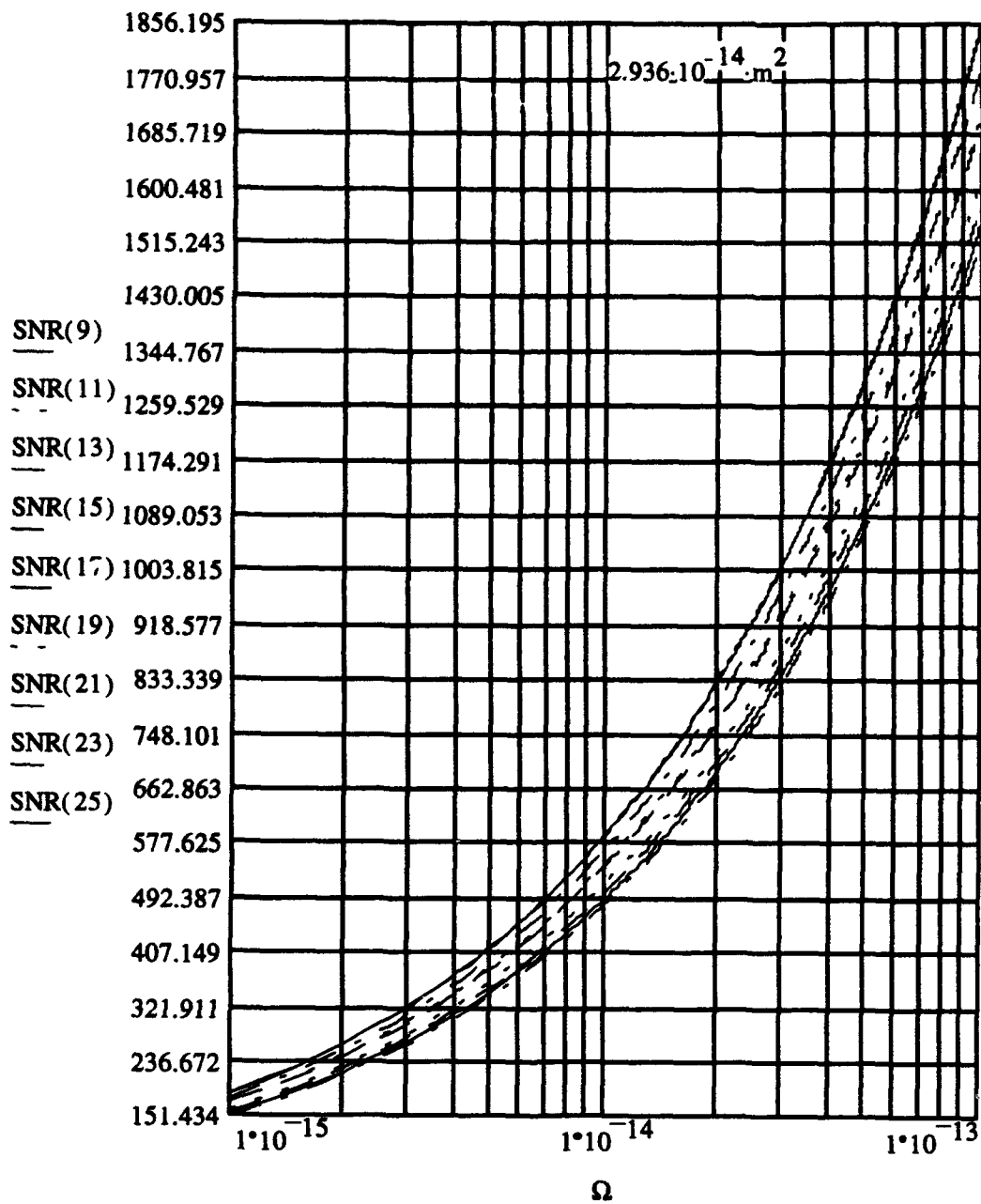


Figure D.10 Case (3), SNR vs  $\Omega$  (radm<sup>2</sup>) (B), 10 nm

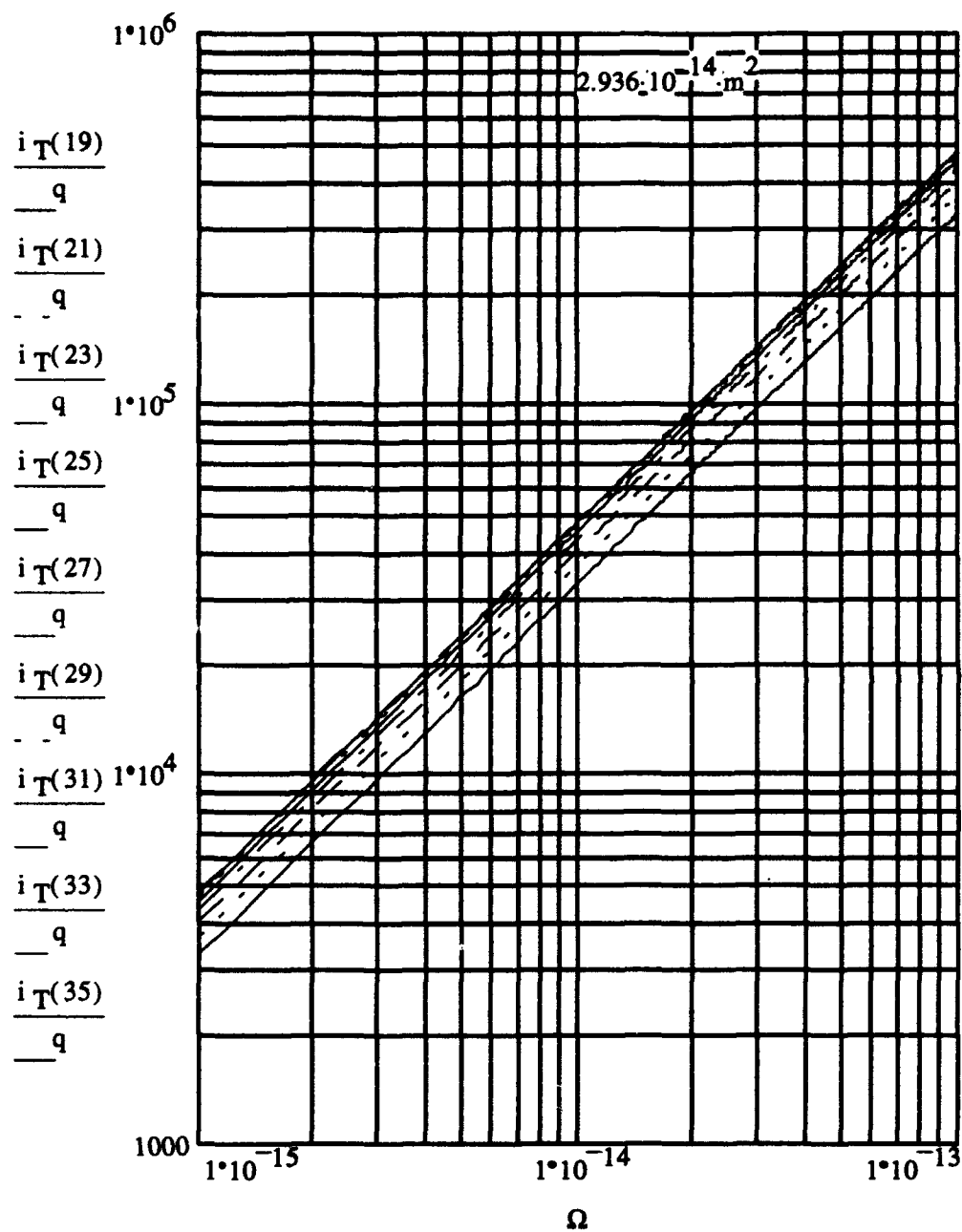


Figure D.11 Case (3), Count Rate  $\frac{i_T}{q}$  (1/s) vs  $\Omega$  ( $\text{rad m}^2$ ) (V), 10 nm

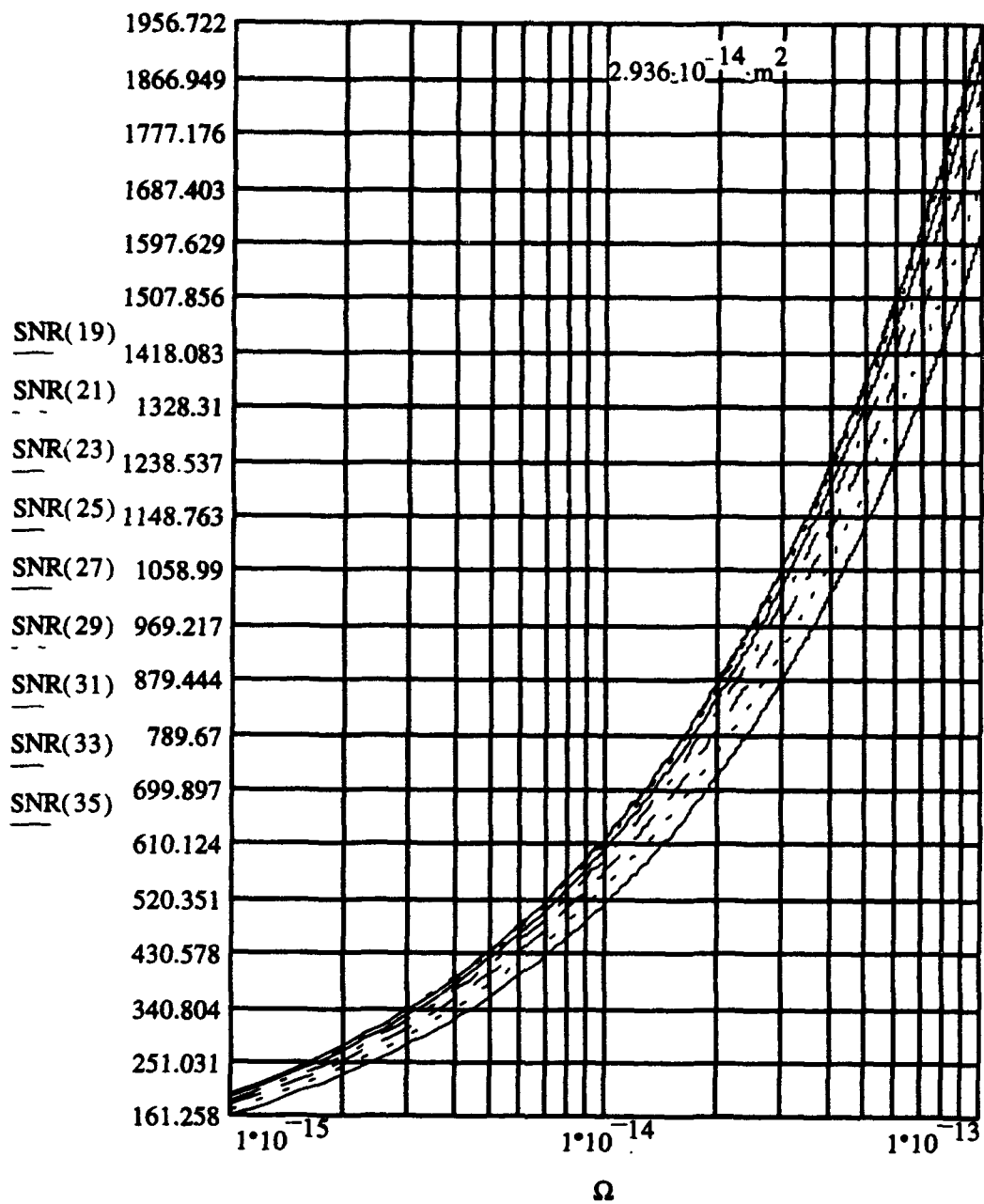


Figure D.12 Case (3), SNR vs  $\Omega$  (rad m<sup>2</sup>) (V), 10 nm

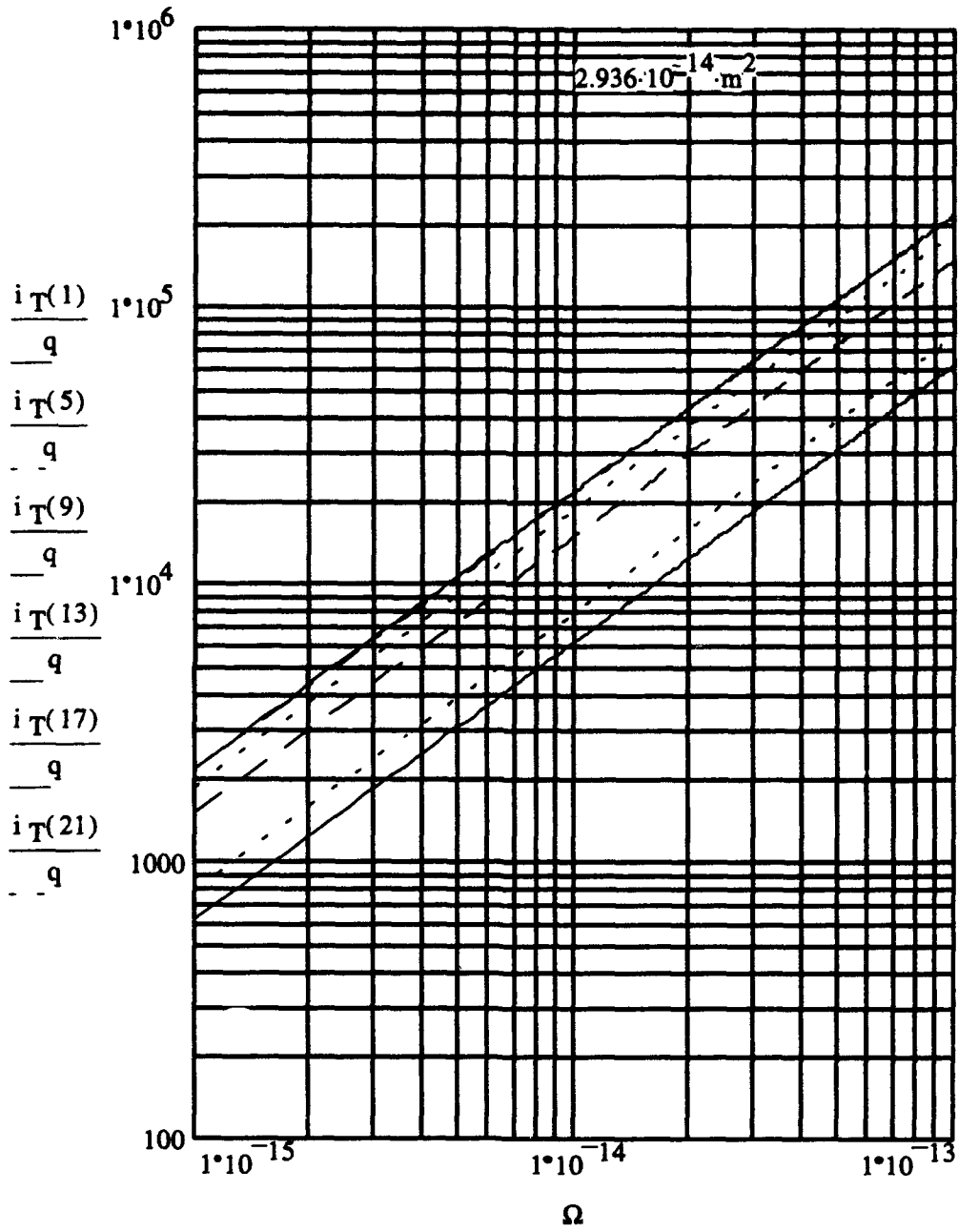


Figure D.13 Case (3), Count Rate  $\frac{i_T}{q}$  (1/s) vs  $\Omega$  ( $\text{rad m}^2$ ) (UV), 5 nm



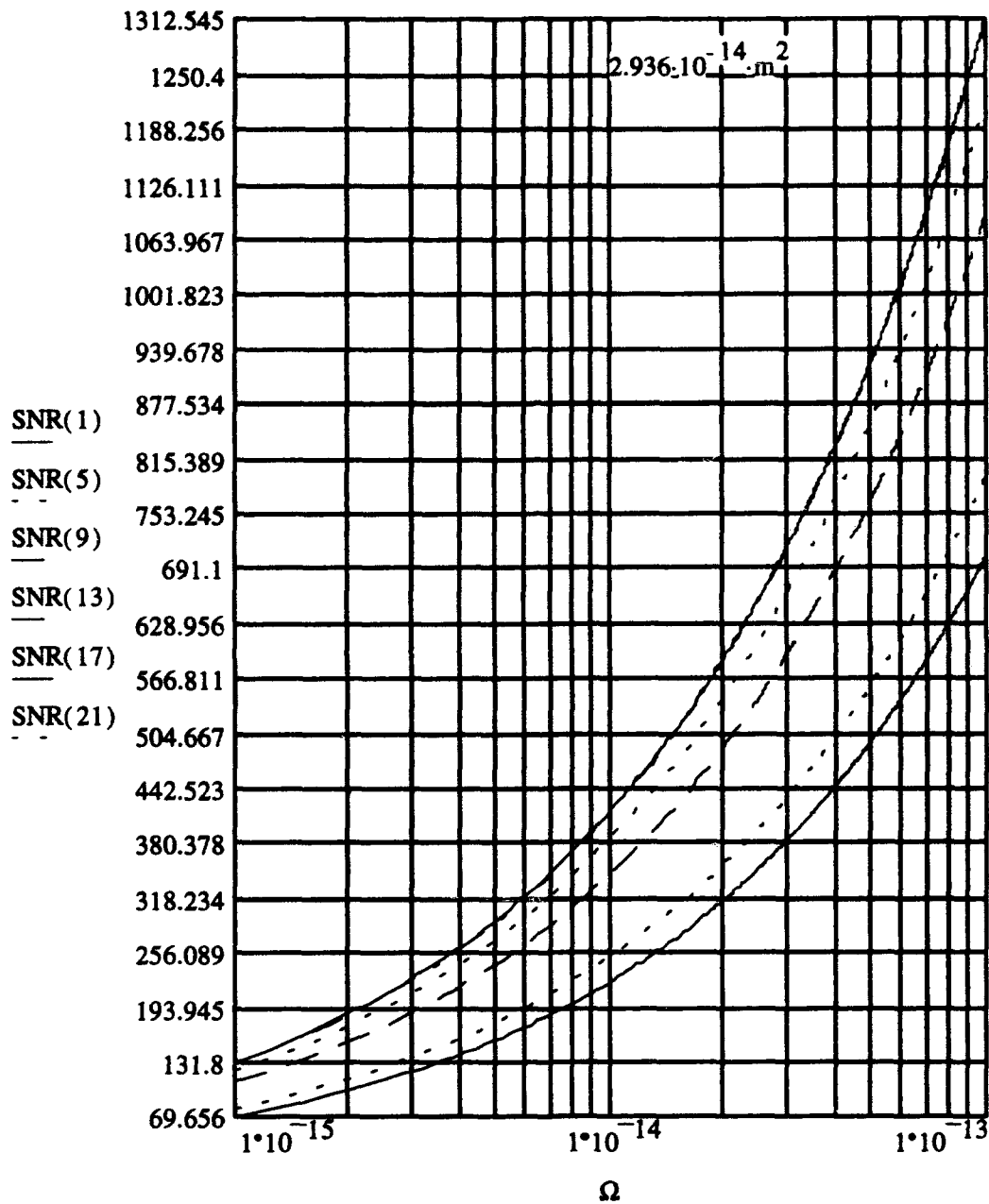


Figure D.14 Case (3), SNR vs  $\Omega$  (radm<sup>2</sup>) (UV), 5 nm

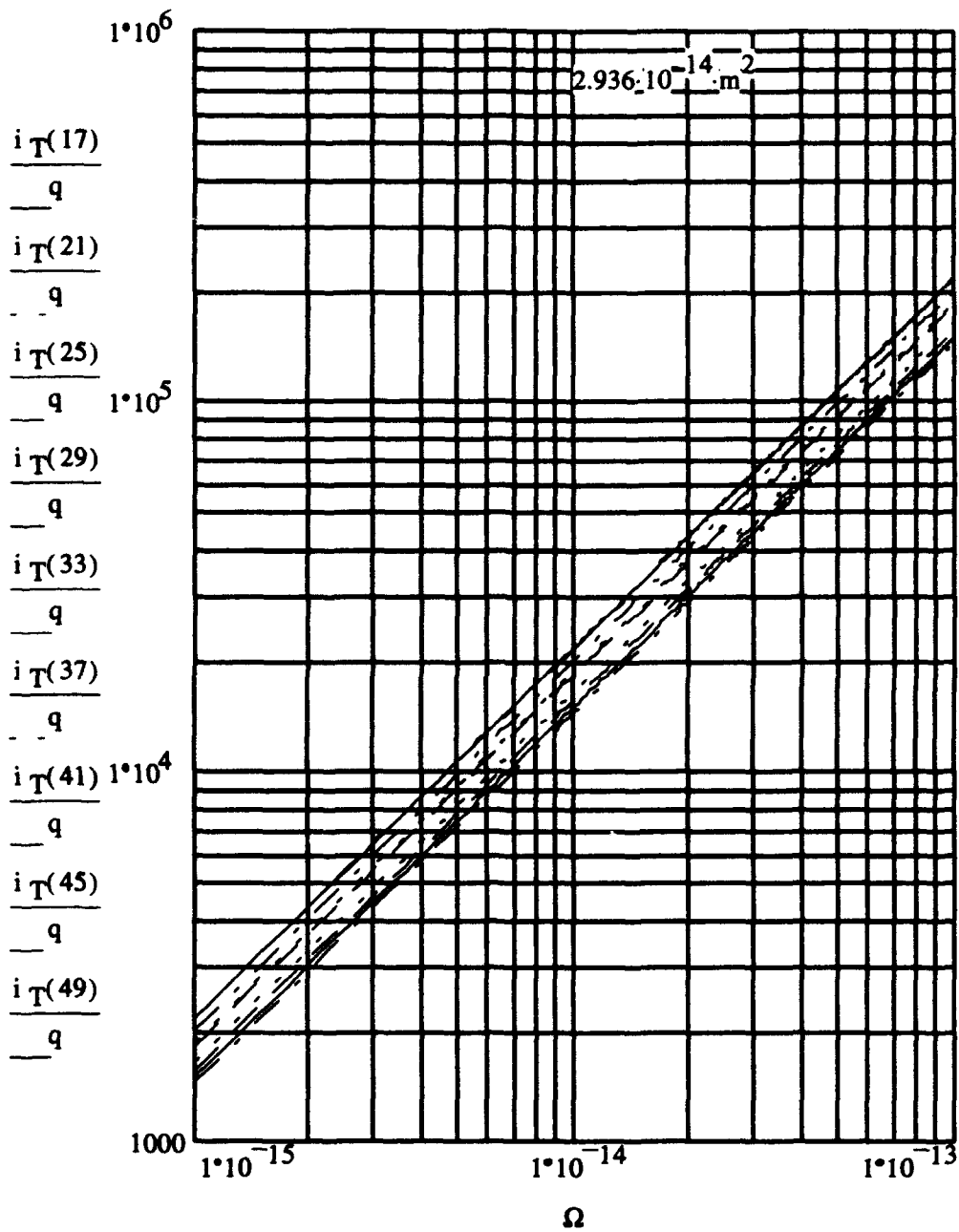


Figure D.15 Case (3), Count Rate  $\frac{i_T}{q}$  (1/s) vs  $\Omega$  ( $\text{rad m}^2$ ) (B), 5 nm

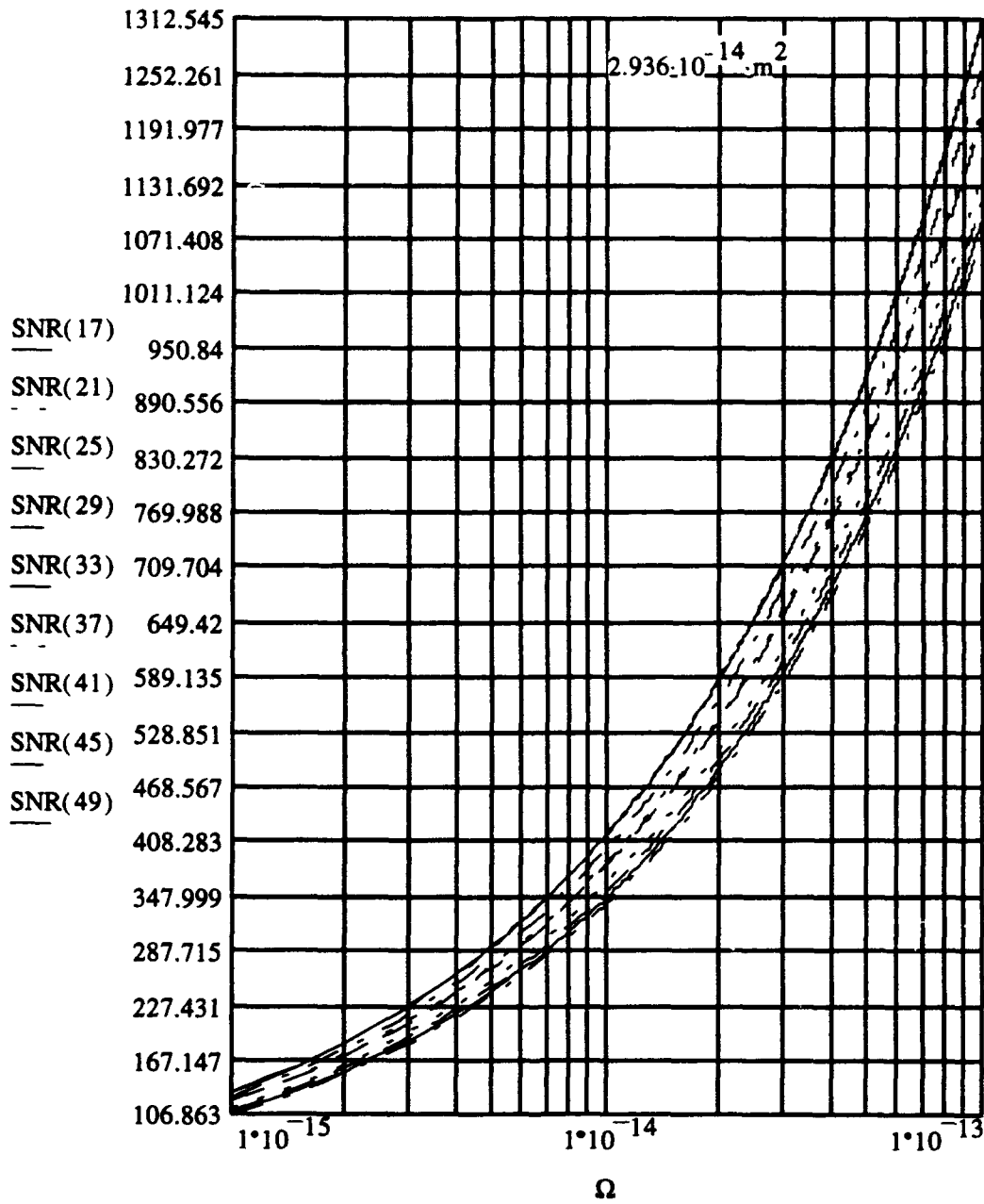


Figure D.16 Case (3), SNR vs  $\Omega$  ( $\text{rad m}^2$ ) (B), 5 nm

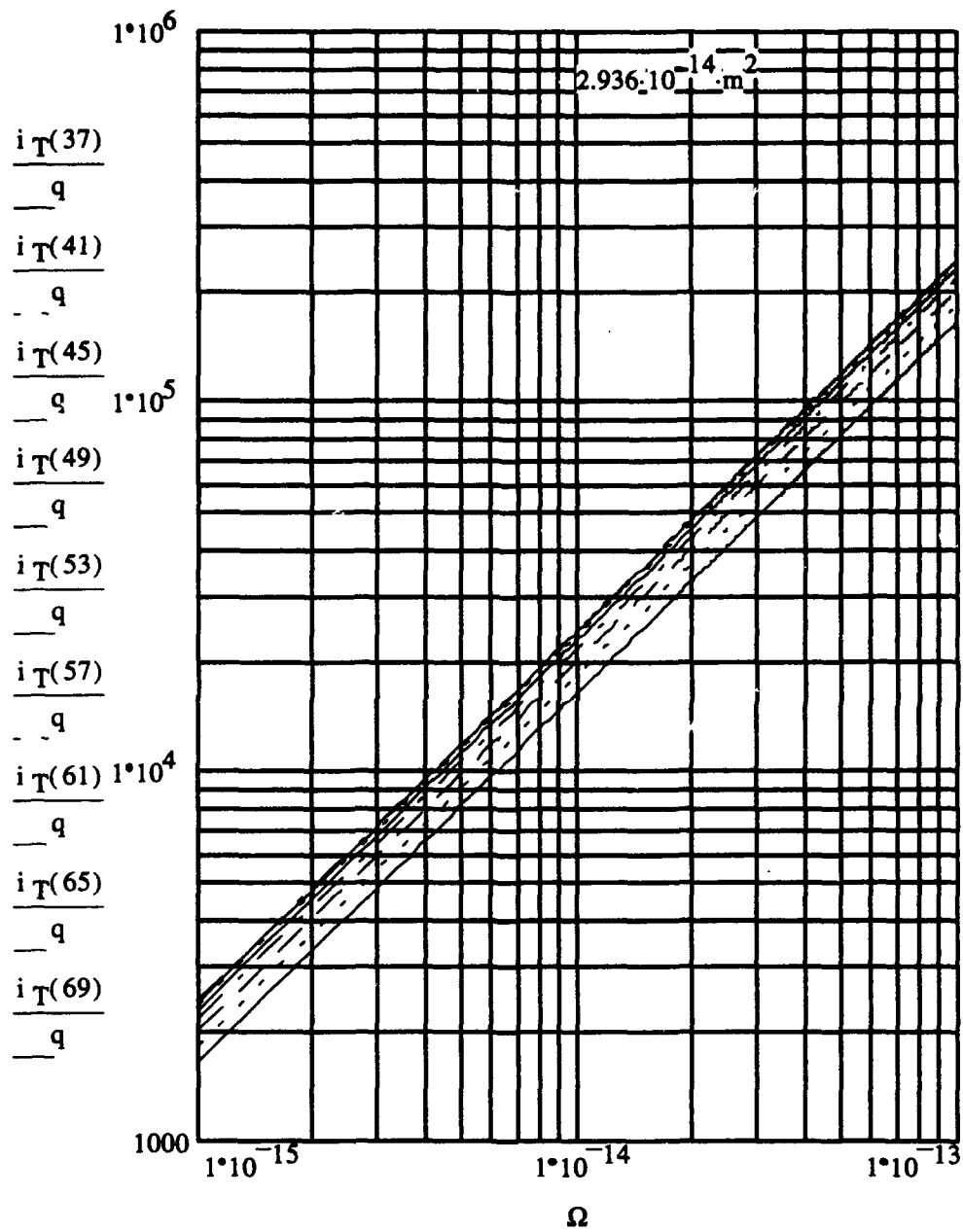


Figure D.17 Case (3), Count Rate  $\frac{i_T}{q}$  (1/s) vs  $\Omega$  (rad m<sup>2</sup>) (V), 5 nm

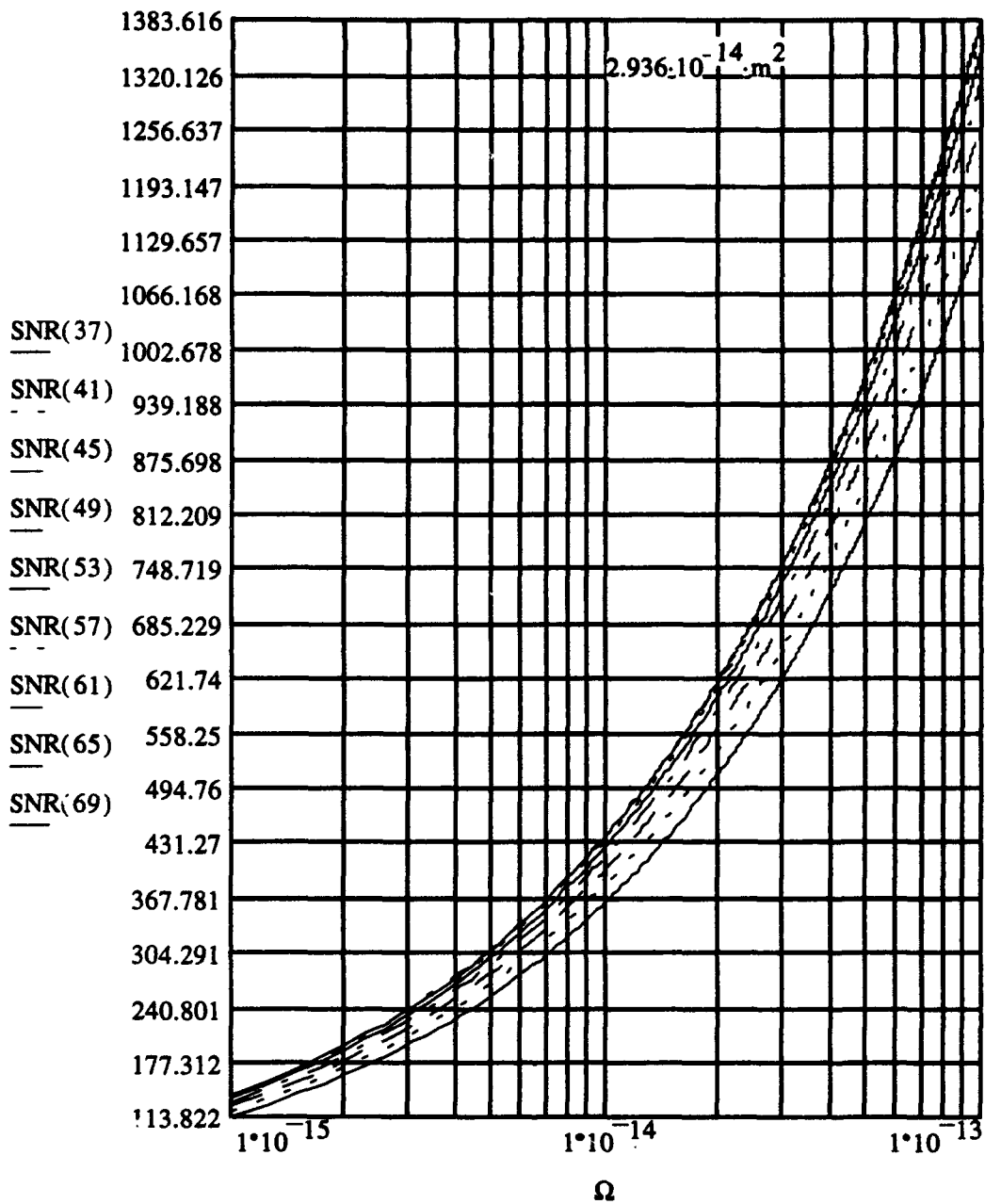


Figure D.18 Case (3), SNR vs  $\Omega$  (rad m<sup>2</sup>) (V), 5 nm

*Appendix E. Case (4): 20 nm, 10 nm and 5 nm Graphs*

*E.1 Legend*

Table E.1 shows the legend for Case (4).

	i			$\bar{\lambda}$ (nm)
	20 nm	10 nm	5 nm	
UV	1	1	1	300
	2	3	5	320
	3	5	9	340
	4	7	13	360
	5	9	17	380
	6	11	21	400
B	5	9	17	380
	6	11	21	400
	7	13	25	420
	8	15	29	440
	9	17	33	460
	10	19	37	480
	11	21	41	500
	12	23	45	520
V	13	25	49	540
	14	27	53	560
	15	29	57	580
	16	31	61	600
	17	33	65	620
	18	35	69	640

Table E.1 Legend, Case (4)

## E.2 20 nm graphs

*E.2.1 Ultraviolet (UV), 300 nm - 400 nm.* Figure E.1 shows the target signal count rate  $i_T/q$  vs  $\Omega$  for Case (4),  $\Delta\lambda = 20$  nm. The vertical dashed line is the reference hypernormalized parameter,  $\Omega_{ref}$ , computed for the target.

Figure E.2 shows the SNR vs  $\Omega$  for Case (4),  $\Delta\lambda = 20$  nm. The vertical dashed line is the reference hypernormalized parameter,  $\Omega_{ref}$ , computed for the target.

*E.2.2 Blue (B), 380 nm - 540 nm.* Figure E.3 shows the target signal count rate  $i_T/q$  vs  $\Omega$  for Case (4),  $\Delta\lambda = 20$  nm. The vertical dashed line is the reference hypernormalized parameter,  $\Omega_{ref}$ , computed for the target.

Figure E.4 shows the SNR vs  $\Omega$  for Case (4),  $\Delta\lambda = 20$  nm. The vertical dashed line is the reference hypernormalized parameter,  $\Omega_{ref}$ , computed for the target.

*E.2.3 Visible (V), 480 nm - 650 nm.* Figure E.5 shows the target signal count rate  $i_T/q$  vs  $\Omega$  for Case (4),  $\Delta\lambda = 20$  nm. The vertical dashed line is the reference hypernormalized parameter,  $\Omega_{ref}$ , computed for the target.

Figure E.6 shows the SNR vs  $\Omega$  for Case (4),  $\Delta\lambda = 20$  nm. The vertical dashed line is the reference hypernormalized parameter,  $\Omega_{ref}$ , computed for the target.

## E.3 10 nm graphs

*E.3.1 Ultraviolet (UV), 300 nm - 400 nm.* Figure E.7 shows the target signal count rate  $i_T/q$  vs  $\Omega$  for Case (4),  $\Delta\lambda = 10$  nm. The vertical dashed line is the reference hypernormalized parameter,  $\Omega_{ref}$ , computed for the target.

Figure E.8 shows the SNR vs  $\Omega$  for Case (4),  $\Delta\lambda = 10$  nm. The vertical dashed line is the reference hypernormalized parameter,  $\Omega_{ref}$ , computed for the target.

*E.3.2 Blue (B), 380 nm - 540 nm.* Figure E.9 shows the target signal count rate  $i_T/q$  vs  $\Omega$  for Case (4),  $\Delta\lambda = 10$  nm. The vertical dashed line is the reference hypernormalized parameter,  $\Omega_{ref}$ , computed for the target.

Figure E.10 shows the SNR vs  $\Omega$  for Case (4),  $\Delta\lambda = 10$  nm. The vertical dashed line is the reference hypernormalized parameter,  $\Omega_{ref}$ , computed for the target.

*E.3.3 Visible (V), 480 nm - 650 nm.* Figure E.11 shows the target signal count rate  $i_T/q$  vs  $\Omega$  for Case (4),  $\Delta\lambda = 10$  nm. The vertical dashed line is the reference hypernormalized parameter,  $\Omega_{ref}$ , computed for the target.

Figure E.12 shows the SNR vs  $\Omega$  for Case (4),  $\Delta\lambda = 10$  nm. The vertical dashed line is the reference hypernormalized parameter,  $\Omega_{ref}$ , computed for the target.

#### *E.4 5 nm graphs*

*E.4.1 Ultraviolet (UV), 300 nm - 400 nm.* Figure E.13 shows the target signal count rate  $i_T/q$  vs  $\Omega$  for Case (4),  $\Delta\lambda = 5$  nm. The vertical dashed line is the reference hypernormalized parameter,  $\Omega_{ref}$ , computed for the target.

Figure E.14 shows the SNR vs  $\Omega$  for Case (4),  $\Delta\lambda = 5$  nm. The vertical dashed line is the reference hypernormalized parameter,  $\Omega_{ref}$ , computed for the target.

*E.4.2 Blue (B), 380 nm - 540 nm.* Figure E.15 shows the target signal count rate  $i_T/q$  vs  $\Omega$  for Case (4),  $\Delta\lambda = 5$  nm. The vertical dashed line is the reference hypernormalized parameter,  $\Omega_{ref}$ , computed for the target.

Figure E.16 shows the SNR vs  $\Omega$  for Case (4),  $\Delta\lambda = 5$  nm. The vertical dashed line is the reference hypernormalized parameter,  $\Omega_{ref}$ , computed for the target.



*E.4.3 Visible (V), 480 nm - 650 nm.* Figure E.17 shows the target signal count rate  $i_T/q$  vs  $\Omega$  for Case (4),  $\Delta\lambda = 5$  nm. The vertical dashed line is the reference hypernormalized parameter,  $\Omega_{ref}$ , computed for the target.

Figure E.18 shows the SNR vs  $\Omega$  for Case (4),  $\Delta\lambda = 5$  nm. The vertical dashed line is the reference hypernormalized parameter,  $\Omega_{ref}$ , computed for the target.

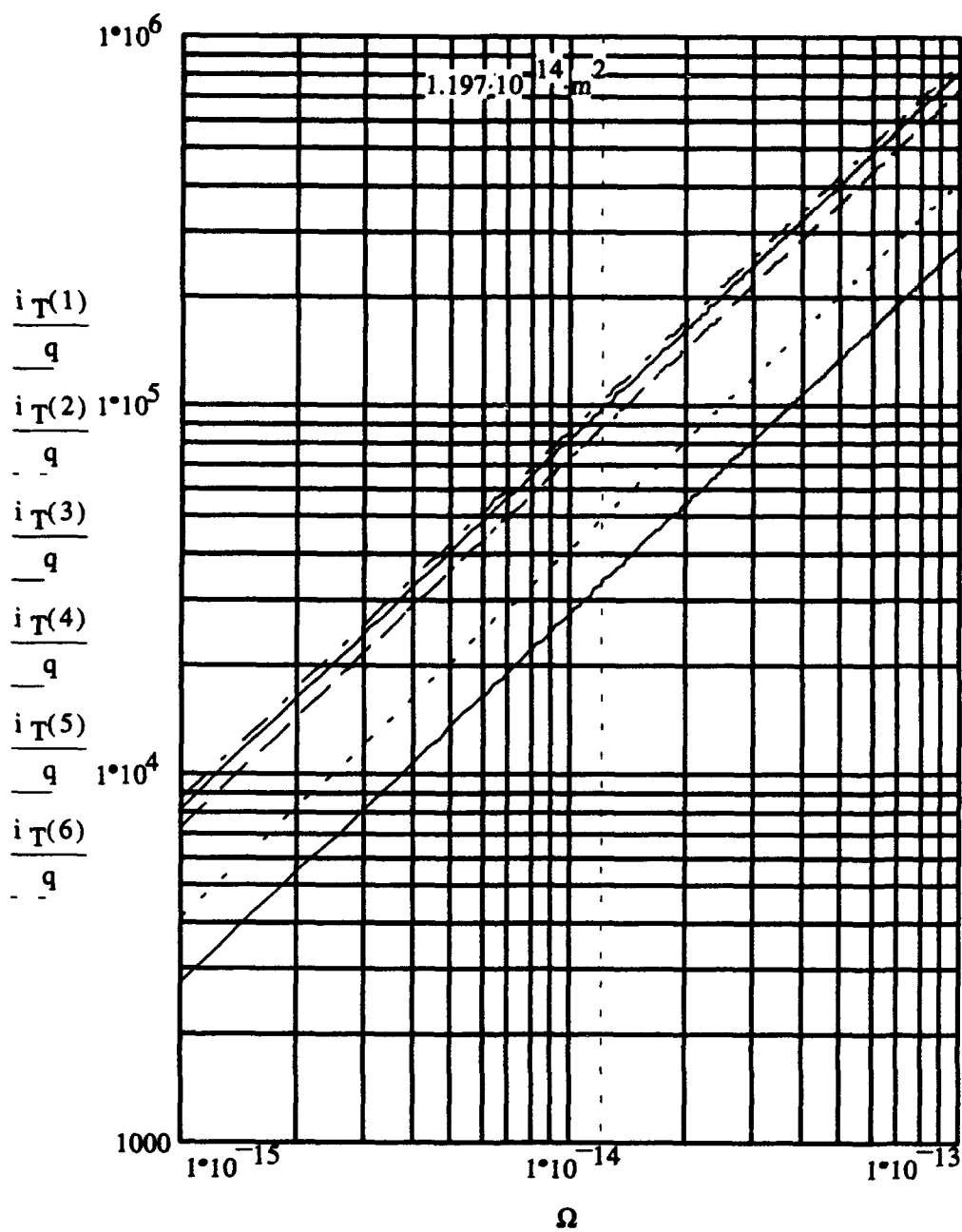


Figure E.1 Case (4), Count Rate  $\frac{i_T}{q}$  (1/s) vs  $\Omega$  ( $\text{rad m}^2$ ) (UV), 20 nm

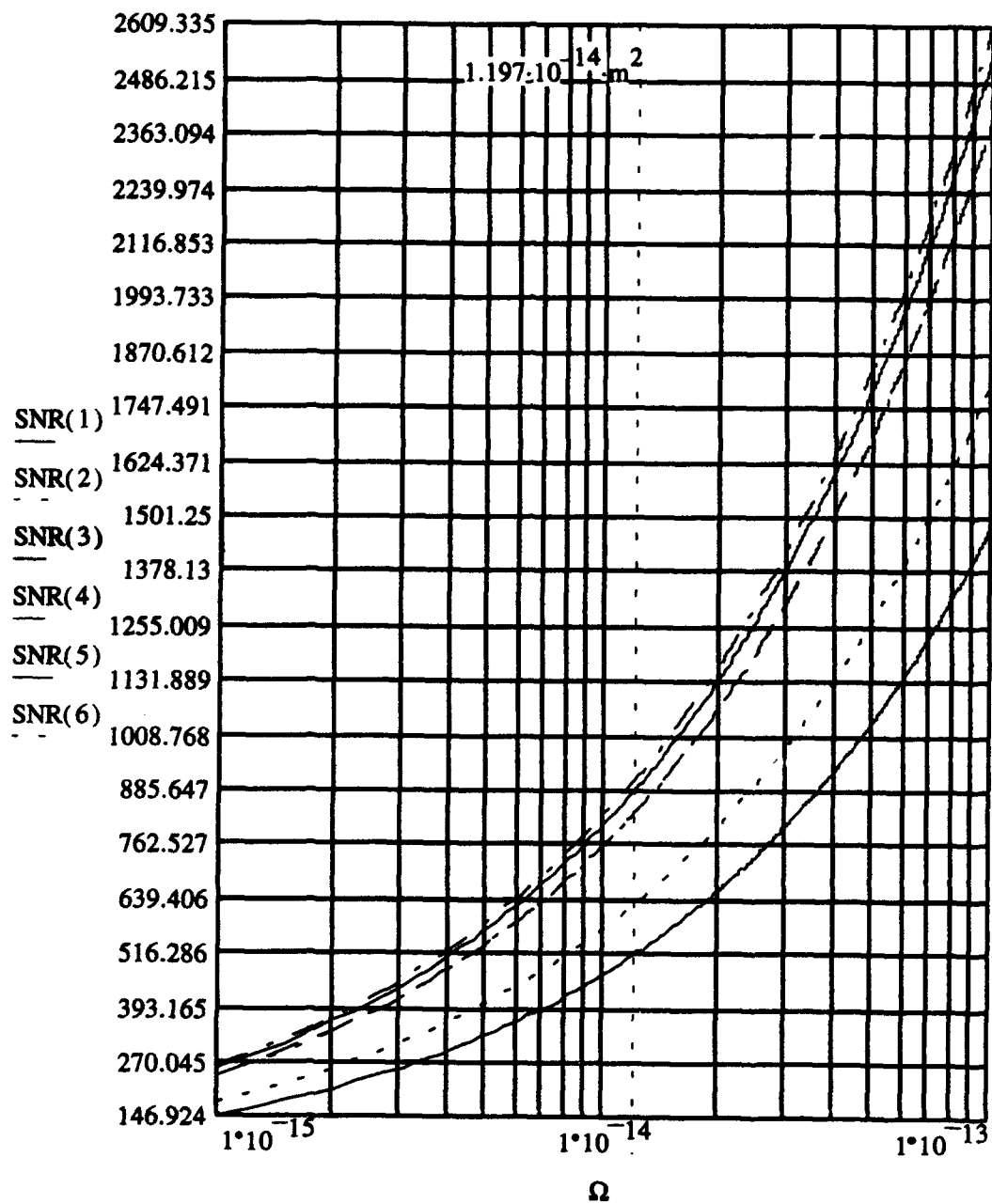


Figure E.2 Case (4), SNR vs  $\Omega$  (rad m<sup>2</sup>) (UV), 20 nm

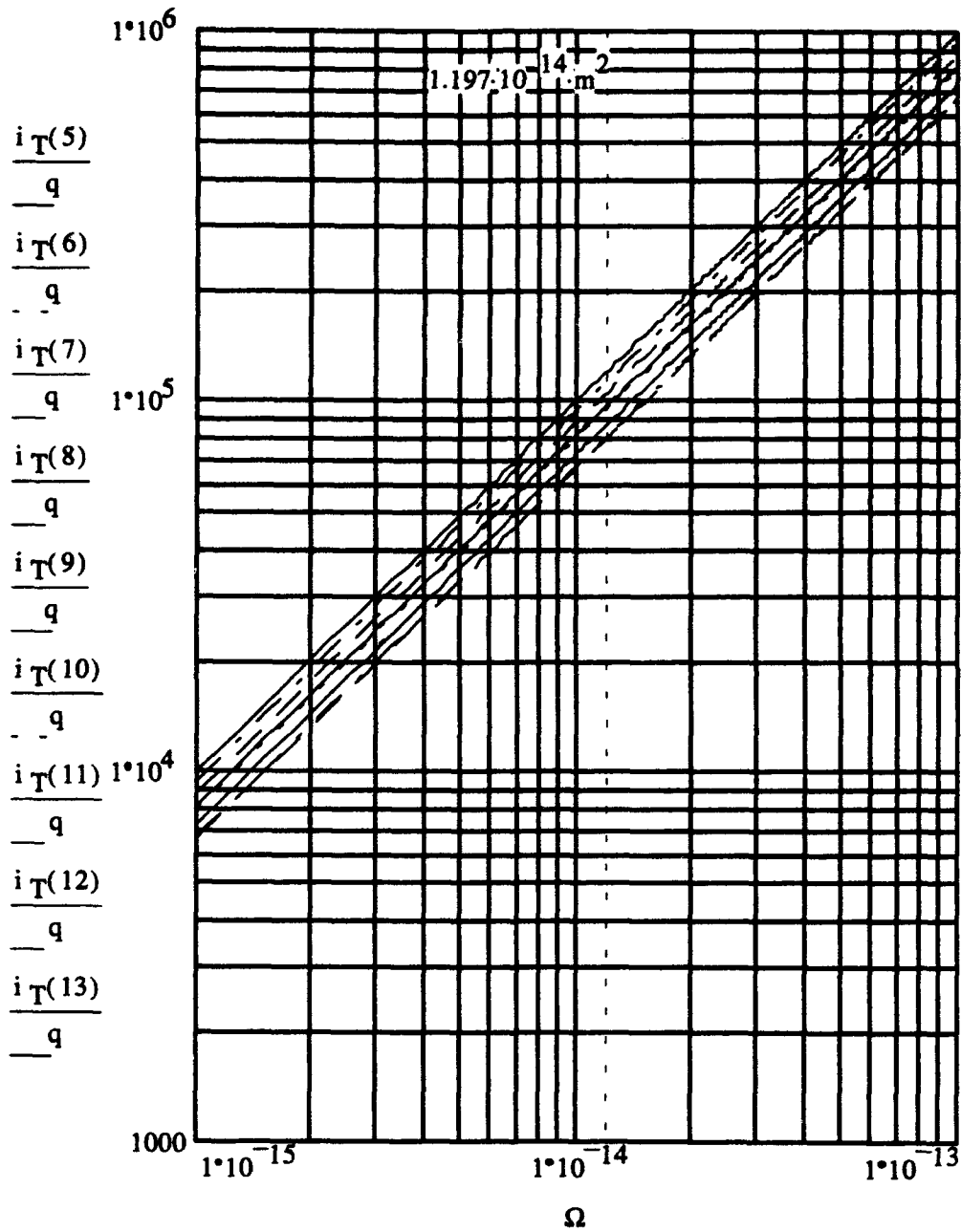


Figure E.3 Case (4), Count Rate  $\frac{i_T}{q}$  (1/s) vs  $\Omega$  ( $\text{rad m}^2$ ) (B), 20 nm

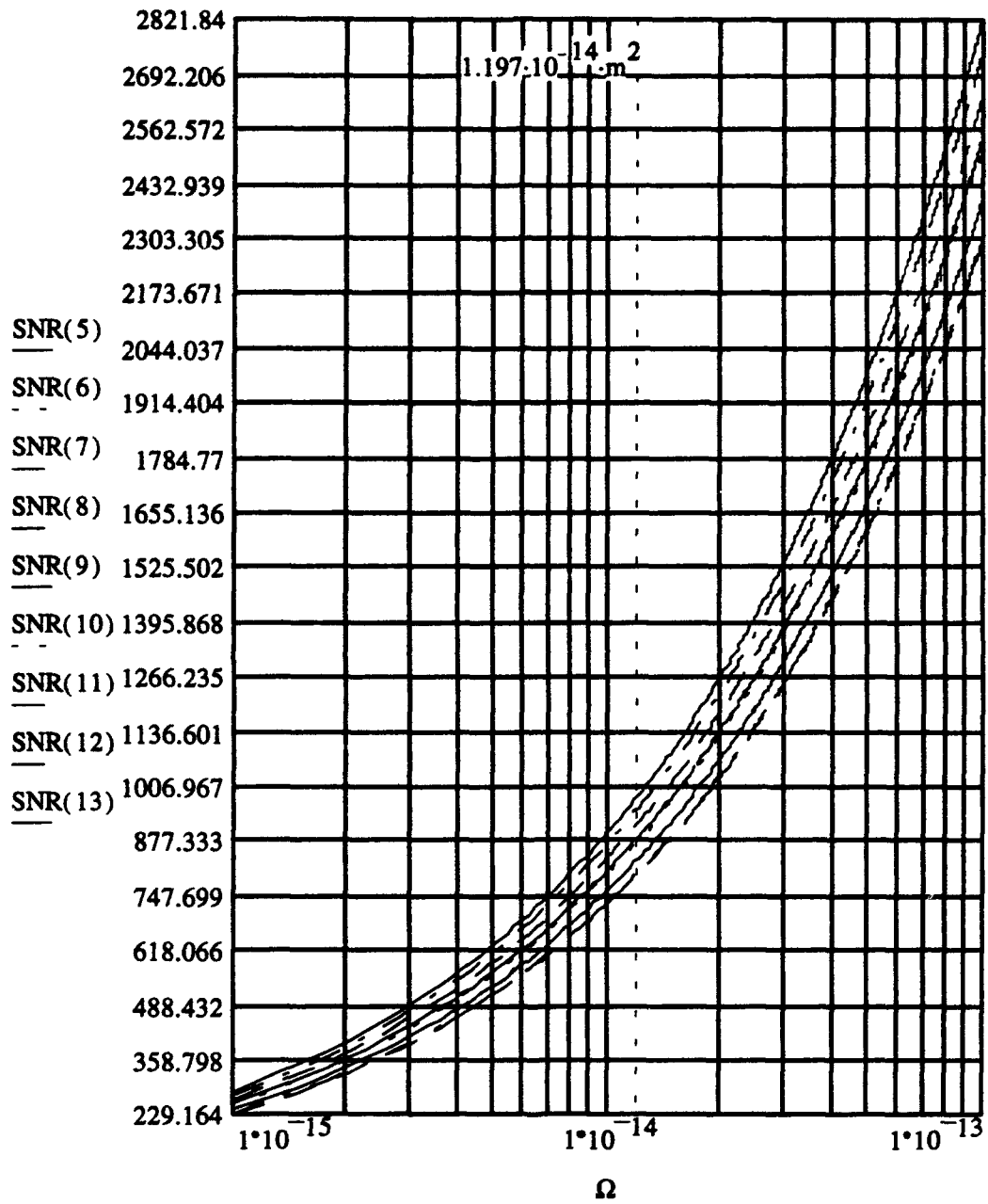


Figure E.4 Case (4), SNR vs  $\Omega$  ( $rad m^2$ ) (B), 20 nm

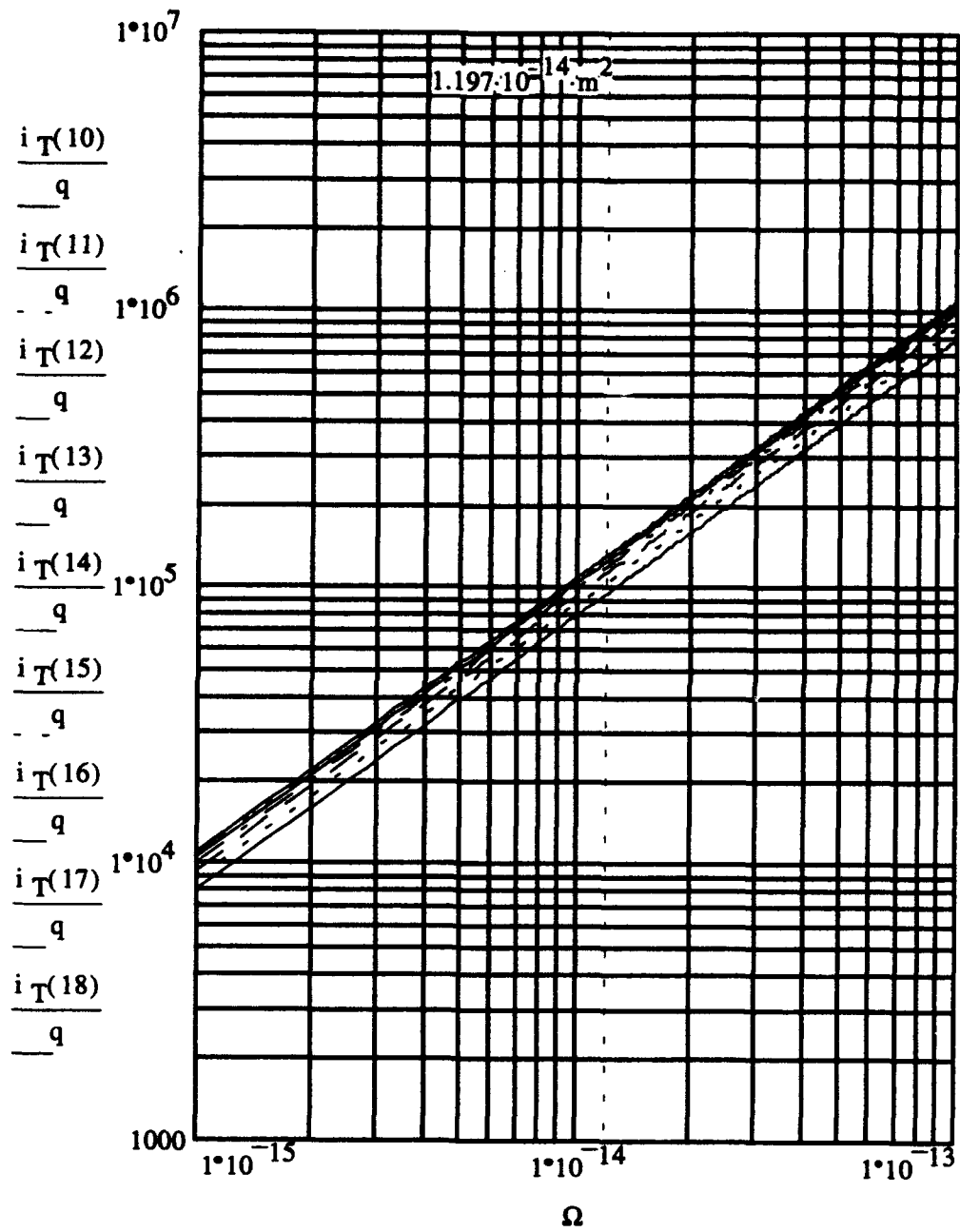


Figure E.5 Case (4), Count Rate  $\frac{i_T}{q}$  (1/s) vs  $\Omega$  (rad m<sup>2</sup>) (V), 20 nm

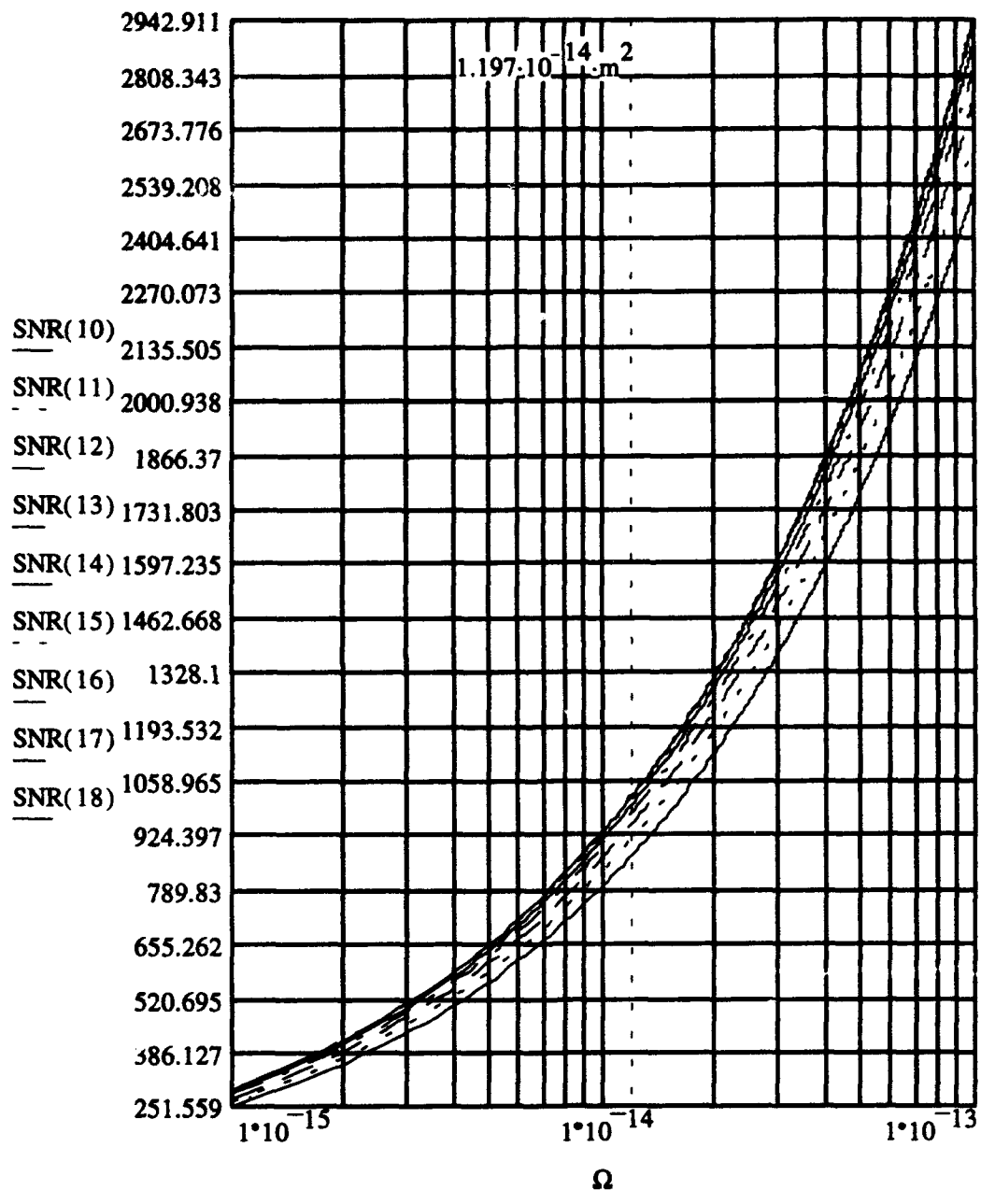


Figure E.6 Case (4), SNR vs  $\Omega$  ( $\text{rad m}^2$ ) (V), 20 nm

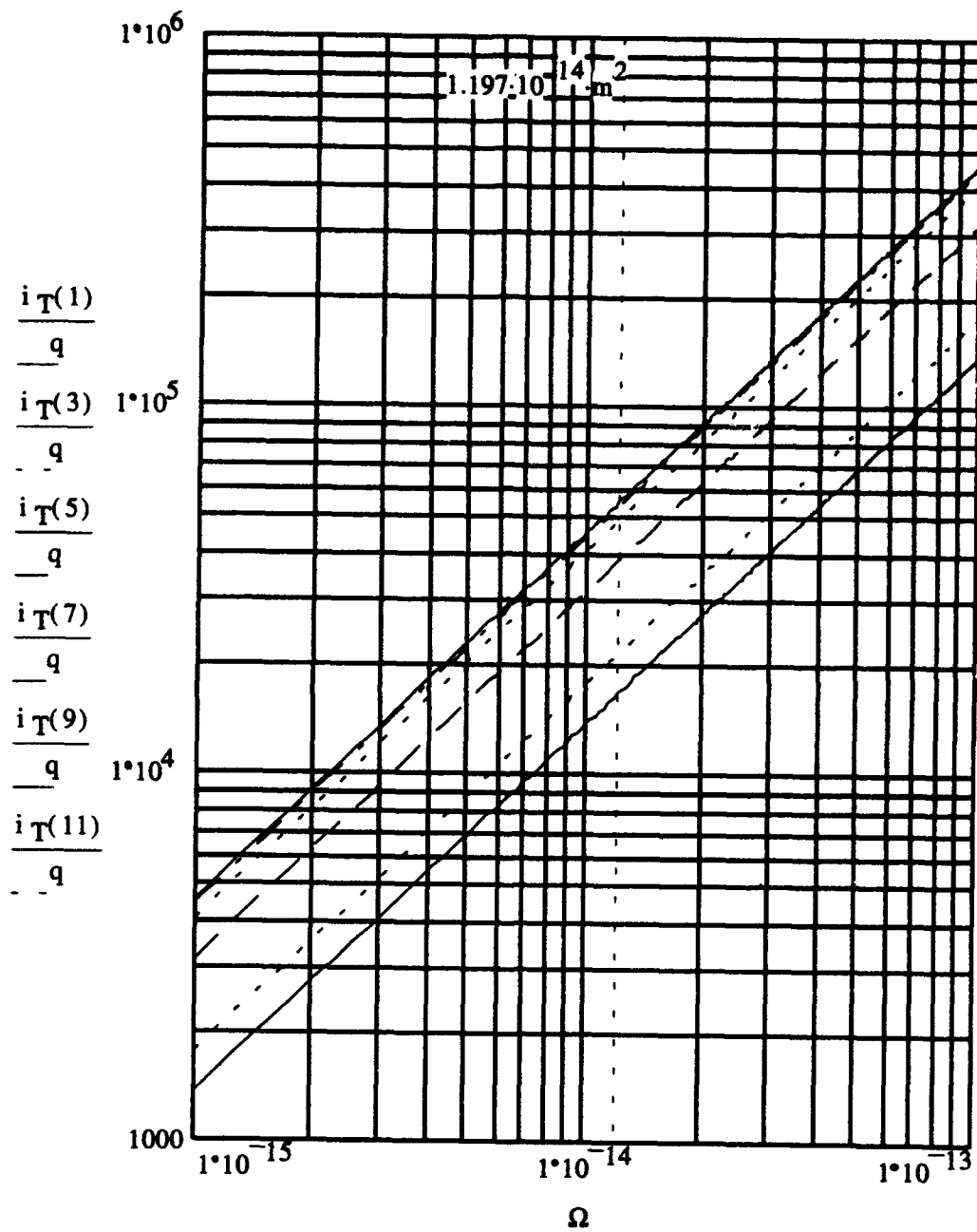


Figure E.7 Case (4), Count Rate  $\frac{i_T}{q}$  (1/s) vs  $\Omega$  (radm<sup>2</sup>) (UV), 10 nm



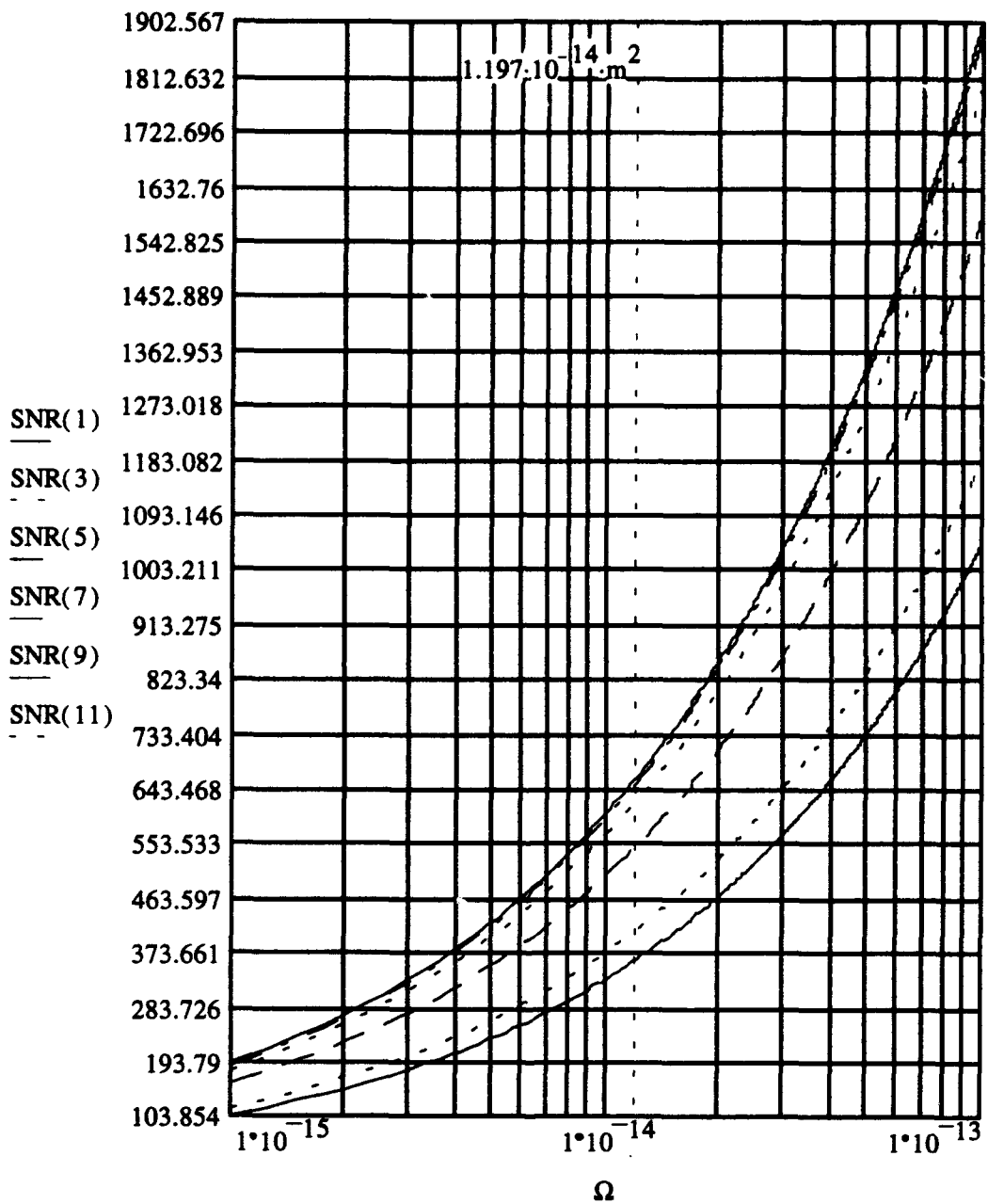


Figure E.8 Case (4), SNR vs  $\Omega$  ( $rad m^2$ ) (UV), 10 nm

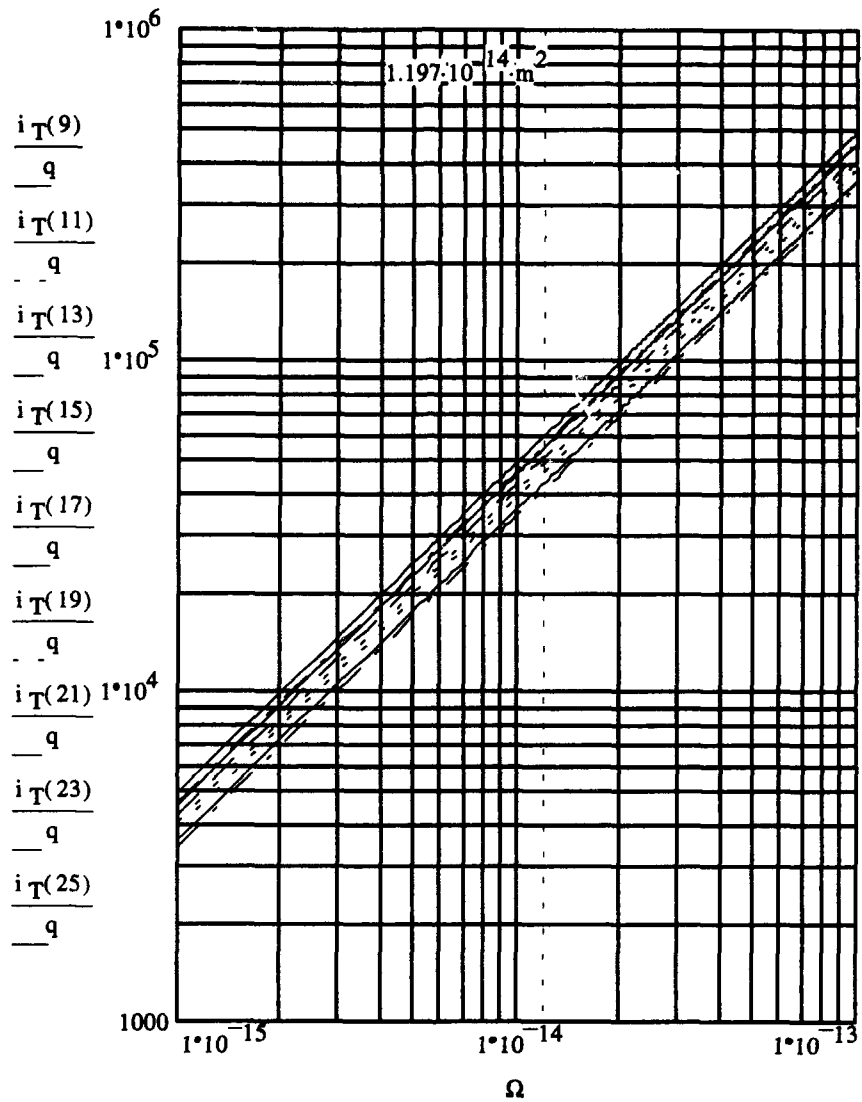


Figure E.9 Case (4), Count Rate  $\frac{i_T}{q}$  (1/s) vs  $\Omega$  ( $\text{rad m}^2$ ) (B), 10 nm

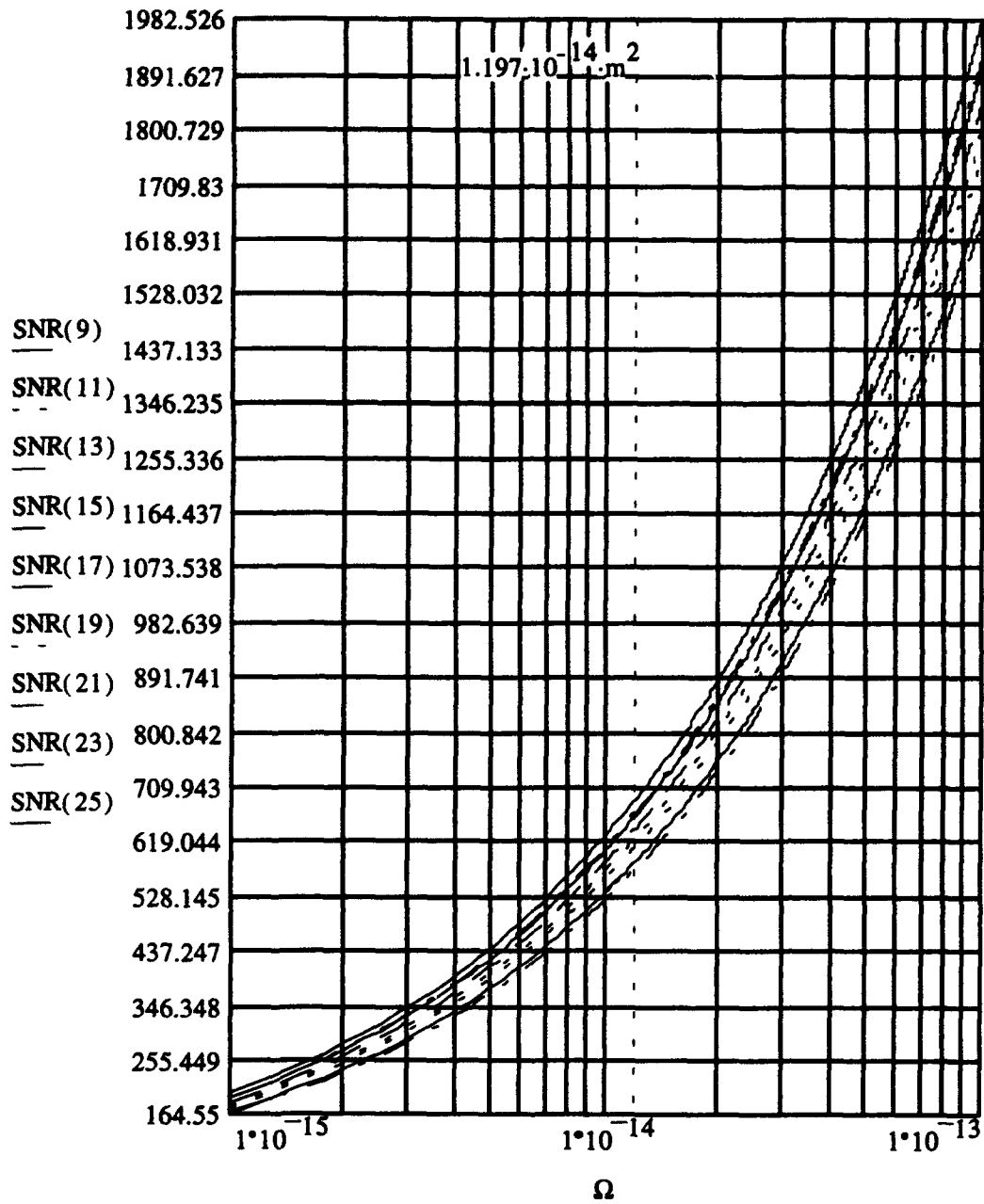


Figure E.10 Case (4), SNR vs  $\Omega$  ( $rad\ m^2$ ) (B), 10 nm

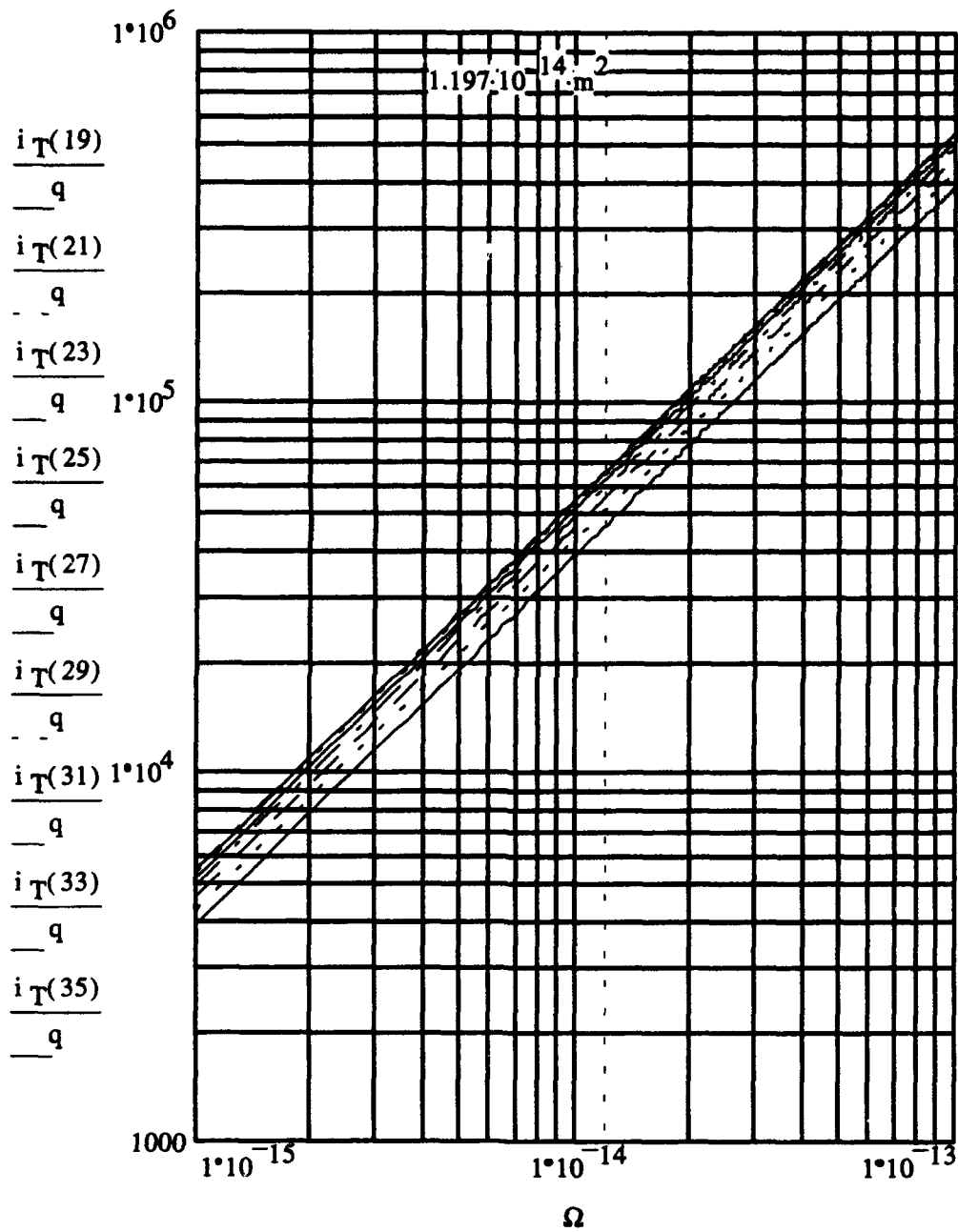


Figure E.11 Case (4), Count Rate  $\frac{i_T}{q}$  (1/s) vs  $\Omega$  ( $\text{rad m}^2$ ) (V), 10 nm

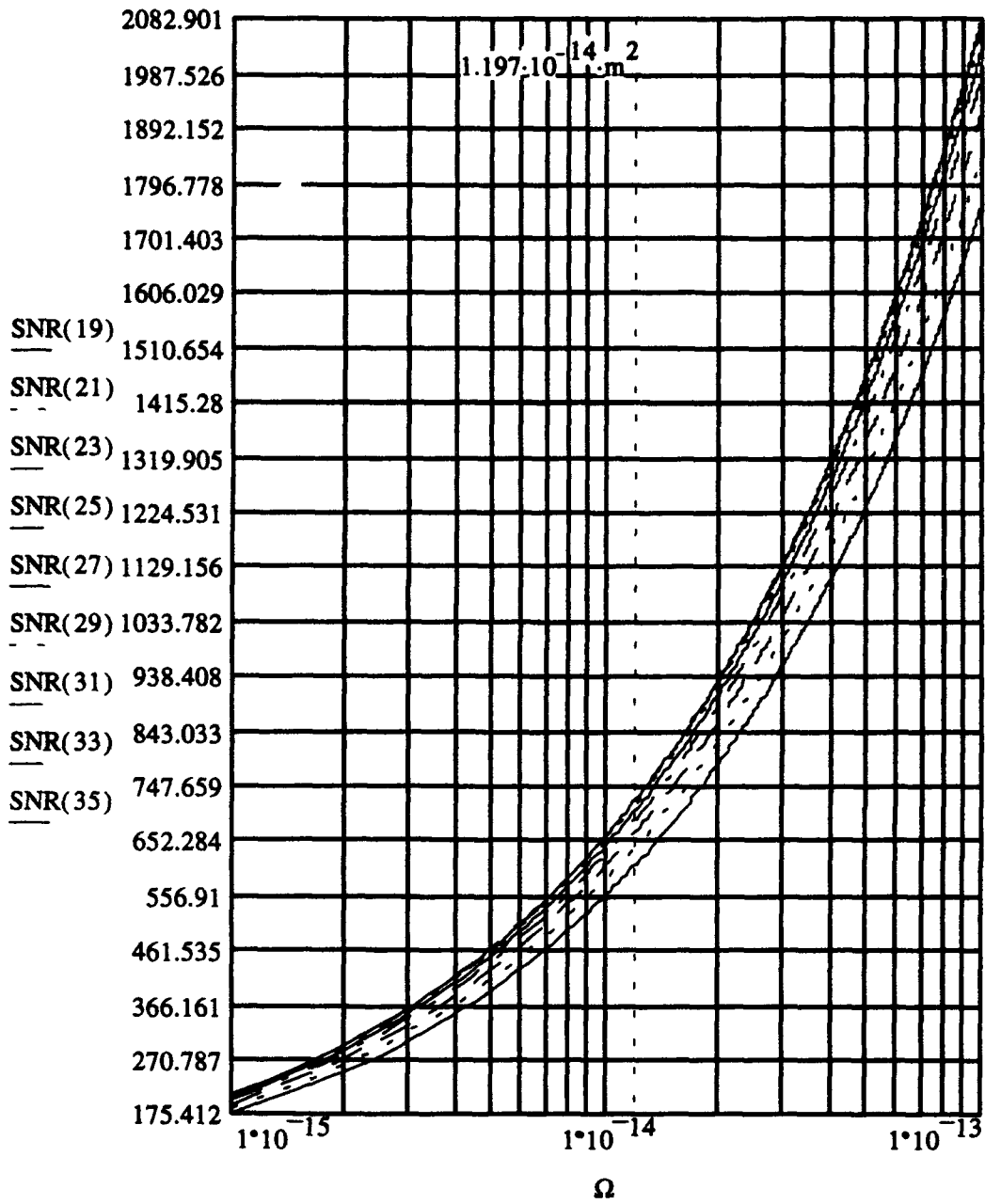


Figure E.12 Case (4), SNR vs  $\Omega$  ( $rad m^2$ ) (V), 10 nm

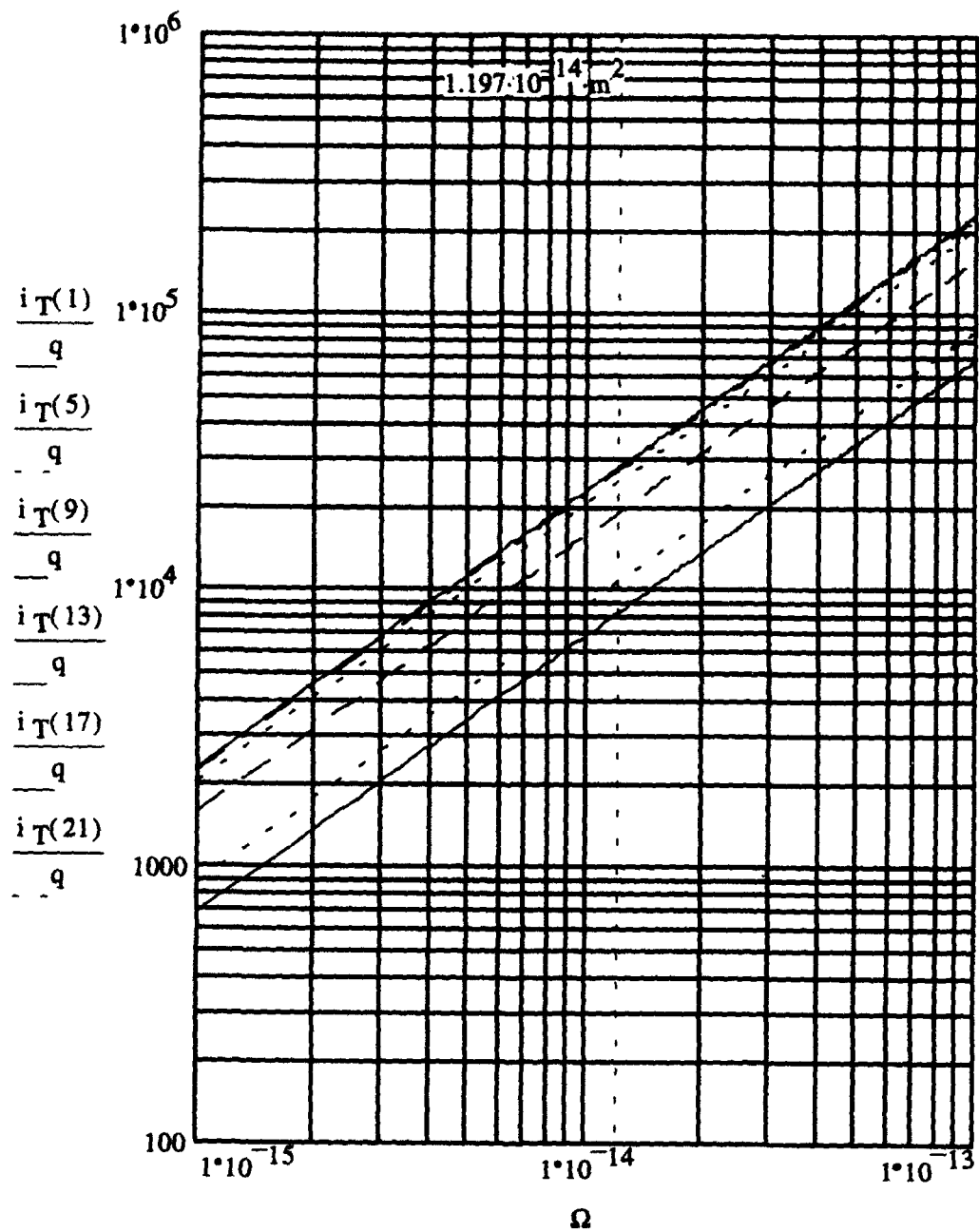


Figure E.13 Case (4), Count Rate  $\frac{i_T}{q}$  (1/s) vs  $\Omega$  ( $\text{rad m}^2$ ) (UV), 5 nm

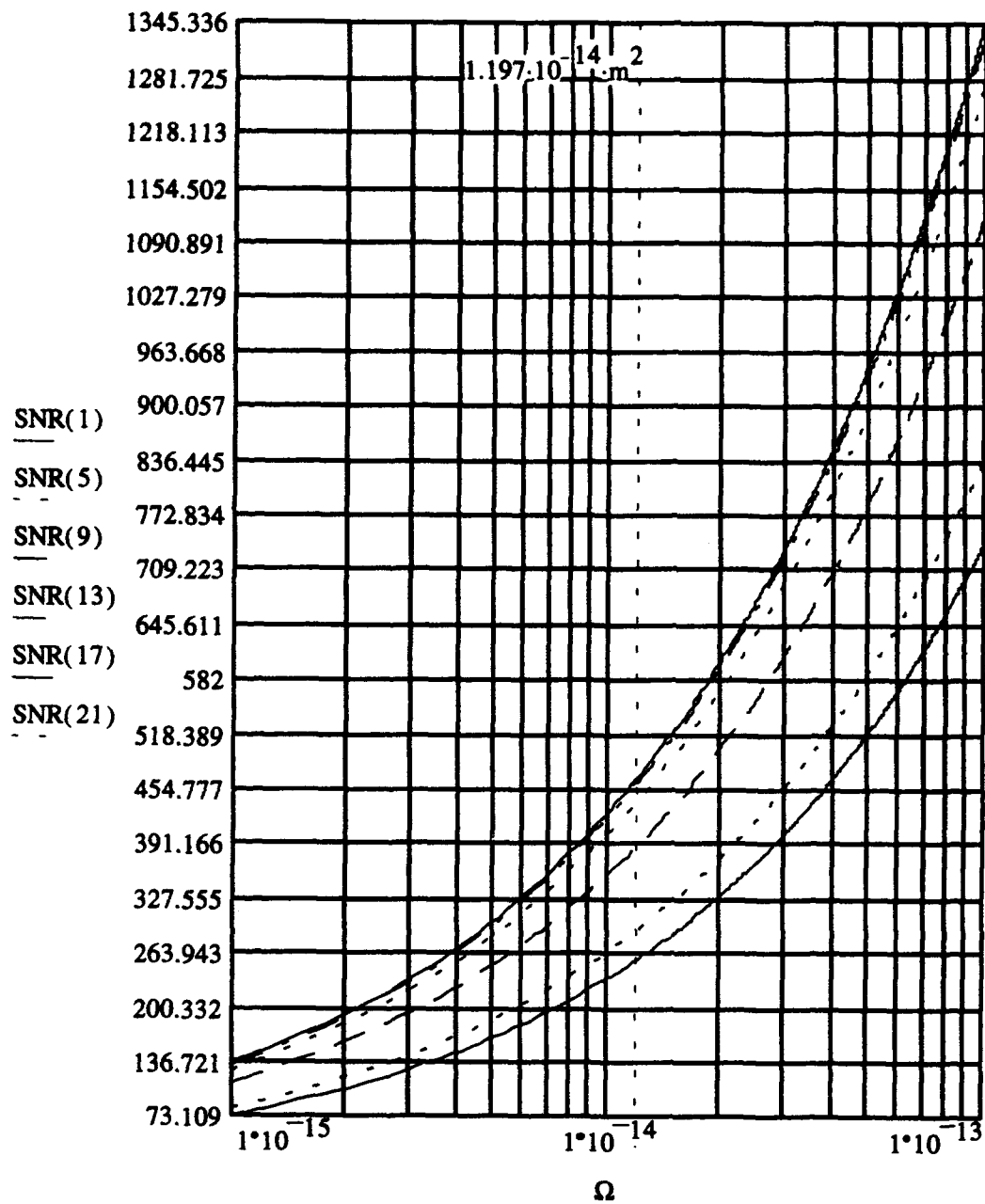


Figure E.14 Case (4), SNR vs  $\Omega$  ( $rad m^2$ ) (UV), 5 nm

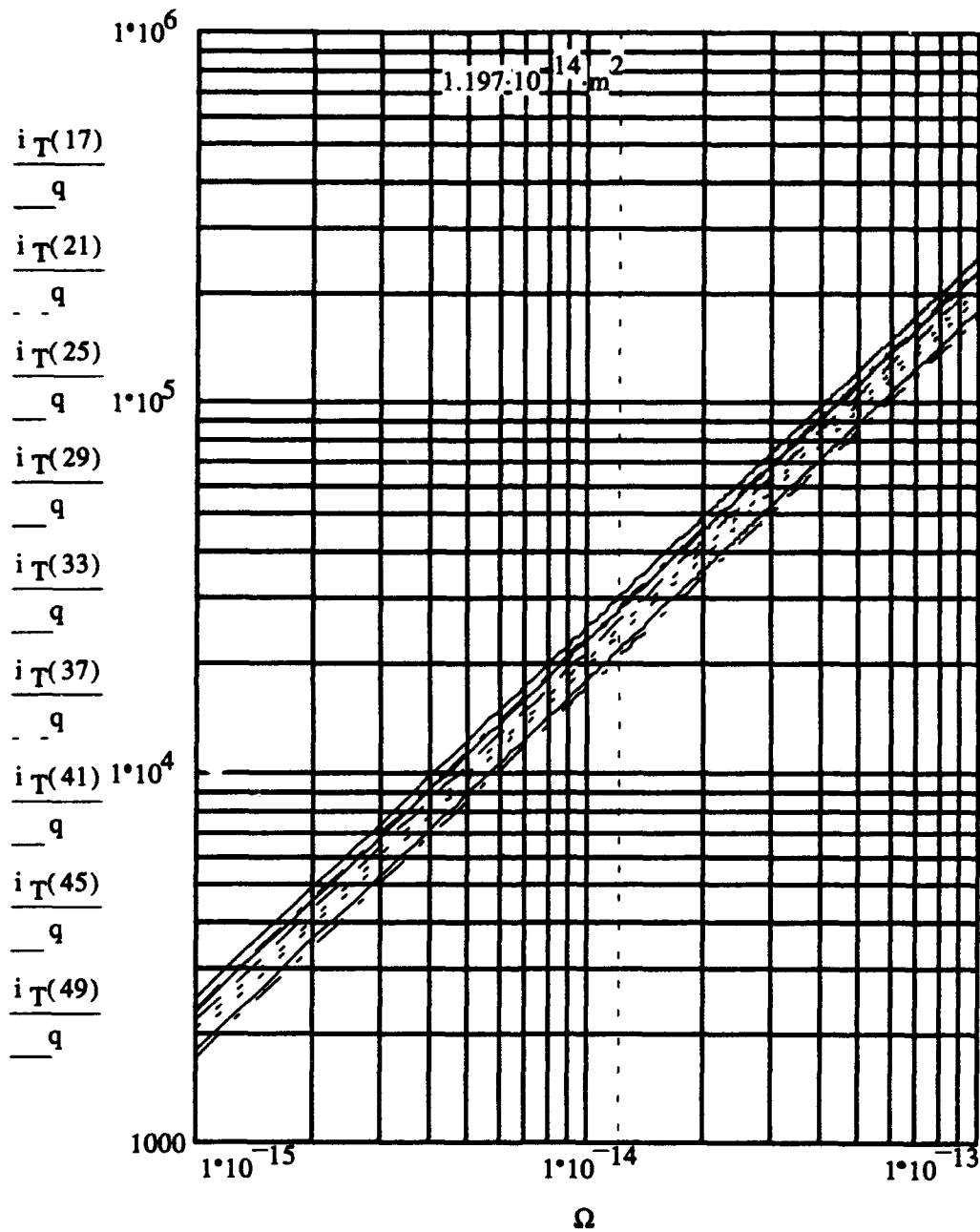


Figure E.15 Case (4), Count Rate  $\frac{i_T}{q}$  (1/s) vs  $\Omega$  (rad m<sup>2</sup>) (B), 5 nm



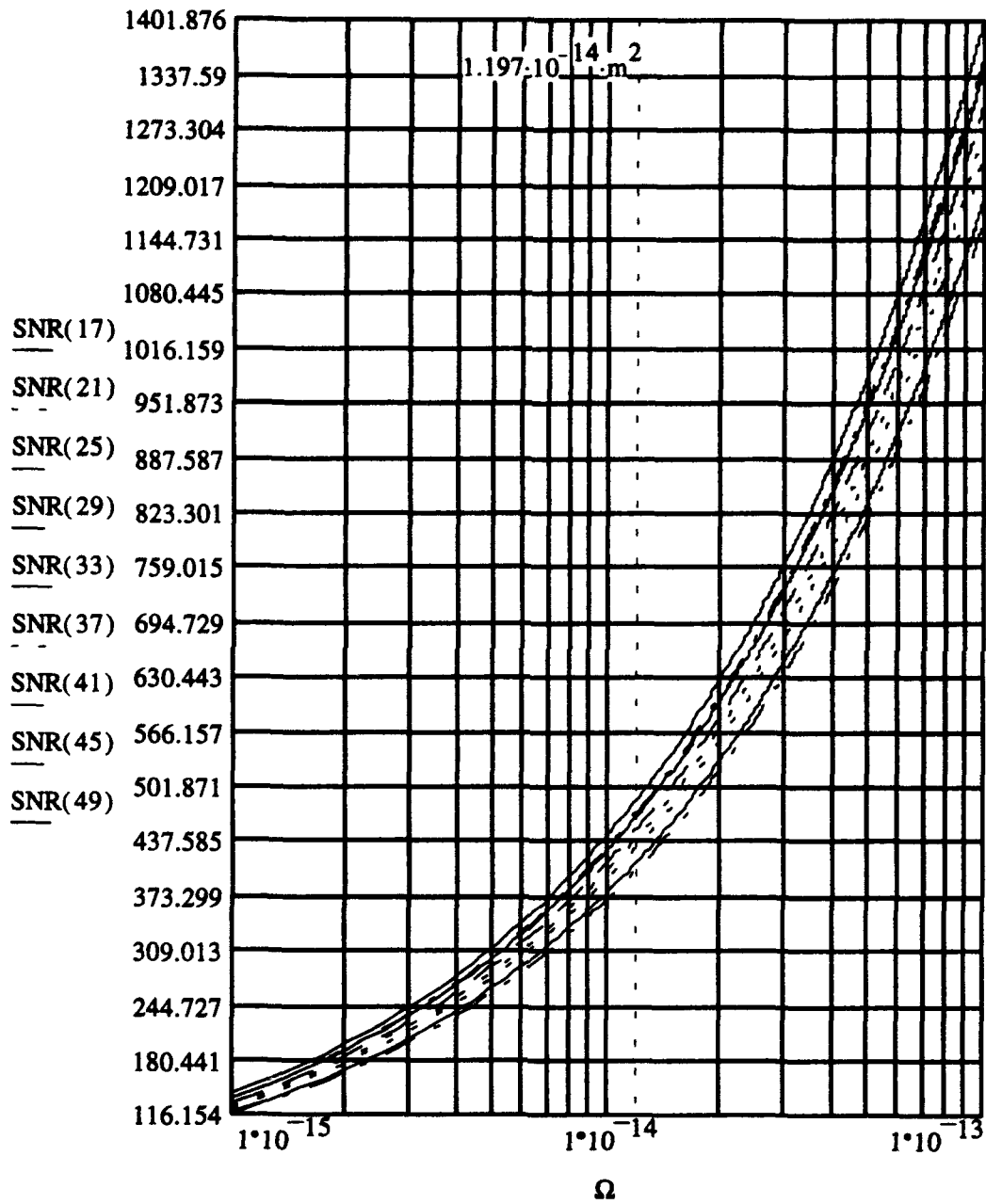


Figure E.16 Case (4), SNR vs  $\Omega$  ( $\text{rad m}^2$ ) (B), 5 nm

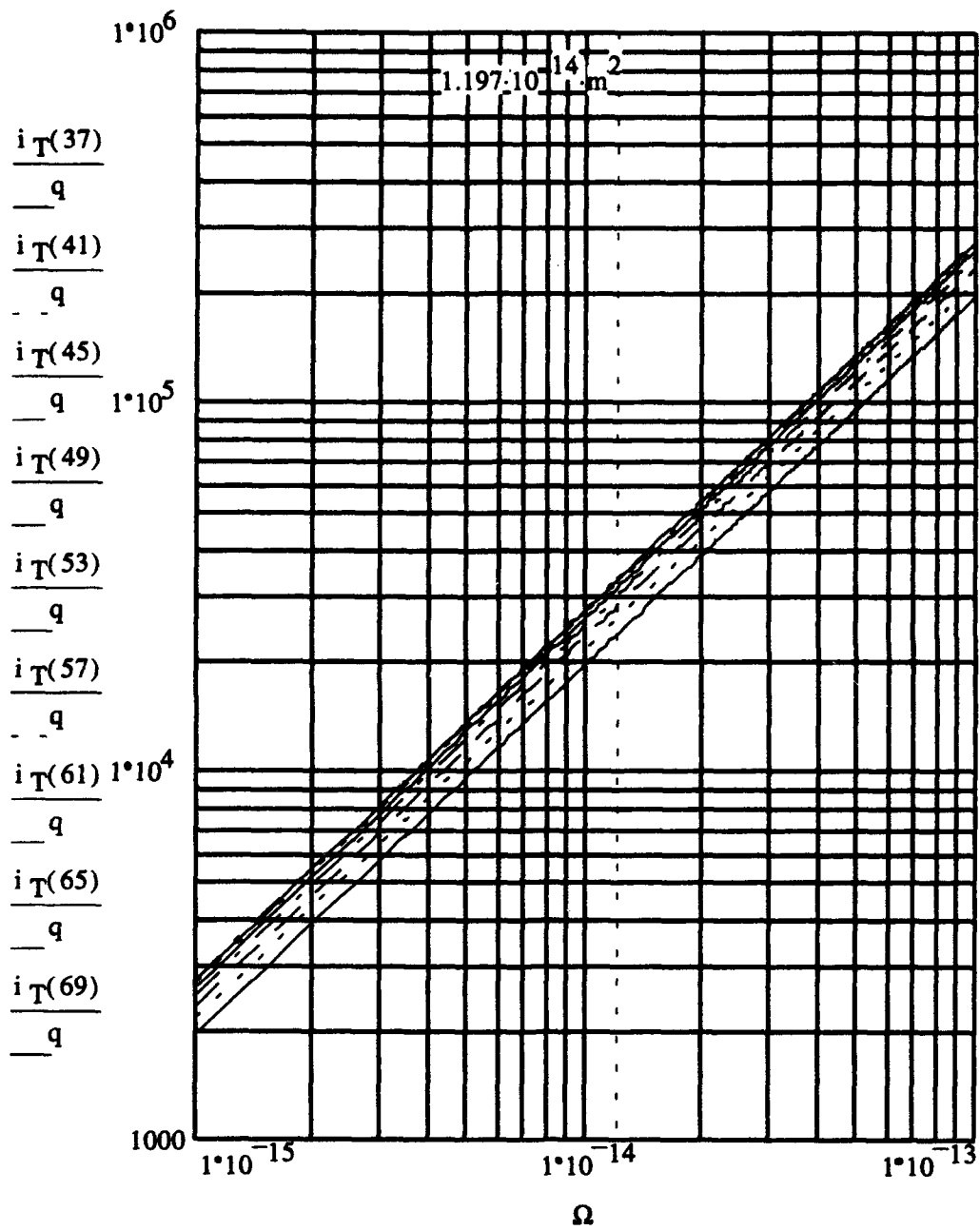


Figure E.17 Case (4), Count Rate  $\frac{i_T}{q}$  (1/s) vs  $\Omega$  ( $\text{rad m}^2$ ) (V), 5 nm

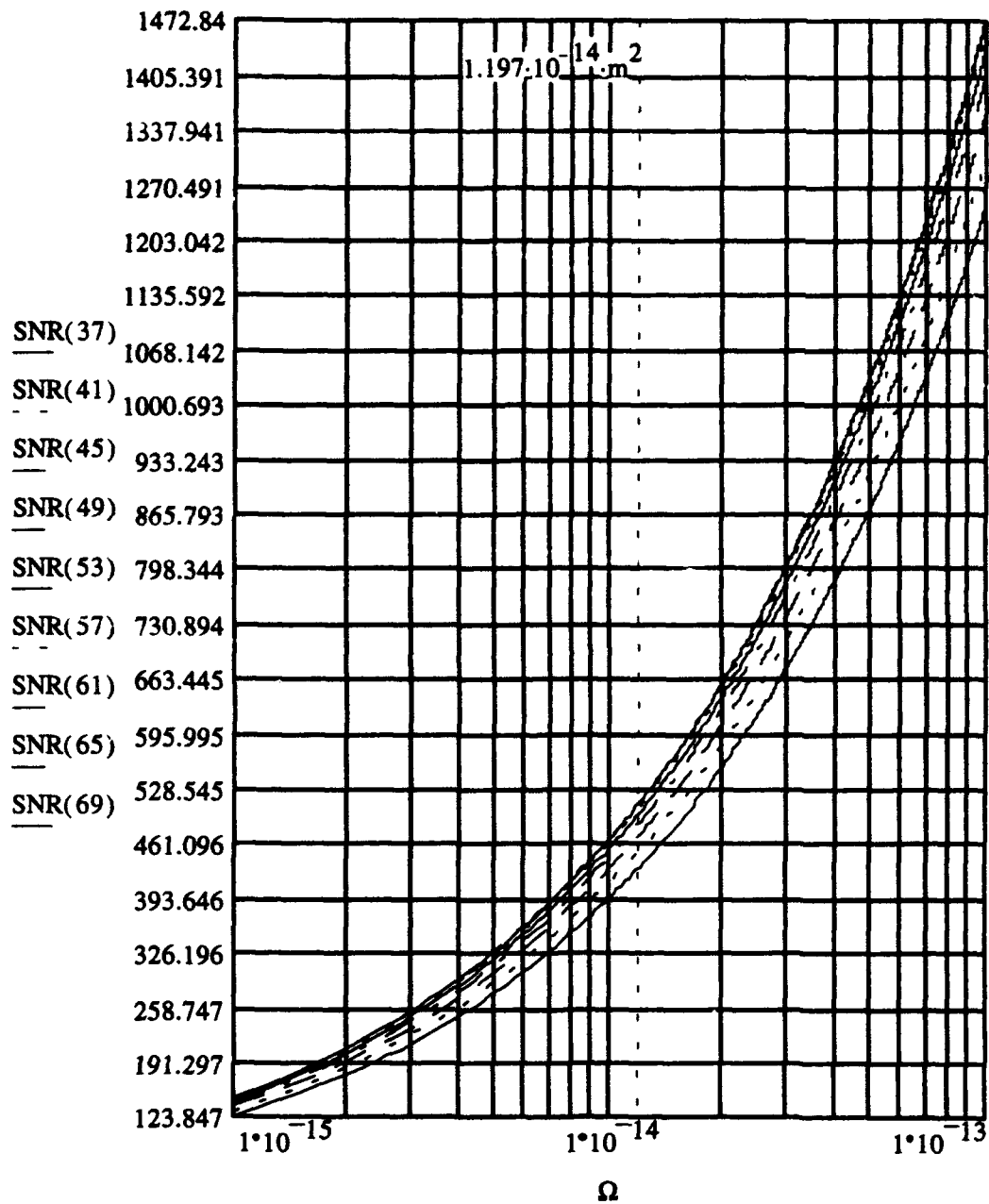


Figure E.18 Case (4), SNR vs  $\Omega$  ( $\text{rad m}^2$ ) (V), 5 nm

### *Appendix F. Spectral Reflectance of Various Materials*

Figure F.1 shows the spectral reflectance versus wavelength for SMC-02, Aluminum Alloy Type 2024-T3 (Mill Finish).

Figure F.2 shows the spectral reflectance versus wavelength for SMC-18, Silver.

Figure F.3 shows the spectral reflectance versus wavelength for SMC-20, Paint, Chemglaze A276 (White).

Figure F.4 shows the spectral reflectance versus wavelength for SMC-23, Solar Cell, Silicon.

Figure F.5 shows the spectral reflectance versus wavelength for SMC-30, Mylar, Aluminized (Aluminum Side Out).

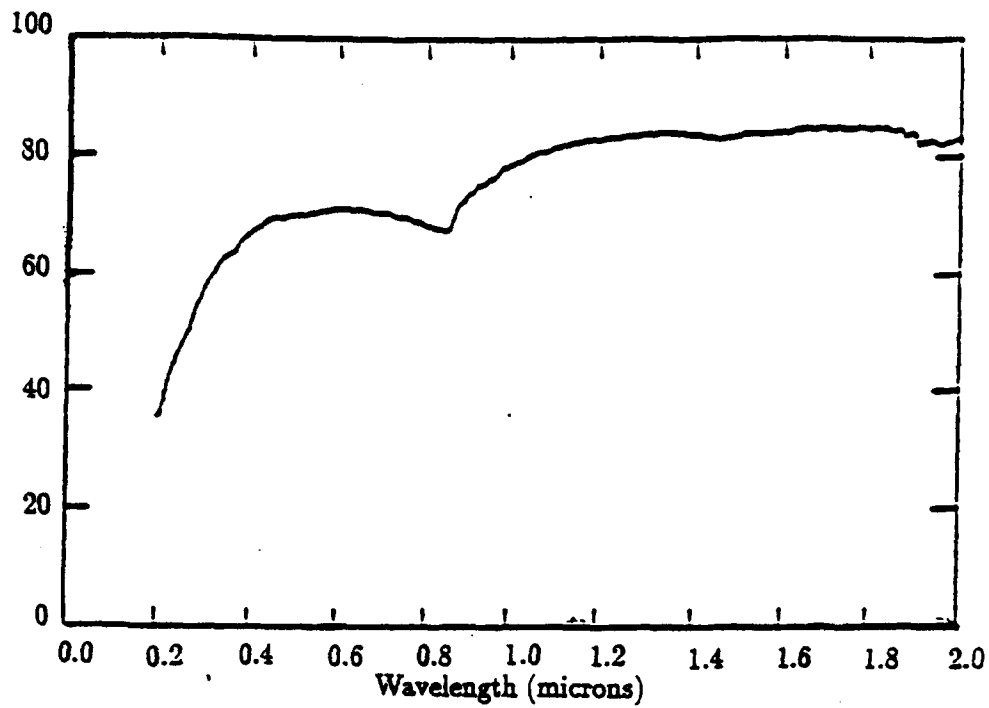


Figure F.1 Spectral Reflectance (%), SMC-02: Aluminum Alloy Type 2024-T3 (Mill Finish)

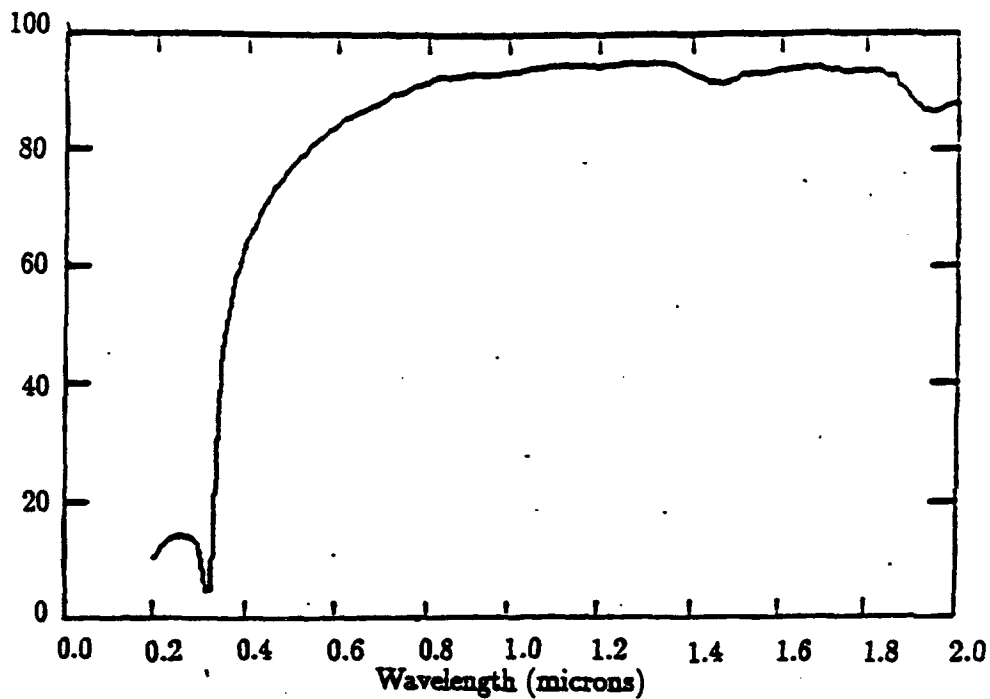


Figure F.2 Spectral Reflectance (%), SMC-18: Silver

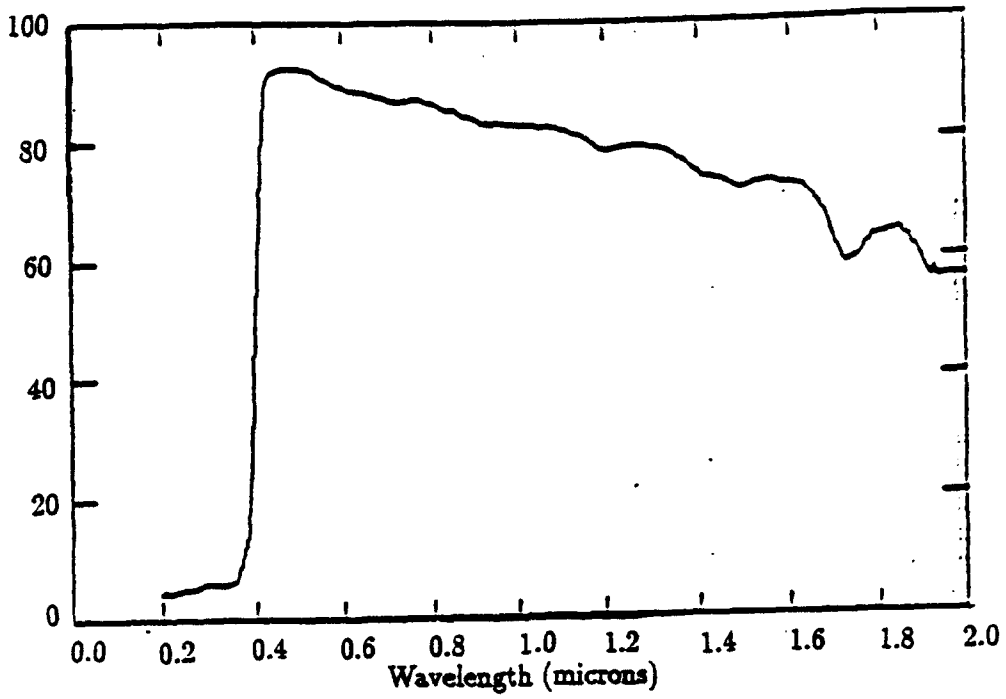


Figure F.3 Spectral Reflectance (%), SMC-20: Paint, Chemglaze A276 (White)

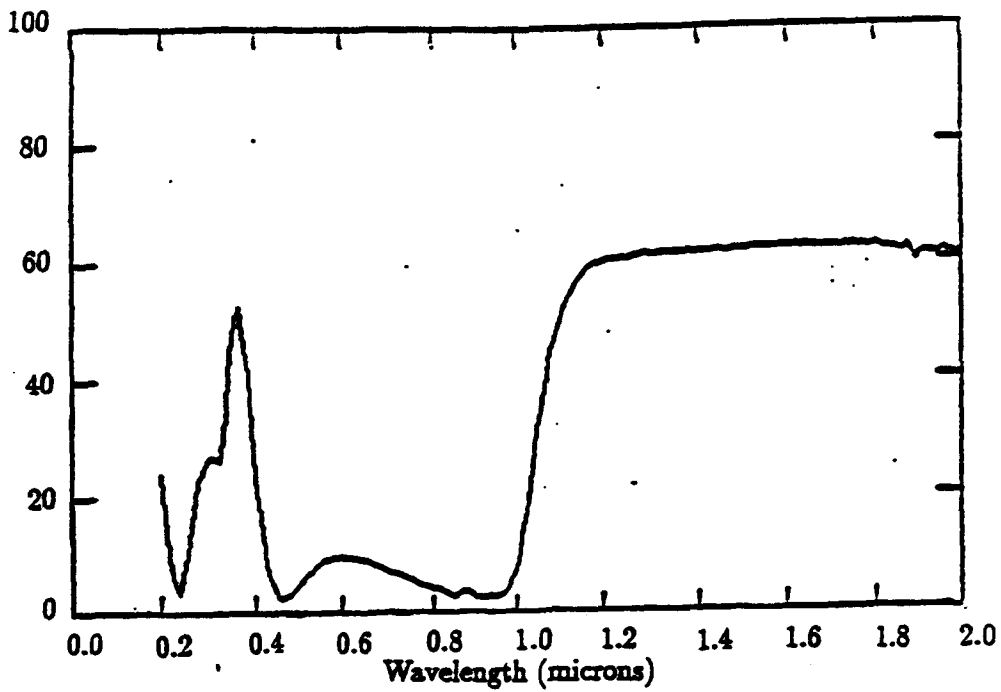


Figure F.4 Spectral Reflectance (%), SMC-23: Solar Cell, Silicon

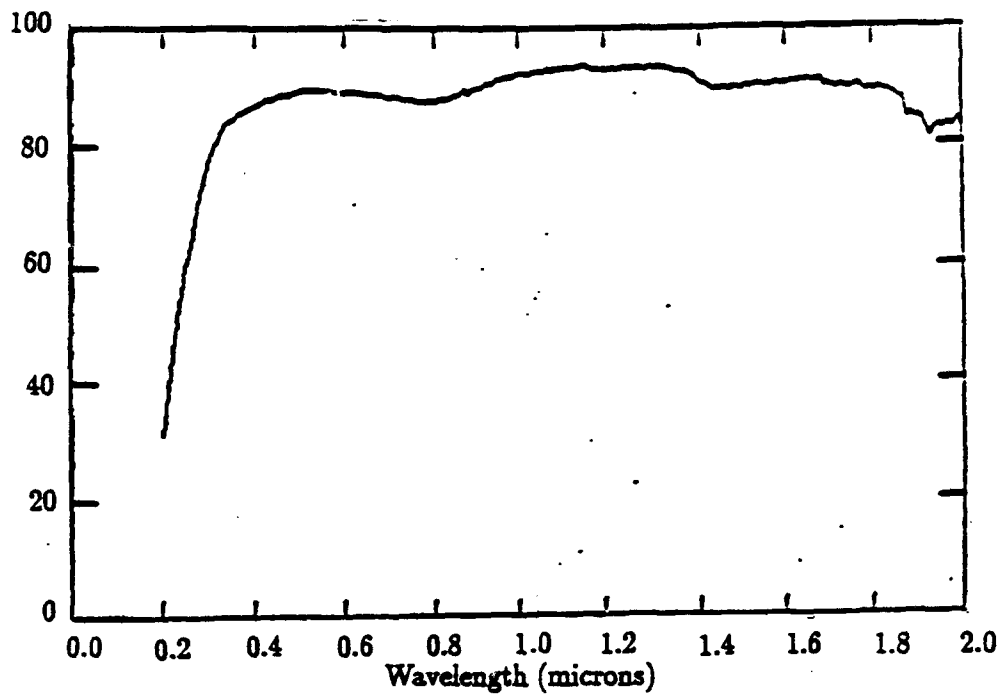


Figure F.5 Spectral Reflectance (%), SMC-30: Mylar, Aluminized (Aluminum Side Out)

## Bibliography

1. Beavers, W.I., et al. "Cylindrical Satellite Specular Season Photometry". Proceedings of the 1993 Space Surveillance Workshop, Vol II. MIT Lincoln Labs MA 1993.
2. Boyd, Robert W.. *Radiometry and the Detection of Optical Radiation* John Wiley and Sons, New York NY, 1983.
3. Dyjak, C.P. and Harrison, D.C. "Space-Based Visible Surveillance Experiment," *SPIE* Vol 1479 Surveillance Technologies, 1991.
4. Elachi, Charles. *Introduction to the Physics and Techniques of Remote Sensing* John Wiley and Sons, New York NY, 1987.
5. Lillesand, Thomas M. and Kiefer, Ralph W. *Remote Sensing and Image Interpretation, Second Edition* John Wiley and Sons, New York NY, 1987.
6. Mathcad. Version 3.1. Computer software. Mathsoft, Inc. Cambridge MA, 1992.
7. Photometrics, Ltd. *Charge-Coupled Devices for Quantitative Electronic Imaging*. Tucson AZ, 1992.
8. Photometrics, Ltd. *CCD Selection Chart*. Tucson AZ, 1992.
9. Prochko, Amy. Technical Staff, W.J. Schafer and Associates, Incorporated. Albuquerque, NM. Telephone interview. 11 Oct 93.
10. Roggemann, Michael C. Class notes, PHY 621, Electro-optical Space Systems Technology. School of Engineering, Air Force Institute of Technology, Wright Patterson AFB OH. Winter Quarter, 1992.
11. Roverse, Mark. Space Experiments Branch, Phillips Lab, Kirtland AFB, NM. Briefing slides. April 93.
12. Tarr, G. Imaging Technology Branch, Phillips Lab, Kirtland AFB, NM. Telephone interview. 17 May 93.
13. Tarr, G. Imaging Technology Branch, Phillips Lab, Kirtland AFB, NM. AFIT/Phillips Lab Technical Interchange Meeting, 22 Jul 92.
14. TRACOR GIE. *Matter.dat Surface Properties Data Compilation* Technical note, GIE-TN-92-013, 1992.
15. Wolfe, William L. and Zissis, George J. *The Infrared Handbook*. Office of Naval Research, Department of the Navy, Washington DC, 1978.



## *Vita*

Captain Daniel Hrovat was born on 4 July, 1963 in Garfield Heights, OH. He graduated from Independence High School, Independence, OH, in 1981. From high school, he entered the U.S. Air Force Academy, and graduated in 1985 with a Bachelor of Science in Physics. He received a regular commission in the USAF, and was assigned to Onizuka AFB, CA, where he worked budget and staff issues for the Satellite Control Network Activation Directorate. In 1987, he was assigned to Peterson AFB, CO, and joined the initial group of Air Force officers training to operate Department of Defense communications satellites. Following training, he was certified as a Defense Satellite Communications System, Phase III crew commander. From 1988-1989, he served on a satellite operations crew at Falcon AFB, CO, and was one of 151 officers who activated the 3rd Satellite Control Squadron (now the 3rd Space Operations Squadron). In 1990, he served in the squadron's Standardization and Evaluation section. In 1991, he was assigned to Clear AFS, AK, where he served as a missile warning crew commander and Chief, Standardization and Evaluation. He entered the Graduate School of Engineering, Air Force Institute of Technology, in May 1992. His follow on assignment is to Headquarters, Air Force Space Command/DRFT, Peterson AFB, CO

Permanent address: 6732 Brecksville Road  
Independence, Ohio 44131

# REPORT DOCUMENTATION PAGE

Form Approved  
OMB No. 0704-0188

Public reporting burden for this collection of information is estimated to average 1 hour per response, including the time for reviewing instructions, searching existing data sources, gathering and maintaining the data needed, and completing and reviewing the collection of information. Send comments regarding this burden estimate or any other aspect of this collection of information, including suggestions for reducing this burden, to Washington Headquarters Services, Directorate for Information Operations and Reports, 215 Jefferson Davis Highway, Suite 1204, Arlington, VA 22202-4302, and to the Office of Management and Budget, Paperwork Reduction Project (0704-0188), Washington, DC 20503.

1. AGENCY USE ONLY (Leave blank)	2. REPORT DATE <b>December 1993</b>	3. REPORT TYPE AND DATES COVERED <b>Master's Thesis</b>	
4. TITLE AND SUBTITLE <b>HYPERSPECTRAL ANALYSIS OF SPACE OBJECTS: SIGNAL TO NOISE EVALUATION</b>		5. FUNDING NUMBERS	
6. AUTHOR(S) <b>Daniel Hrovat, Captain, USAF</b>		8. PERFORMING ORGANIZATION REPORT NUMBER <b>AFIT/GSO/ENP/93D-02</b>	
7. PERFORMING ORGANIZATION NAME(S) AND ADDRESS(ES) <b>Air Force Institute of Technology, WPAFB OH 45433-6583</b>		10. SPONSORING / MONITORING AGENCY REPORT NUMBER	
9. SPONSORING / MONITORING AGENCY NAME(S) AND ADDRESS(ES) <b>Phillips Lab/LIMI Kirtland AFB, NM 87117</b>		10. SPONSORING / MONITORING AGENCY REPORT NUMBER	
11. SUPPLEMENTARY NOTES			
12a. DISTRIBUTION / AVAILABILITY STATEMENT <b>Approved for public release; distribution unlimited</b>		12b. DISTRIBUTION CODE	
13. ABSTRACT (Maximum 200 words) <b>Hyperspectral analysis of space objects is being considered as a means of enhancing Space Object Identification (SOI) capabilities. This study develops a mathematical simulation based on fundamental radiometry principles to evaluate the feasibility of hyperspectral analysis of space objects. The study uses Signal to Noise Ratio (SNR) as the basis for the feasibility evaluation, and addresses the question: Is there enough target signal in narrow wavelength bandwidths to conduct hyperspectral measurements of space objects? The analysis characterizes the target signal and noise sources using fundamental radiometry, and develops a flexible radiometry model which calculates the target signal count rate, and SNR for a specified target-sensor configuration. The model was applied to four case studies, and revealed: 1) Enough target signal is present in narrow wavelength bandwidths for hyperspectral measurements; 2) Differences exist in signal strength as a function of wavelength and bandwidth which may serve as a basis for Space Object Identification applications. Hyperspectral analysis of space objects warrants further investigation.</b>			
14. SUBJECT TERMS <b>Hyperspectral analysis, Space Object Identification (SOI), Space Surveillance</b>		15. NUMBER OF PAGES <b>152</b>	
17. SECURITY CLASSIFICATION OF REPORT <b>Unclassified</b>		16. PRICE CODE	
18. SECURITY CLASSIFICATION OF THIS PAGE <b>Unclassified</b>		20. LIMITATION OF ABSTRACT <b>UL</b>	
19. SECURITY CLASSIFICATION OF ABSTRACT <b>Unclassified</b>		20. LIMITATION OF ABSTRACT <b>UL</b>	